APR 12 1982

1051-A-11

Y3.N88:25/2283

NUREG/CR-2283
SAND81-1754
R7
Printed January 1982

COMPLETED
154

ORIGINAL

Direct Observation of Melt Behavior During High Temperature Melt/Concrete Interactions

Dana A. Powers, Frank E. Arellano

Prepared by
Sandia National Laboratories
Albuquerque, New Mexico 87185 and Livermore, California 94550
for the United States Department of Energy
under Contract DE-AC04-76DP00789

SF2

Prepared for
U. S. NUCLEAR REGULATORY COMMISSION I

NOTICE

This report was prepared as an account of work sponsored by an agency of the United States Government. Neither the United States Government nor any agency thereof, or any of their employees, makes any warranty, expressed or implied, or assumes any legal liability or responsibility for any third party's use, or the results of such use, of any information, apparatus product or process disclosed in this report, or represents that its use by such third party would not infringe privately owned rights.

Available from
GPO Sales Program
Division of Technical Information and Document Control
U.S. Nuclear Regulatory Commission
Washington, D.C. 20555

and

National Technical Information Service
Springfield, Virginia 22161

II

NUREG/CR-2283
SAND81-1754
R7

DIRECT OBSERVATION OF MELT BEHAVIOR DURING HIGH TEMPERATURE MELT/CONCRETE INTERACTIONS

D. A. Powers

F. E. Arellano

Date Published: January, 1982

Reactor Containment Safety Studies Division
Sandia National Laboratories
Albuquerque, New Mexico 87185
Operated by
Sandia Corporation
for the
U. S. Department of Energy

Prepared for
Division of Accident Evaluation
Office of Nuclear Regulatory Research
U. S. Nuclear Regulatory Commission

Under Memorandum of Understanding DOE 40-550-75
NRC FIN No A 1218

ABSTRACT

The feasibility of using a pulsed x-ray source and an x-ray image intensification system to provide continuous, real time data on high temperature melt behavior during interaction with concrete is demonstrated. A test of the system using a 1972g metallothermically generated melt interacting with limestone/common sand concrete is described. Analysis of the recorded x-ray image of the melt is used to determine the mode of melt contact with concrete, the time dependence of pool swelling due to entrained gas, and the nature of gas injection into the melt. Localized gas injection is found. Swelling of the pool increases with superficial gas velocity to an asymptotic limit. Results are shown to be consistant with the gas film model of melt-to-concrete heat transfer. The image data are used to assist interpretation of diagnostic data -- gas generation rate, gas composition and concrete temperatures -- gathered in the test.

TABLE OF CONTENTS

I. Description of the Experiments 2

II. Performance of the Image Intensification System 21

III. Test Results 22

IV. Quantitative Data 46

  A. Gas Composition 46

  B. Gas Generation Rates 53

  C. Temperature Data 61

V. Summary 69

VI. References 71

Appendix A: Temperatures in Thermitic Melts 73

Appendix B: Viscosity of Mixtures 79

Appendix C: Photographs of the Melt Image 83

TABLES

Number		Page
I	Simulant Experiments and Analytic Models That Have Been Used for Understanding Melt/Concrete Interactions	3-5
II	Chemical Composition of the Limestone/ Common Sand Concrete Used in Test BURN 1	19
III	Events of Test BURN 1	24
IV	Average Time Melt Was in Contact with Concrete at Nine Locations on the Cavity Surface During Test BURN 1	27
V	Compositions of Gas Samples Drawn During Test BURN 1	47
VI	Oxygen/Nitrogen Ratios in the Gas Samples	49
VII	Estimated Quench Temperatures and Gas Compositions	52
A-I	Phase Changes in Thermite Reaction Products	74
B-I	Comparison of Calculated and Observed Viscosities of Air	81

ILLUSTRATIONS

Number		Page
1	Schematic Diagram of the Crucible and Instrumentation Tower Used in Test Burn 1	6
2	Schematic Diagram of the Baffle Section of the Instrumentation Tower and the Arrangement for Sealing the Tower to the Concrete	8
3	Photograph of the Assembled Crucible, Baffle Section, and "T" Section Used in Test BURN 1 (SAND Photo C78-6444)	10
4	Typical Output from the Line Pressure Transducer During a Gas Sampling Event	11
5	Calibration Curve for the Laminar Flow Element Mounted on the Sidearm of the Instrumentation Tower Used in Test BURN 1	13
6	Comparision of Calibration Data Taken Before and After Test BURN 1	14
7	Photograph of the X-ray Source, Image Intensifier and the Instrumentation Tower as Used in Test BURN 1 (SAND Photo C78-6445)	16
8	Differential Thermogram of Metal Phase Formed by the Metallothermic Reaction in Test BURN 1	17
9	Differential Thermogram of the Limestone/ Common Sand Concrete Used in Test BURN 1	20
10	Locations Monitored to Determine the Fraction of Time Melt Spent in Contact with the Concrete	26
11	Percent of Time the Melt Was in Contact with Concrete at Location P1	28
12	Percent of Time the Melt Was in Contact with Concrete at Location P2	29
13	Percent of Time the Melt Was in Contact with Concrete at Location P3	30

ILLUSTRATIONS (Continued)

Number Page

14 Percent of Time the Melt Was in Contact with Concrete at Location P4 31

15 Percent of Time the Melt Was in Contact with Concrete at Location P5 32

16 Percent of Time the Melt Was in Contact with Concrete at Location P6 33

17 Percent of Time the Melt Was in Contact with Concrete at Location P7 34

18 Percent of Time the Melt Was in Contact with Concrete at Location P8 35

19 Percent of Time the Melt Was in Contact with Concrete at Location P9 36

20 Top Surface of the Solidified Metal Pool (SAND Photo C78-9402) 39

21 Bottom Surface of the Solidified Metal Pool (SAND Photo C78-9403) 40

22 Photograph of a Cross-Section of the Metal Slug Showing the Positions of Hardness Determinations 42

23 Time Dependence of Maximum Pool Depth in Test BURN 1. Pool Depth is in Units of Fraction of the Expected Quiescent Pool Depth 44

24 Time Dependence of the Mean Pool Depth in Test BURN 1. Pool Depth is in Units of Fraction of the Expected Quiescent Pool Depth 45

25 Comparison of Observed CO/CO_2 Ratios to Those Predicted for Two Iron Oxidation Reactions 54

26 Gas Flow Rate in Test BURN 1 56

ILLUSTRATIONS (Continued)

Number		Page
27	Gas Flow Rate in the first 30 Seconds of Test BURN 1	57
28	Cumulative Gas Production During Test BURN 1	58
29	Cumulative Production of H_2, CO, and CO_2 During Test BURN 1	59
30	Maximum Pool Depth as a Function of Superficial Gas Velocity (STP). Pool Depth is in Units of Fraction of the Expected Quiescent Pool Depth	62
31	Mean Pool Depth as a Function of Superficial Gas Velocity (STP). Pool Depth is in Units of Fraction of the Expected Quiescent Pool Depth	63
32	Temperature Data from Thermocouple TC5 Below the Bottom of the Crucible Cavity	64
33	Temperature Data from Thermocouple TC5 for the First 500s of Test BURN 1	65
34	Temperature Data from Thermocouple TC4 on the External Wall of the Crucible	66
35	Temperature Data from Thermocouple TC4 for the First 500s of Test BURN 1	67
A-1	Maximum Temperature of A Thermitic Melt	76

The attack of molten core materials on concrete is a critical aspect of a severe nuclear reactor accident involving fuel melting (1). The behavior of the melt, especially at the interface with concrete, must be known if quantitative descriptions of the interaction with concrete are to be developed. Heat transfer from melt to concrete, passage through the melt of gases liberated from the concrete, formation of solidified crusts over the melt, and swelling of the melt by entrained gases are a few of the topics of reactor safety analysis that could be addressed if melt behavior were better known.

Typical experimental investigations of interactions between melt and concrete can yield data on melt behavior only by inference. Direct observation of even the top surfaces of the melts during these tests is difficult because of the high temperatures and the emissions of dense aerosol (2).

Simulant experiments and detailed analytic models have been used to obtain both qualitative and quantitative information concerning the melt-to-concrete heat transfer, in particular. Some of these simulant experiments and models are summarized in Table 1. The model of heat transfer that has received the most attention is the "gas film" model. This model has been derived by independent researchers in two countries (see Table 1) and shows some indications of providing an adequate description of very high temperature melt/concrete interactions. Recently, an alternate description of the heat transfer process, the "slag film" model, has shown potential for predicting melt/concrete interactions. The "stagnation flow" model has not received the attention devoted to the two film models.

The melt/concrete system has been particularly difficult to simulate. Objections to the qualitative significance of the simulant experiments can be raised. The location and the rate of gas generation are frequent points of objection. Data on the real system are needed to properly design simulant experiments to obtain quantitative correlations of melt behavior.

In this report, the feasibility of using x-ray image intensification to monitor high temperature melt behavior continuously during interaction with concrete is demonstrated. This technique provides qualitative melt behavior information. It also allows precise determination of freezing of the melt and could be used to accurately monitor concrete erosion. The technique does not displace simulant experimentation as a basis for development of quantitative correlations concerning the attack of high temperature fluids on decomposing solids. It should, however, yield data that will aid in selection of simulants more representative of concrete and molten core materials.

I. Description of the Experiment

The test of the feasibility of x-ray image intensification was designated test BURN 1. The test consisted of igniting a melt-producing metallothermic reaction within a concrete crucible. The melt behavior was observed by image intensification of an x-ray beam directed through the concrete crucible.

The crucible and the instrumentation tower used in the test are schematically depicted in Figure 1. The crucible was made of limestone/common sand concrete. An 8.9-cm-diameter, 14.9-cm-deep cavity was cut, using water lubricant, in a 15.2-cm-diameter, 30.5-cm-long compression-testing cylinder. The cylinder had aged 1.4 years prior to the cutting of the crucible cavity.

Two 1-mm-diameter, stainless steel sheathed, type K thermocouples were placed in the concrete. One thermocouple (TC4) was wound around the crucible in a horizontal groove about 2.5 cm above the original bottom of the crucible cavity. The thermocouple was held in place by two layers of 0.2-cm-thick asbestos paper. The thermocouple was about 2.8 cm from the original crucible cavity wall.

The second thermocouple (TC5) was located 7.7 cm deep along a crucible-block diameter about 3.2 cm below the original cavity bottom. The thermocouple was held in a 0.6-cm-diameter hole with Saureisen #63 castable ceramic.

The thermocouple outputs were recorded at 3 sec/cm on Soltec model VP6232S strip chart recorders.

TABLE I Simulant Experiments and Analytic Models That Have Been Used for Understanding Melt/Concrete Interactions

REFERENCE	DESCRIPTION
D. W. Larson & D. O. Lee, Simulant experiments with Fluid-Mechanic/Thermal Interactions of Molten Material and a Decomposing Solid SAND76-0240, Sandia Laboratories, Albuquerque, NM - Dec. 1976	plastic and low melting metals; interfacial temperature condition derived.
H. Alsmeyer and M. Reimann, "On the Heat and Mass Transport Processes on a Horizontal Melting or Decomposing Layer Under a Molten Pool" presentation at the Winter Meeting ASME, Atlanta, GA - Nov. 27 - Dec. 2, 1972	The gas film model for heat transport is derived.
V. K. Dhir, J. N. Castle, and I. Catton, "Role of Taylor Instability on Sublimation of a Horizontal Slug of Dry Ice" J. Heat Transfer, 411-418 (1977)	Simulant experiments with water and dry ice and frozen xylene/dry ice and water; the gas film model that differs from that by Alsmeyer and Reiman only by the value of a constant is derived.
F. G. Blottner, Hydrodynamics and Heat Transfer Characteristics of Liquid Pools with Bubble Agitation SAND 79-1132 Sandia National Laboratories, Albuquerque, NM, Nov. 1979 see also references therein for citations concerning heat transfer to a horizontal porous plate with gas injection	A critical review of various heat transfer models for melt/concrete interactions; suggests gas generation rates are too low for applicability of the gas film model; a slag film model is suggested.
J. F. Muir and A. S. Benjamin "Modelling of Molten Fuel/Concrete Interactions," Proc. of the ANS-ENS Topical Meeting on Thermal Reactor Safety (Knoxville, Tenn., April 6-9, 1980) CONF-800403/V-1 p 205	Derivation of the slag film model; the model accounts for experimental data as well as does the gas film model.

TABLE I (Cont'd)

REFERENCE	DESCRIPTION
A. S. Benjamin "Core-Concrete Pool Dynamics and Interfacial Heat Transfer," Proc. ANS/ASME/NRC Topical Meeting on Nucl. Reac. Thermohydraulics, Saratoga Springs, NY, October 5-8, 1980 NUREG/CP 0014 Vol 2, p. 1437.	Further development of the slag film model.
H. H. Reineke, L. Rinkleff and R. Schramm "Heat Transfer Between Molten Core Material and Concrete," Proc. of the Third Post-Accident Heat Removal Information Exchange (Argonne, Illinois, November 2-4, 1977) ANL 78-10 Argonne Nat'l Labs, Argonne, Ill.	Stagnation flow model developed.
I. K. Paik, D. K. Felde, S. I. Abdel-Khalik, "Simulation of Overlaying Steel Layers on the Growth of Molten Core Debris in Concrete," Transactions ANS 33, 529 (1979)	Simulation experiment with water and ammonium bicarbonate dispersed in carbowax 1540. The effect of gas generation on the relative growth of a pool in the horizontal and vertical directions is shown. Immiscible surface layer made of 1-haloheptanes.
I. K. Paik and S. I. Abdel-Khalik "Simulation Experiments on the Retention of Molten Core Debris Pools in Composite Sacrificial Beds," Transactions ANS 33, 530 (1979)	Similar to preceding citation except an immiscible surface layer was not included.
D. K. Felde, H. S. Kim and S. I. Abdel-Khalik, "Convective Heat Transfer Correlations for Molten-Core Debris Pools Growing in Concrete," Transactions ANS 33, 544 (1979)	The heat transfer correlations developed: (1) downward with solid upper boundary: $(Nu)(W/L) = 204 (ReFr)^{0.05}$

TABLE I (Cont'd)

REFERENCE	DESCRIPTION
	(2) downward with free upper boundary: $Nu(W/L) = 231\ (ReFr)^{0.04}$ (3) sideward: $Nu(W/L) = 194\ (ReFr)^{0.043}$ (4) upward with solid upper boundary: $Nu(W/L) = 565\ (ReFr)^{0.048}$
I. K. Pail and S. I. Abdel-Khalik Retention of Molten Core Debris Pools in Composite Sacrificial Beds, COO-4261-10 University of Wisconsin, Madison, Wisconsin (no date given)	Ammonium bicarbonate dispersed in carbowax 1500 and 1000 is used to simulate composite beds of concrete.
D. K. Felde, Z. Musicki, and S. I. Abdel-Khalik, "Growth of Volumetrically Heated Pools in Miscible Gas-Releasing Solid Beds," European Applied Research, 1 (6) 1567-1576 (1979)	
D. K. Felde, H. S. Kim, and S. I. Abdel-Khalik, "Convective Heat Transfer Correlations for Molten Core Debris Pools Growing in Concrete," Nucl. Eng. Design, 58 65-74 (1980)	Heat transfer at a porous plate with gas injection; porous plates both at bottom and on sidewalls. Superficial gas velocities 0-.4 cm/s.
R. Farhadieh, unpublished results see also: R. Farhadieh, M. Epstein, and J. D. Bingle, "Downward Penetration of a Hot Liquid Pool into an Underlying Meltable Solid," Trans. ANS November 1980, in press	Simulation experiments with hydrochloric acid solution and sodium carbonate in polyethylene glycol 1500. Suggests a critical ratio between pool and bed densities yields maximum erosion. Very low superficial gas velocities.
R. Farhadieh and L. Baker, Jr. "Heat Transfer Phenomenology of a Hydrodynamically Unstable Melting System," J. Heat Transfer, 100 305 (1978)	

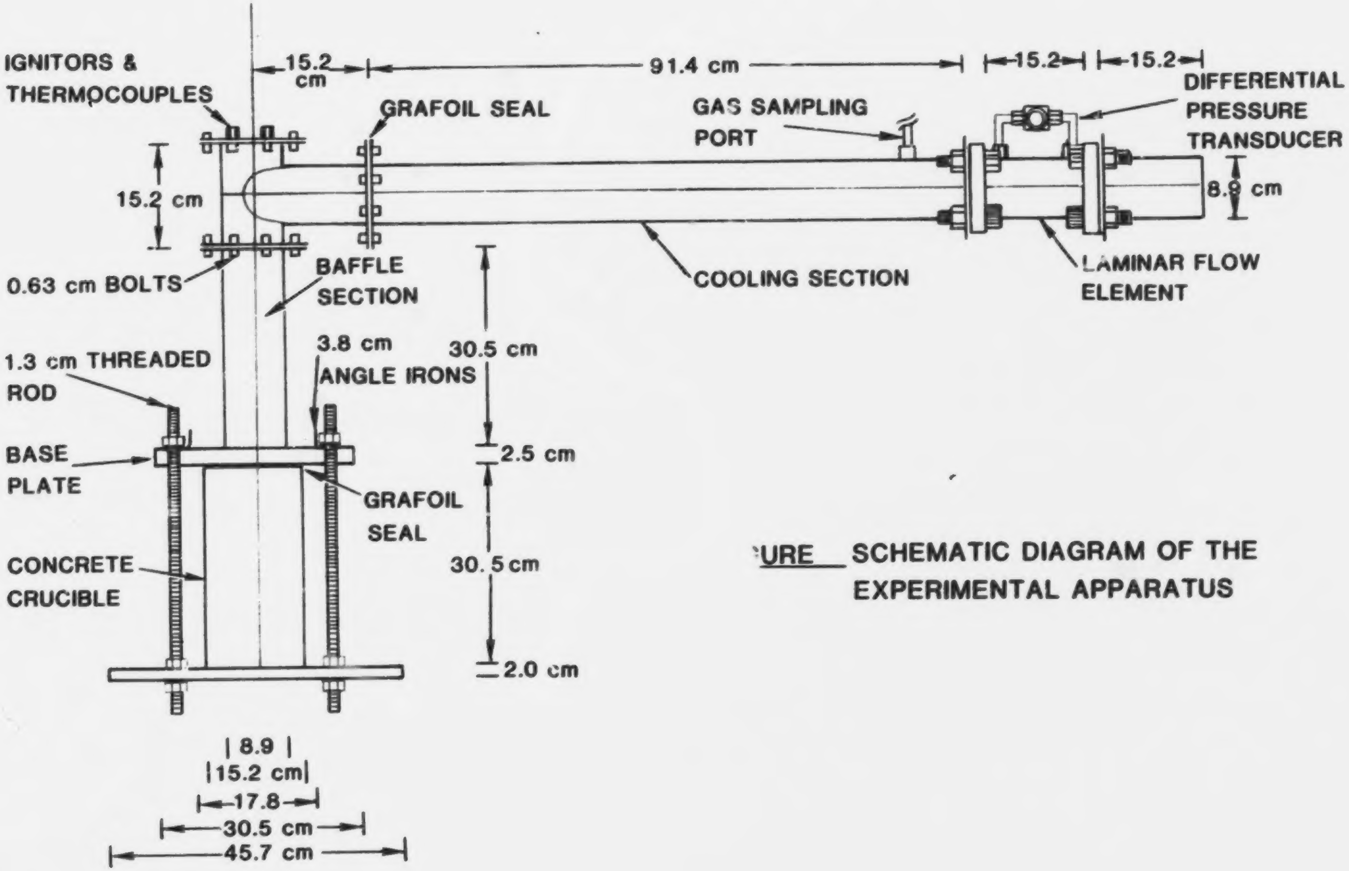
IGNITORS &
THERMOCOUPLES
15.2 cm
91.4 cm
15.2
15.2
DIFFERENTIAL PRESSURE TRANSDUCER
GRAFOIL SEAL
GAS SAMPLING PORT
15.2 cm
8.9 cm
0.63 cm BOLTS
BAFFLE SECTION
COOLING SECTION
LAMINAR FLOW ELEMENT
3.8 cm ANGLE IRONS
30.5 cm
1.3 cm THREADED ROD
BASE PLATE
2.5 cm
GRAFOIL SEAL
CONCRETE CRUCIBLE
30. 5 cm
2.0 cm
URE SCHEMATIC DIAGRAM OF THE EXPERIMENTAL APPARATUS
8.9
15.2 cm
17.8
30.5 cm
45.7 cm

Figure 1 Schematic Diagram of the Crucible and Instrumentation Tower Used in Test Burn 1

The crucible was capped with a steel instrumentation tower. The tower consisted of the following sections:

1) base plate
2) baffle chamber
3) cooling section
4) laminar flow element
5) outlet nipple

The instrumentation tower acted to retain the melt in the crucible and to channel effluent produced in the test so that it could be accurately measured. All sections of the tower were made of mild steel, except the laminar flow element which was stainless steel. Tubular sections were made of 8.9-cm-OD, 7.6-cm-ID pipe.

The seal between the instrumentation tower and the crucible is schematically drawn in Figure 2. A 3.8-cm nipple extended down from the base plate into the crucible cavity. The baseplate was sealed to the concrete with a compression seal of 22 layers of 0.13-mm-thick graphite sheets (Grafoil, Product of Union Carbide Corporation). Four 1.3-cm-diameter threaded rods were used to press the graphite sheets between the concrete and the steel base plate.

The steel baseplate was quite massive (30.5 x 30.5 x 2.5 cm thick), so that it would act as a large heat sink; it was also flat, for making the seal to the concrete.

Gases produced by the melt/concrete interaction passed through a 2.5-cm-diameter hole in the baseplate into the baffle section welded to the baseplate. The baffle section was 30.5 cm long. The baffle within this section was used to quench gases and to catch expelled solids so they would not perforate the instrumentation tower or interfere with measurements made in other sections of the tower. The baffle consisted of a 35.6-cm-long piece of 6.4-cm-OD, 5.1-cm-ID pipe. Two plates, each perforated by 20 holes 0.32 cm in diameter were affixed on the ends of the baffle. The baffle was filled with steel wool to increase the contact surface presented to gases entering the baffle. The baffle was held against

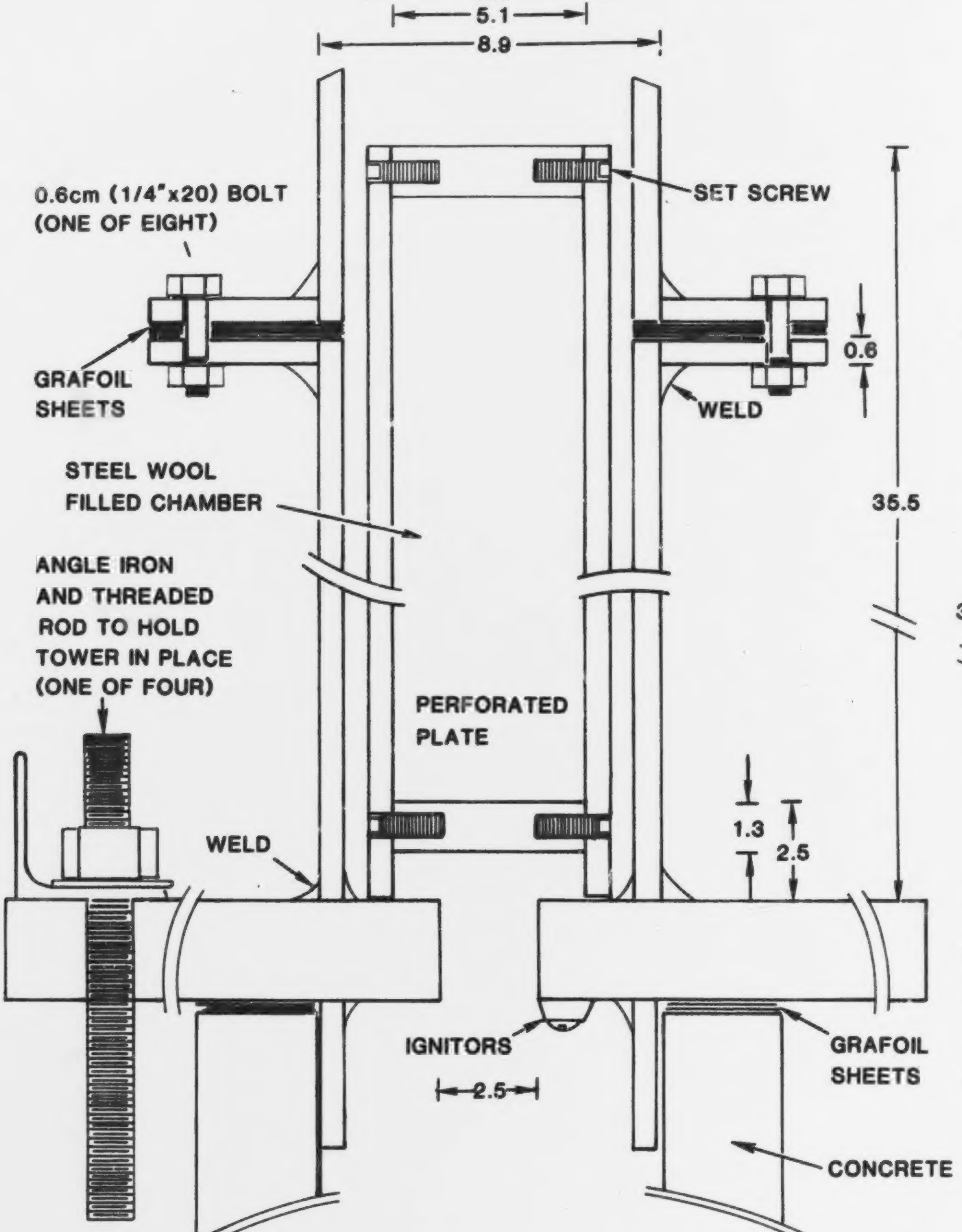
6.4
5.1
8.9
0.6cm (1/4"x20) BOLT
(ONE OF EIGHT)
SET SCREW
GRAFOIL
SHEETS
0.6
WELD
STEEL WOOL
FILLED CHAMBER
35.5
ANGLE IRON
AND THREADED
ROD TO HOLD
TOWER IN PLACE
(ONE OF FOUR)
30.5
PERFORATED
PLATE
1.3
2.5
WELD
2.5
IGNITORS
GRAFOIL
SHEETS
3.8
2.5
CONCRETE
15.2

Figure 2 Schematic Diagram of the Baffle Section of the Instrumentation Tower and the Arrangement for Sealing the Tower to the Concrete

BEST DOCUMENT AVAILABLE

the baseplate by a 0.6-cm-diameter rod extended from the top of the tower.

The baffle section was connected to a "T" section. This connection and other connections in the instrumentation tower were made with graphite compression seals similar to that between the tower and the concrete. Eight 0.63-cm-diameter (1/4" x 20) screws were used to hold four sheets of 0.13-cm-thick graphite sheets between 17.8-cm-square flanges (0.6 cm thick) welded to the ends of the tower sections.

Electrical wires for igniting the melt-forming reaction and two 0.32-cm-diameter, stainless-steel-sheathed, type K thermocouples to signal ignition extended from the top of the "T" section, through the baffle, and into the charge. Figure 3 is a photograph of the assembled crucible, baffle section, and "T" section.

A 91.4-cm arm connected to the "T" section was used to cool the gases further. The gases were sampled from this side arm. Twelve gas samples were drawn into remotely controlled, evacuated bottles during the test. Each bottle had a volume of 150 ml. The sampling line was 2 meters of 0.63-cm-OD, 0.32-cm-ID stainless steel. The sampling line was terminated within the cooling tower by a glass-wool-filled 1/4" Swagelok union. The glass wool prevented solid particulate expelled during the test from being drawn into the sampling line. The "dead" volume of the sampling line and the valving arrangements for the bottles was estimated to be about 25 ml. This "dead" volume was filled with air at the start of the test.

A Validyne model AP10 absolute pressure transducer on the sampling line was read through a Validyne model DM56A demodulator and recorded on a Soltec model VP-6232S strip chart recorder to signal when gas samples were extracted. Typical output from the line pressure transducer is shown in Figure 4. The data in the figure shows the sharp pressure drop in the sampling line pressure that occurs when a sample bottle opens. The pressure reaches a minimum at about 1 second after the bottle is opened. Line pressure recovers to ambient about 2.5 seconds after the bottle is opened. This would indicate that the error in the time of gas sampling is about 1 second and certainly less than 2.5 seconds.

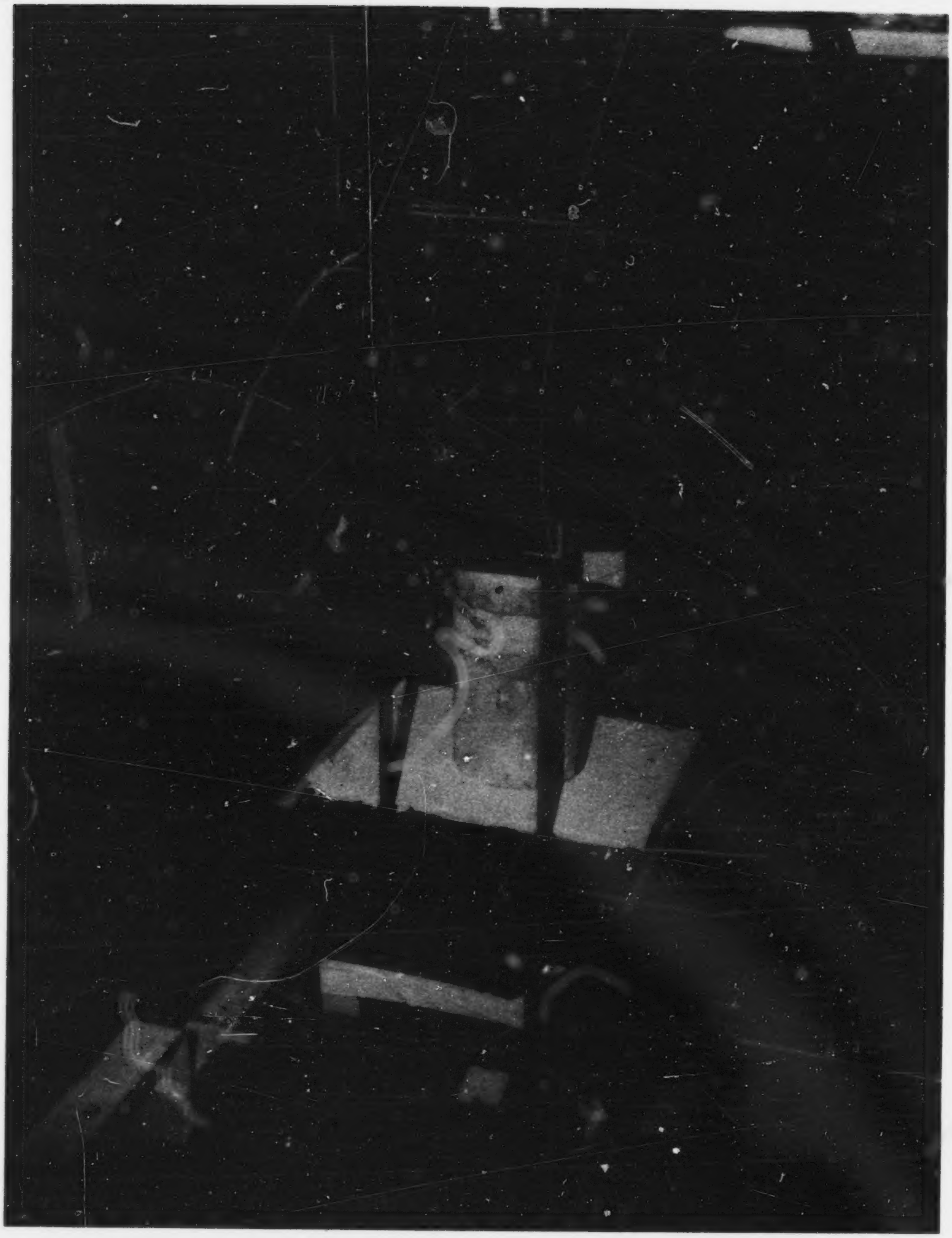

Figure 3 Photograph of the Assembled Crucible, Baffle Section, and "T" Section Used in Test BURN 1 (SAND Photo C78-6444)

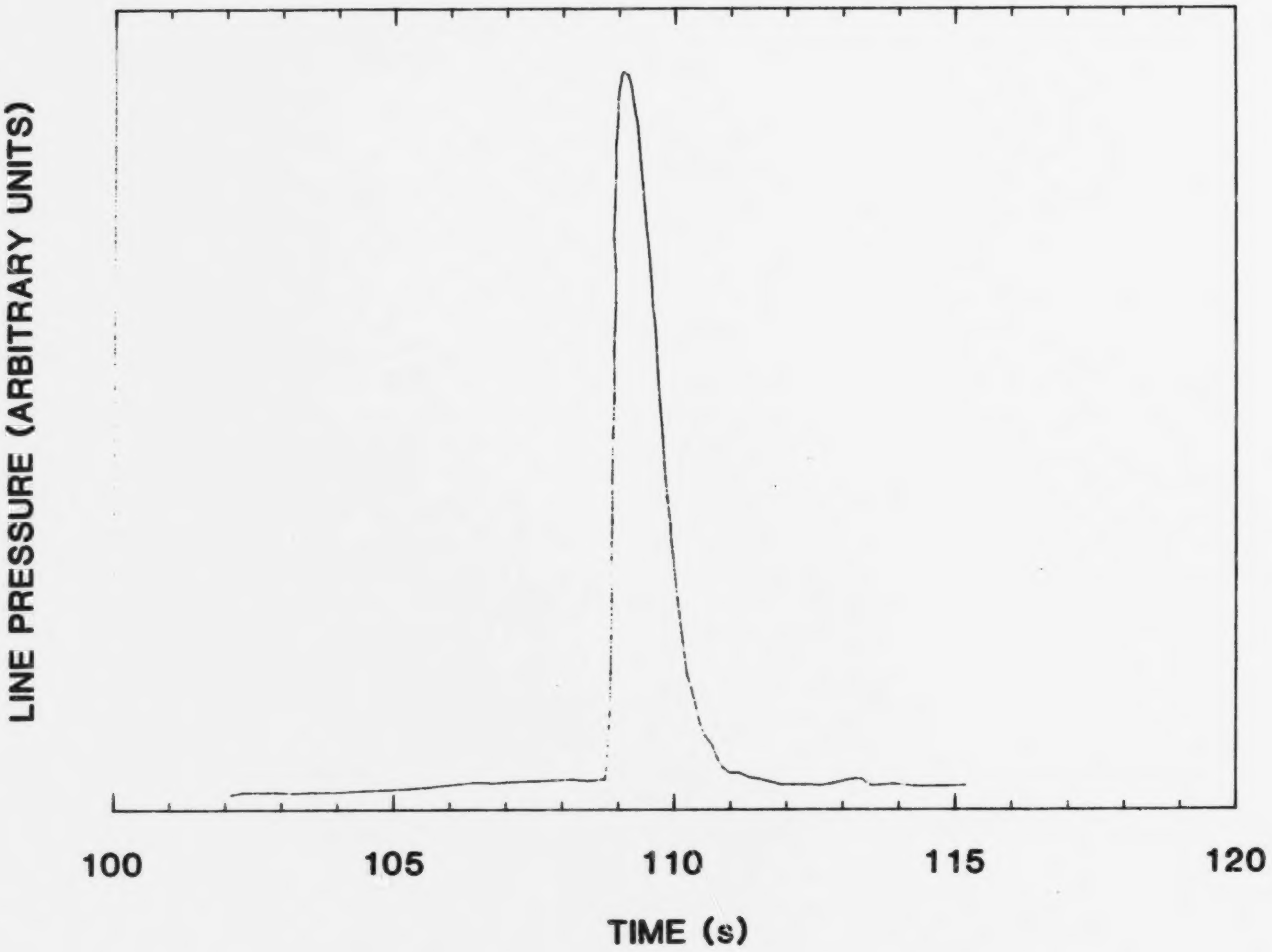

Figure 4 Typical Output from the Line Pressure Transducer During a Gas Sampling Event

The details of analysis of the gas samples drawn during this test have been discussed elsewhere (3). The method of analysis allowed determination of H_2, N_2, O_2, Ar, CO, CO_2, and hydrocarbons in the gas. The method was not suitable for determination of H_2O in the gas.

Gas flow measurements were made by following the pressure drop across a laminar flow element (Merriam Inc. Model 50 MY 15-3). Pressure measurements were made with a Validyne model AP10 1 psid differential pressure transducer. Output from this gauge was conditioned in a Validyne model MC1-3 signal demodulator and recorded on a Soltec Model VP6232S strip chart recorder.

The laminar flow element was calibrated with dry air before and after the test. The calibration curve was linear at flow rates greater than 40 liters/min ambient conditions (see Figure 5). The curve deviated from linear at lower flows. Only in this nonlinear region were differences in calibration between the pre-test and post-test determinations detected. These differences were quite small (see Figure 6).

Indicated flow data from the pressure drop across the laminar flow element could be corrected for the effects of gas viscosity, temperature, and pressure to get standard state flow by the formula:

$$F(\text{air})\ \frac{290}{T} \cdot \frac{\mu \text{air}}{\mu \text{gas}} = F\ (\text{gas})$$

F = flow rate, T = absolute temperature, μ = viscosity

Various methods for calculating the viscosity of a gas mixture are shown in Appendix A.

The laminar flow element was connected to the cooling section and the outlet nipple with graphite compression seals. Flanges on the element were 2.5-cm-thick and the compression seals were made with four 2.5-cm-diameter bolts on each flange.

A 1-mm-diameter, stainless steel sheathed, type K thermocouple was located near the outlet of the laminar flow element to measure gas temperature. This thermocouple indicated that the gas temperature did not deviate from the ambient temperature (27°C) throughout the monitored portion of the test (~300 seconds).

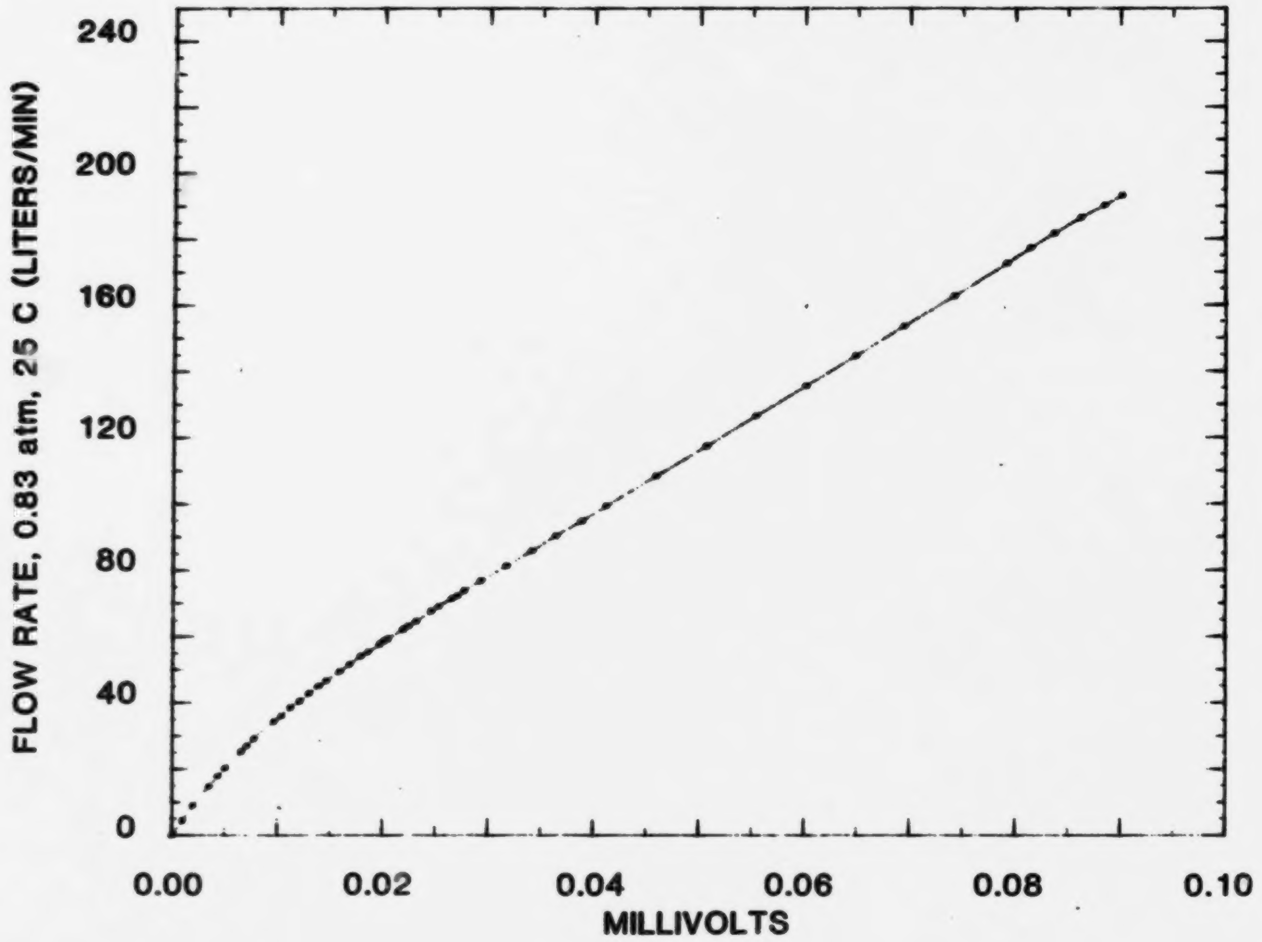

Figure 5 Calibration Curve for the Laminar Flow Element Mounted on the Sidearm of the Instrumentation Tower Used in Test BURN 1

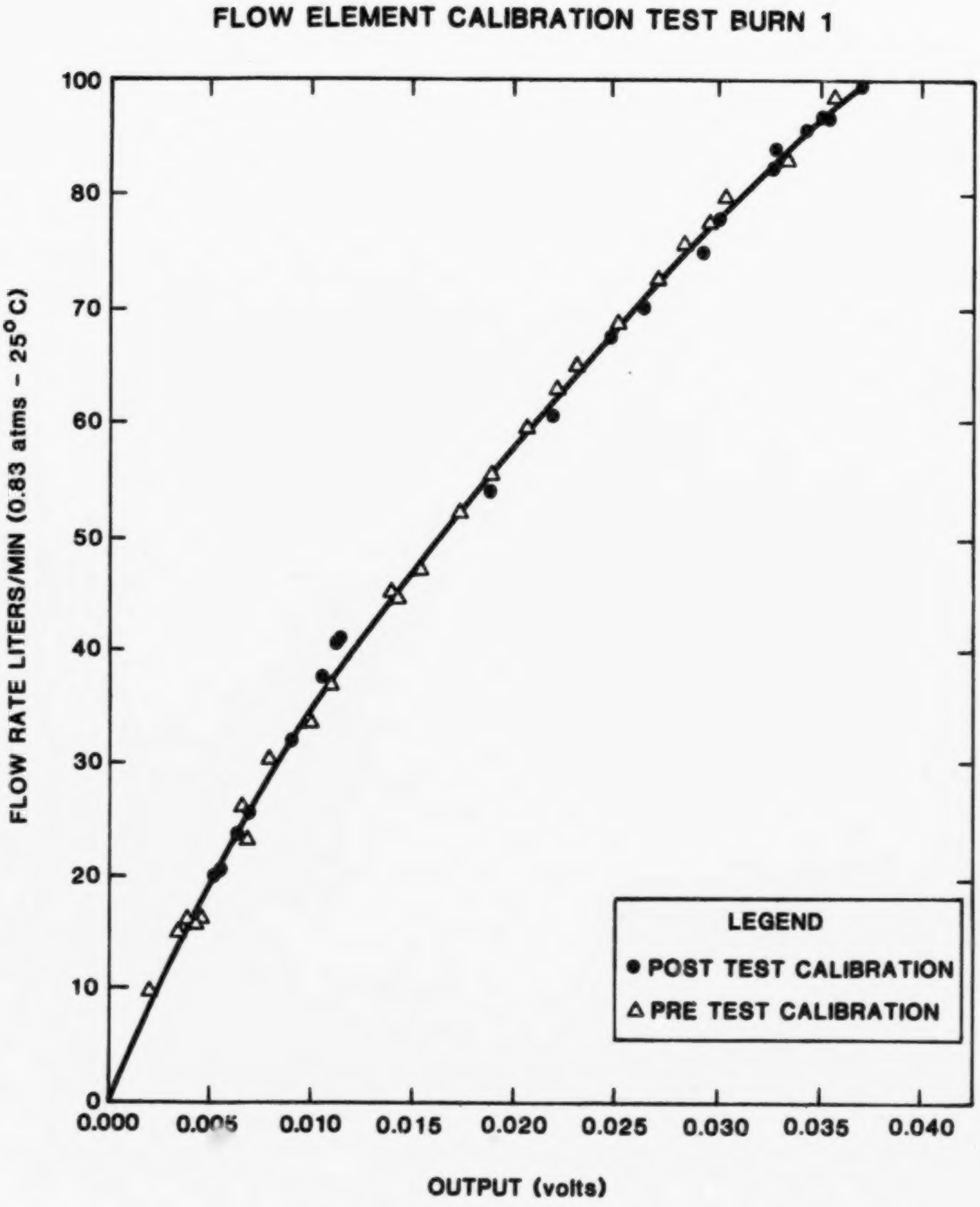

Figure 6 Comparison of Calibration Data Taken Before and After Test BURN 1

BEST DOCUMENT AVAILABLE

The x-ray beam used in the test was obtained from a Linatron model 1500 pulsed x-ray source (Varian product). The x-ray voltage was 7.5 Mev. The dose rate was about 500 rads/min.

Image collection was done with a Decalix-SI image intensifier (product of N.V. Optische Industrie De Oude Delft, Delft, Holland). This device has a 32-cm fluorescent screen that is excited by x-rays emerging through the test fixture. The screen is flat and was carefully aligned normal to the x-ray source so that the x-ray image was undistorted. The device used an Isocon television camera tube (4). The television image consisted of 625 lines interlaced at 25 f/s. The television band width is 7 MHz. The maximum resolution by the television camera tube is 9 line pairs/cm. This resolution is far in excess of that estimated for the x-ray image. The video taped image obtained from the image intensification system was photographed on 16 mm film by Byron Laboratories. Analysis of the test results was made from this motion picture.

Figure 7 is a photograph of the x-ray source, image intensifier, and the test fixture.

The charge used in the melt-forming reaction was 1972 g of a mixture consisting of 76.3 w/o Fe_3O_4 and 23.7 w/o Al. The mixture was electrically ignited with Pyrofuze. Appendix B presents further discussion of the reaction characteristics of this charge. If the reaction proceeded to completion it would yield 1088 g of iron and 884 g of aluminum oxide. The maximum, adiabatic, reaction temperature of the mixture is 2870°C. Posttest analyses suggest that the reaction did not go to completion and the initial temperature of the melt formed during the reaction was probably less than the adiabatic maximum (See Appendix B).

The thermal behavior of the metal phase produced by the metallothermic reaction was determined by differential thermal analysis. A 72-mg sample held in an aluminum oxide cup was heated at 20°C/min in an argon atmosphere with a Dupont 1600°C differential thermal analysis unit. Sintered aluminum oxide was used as the reference material. Both the sample and the reference were covered by a platinum radiation shield. The thermogram is shown in Figure 8.

BEST DOCUMENT AVAILABLE

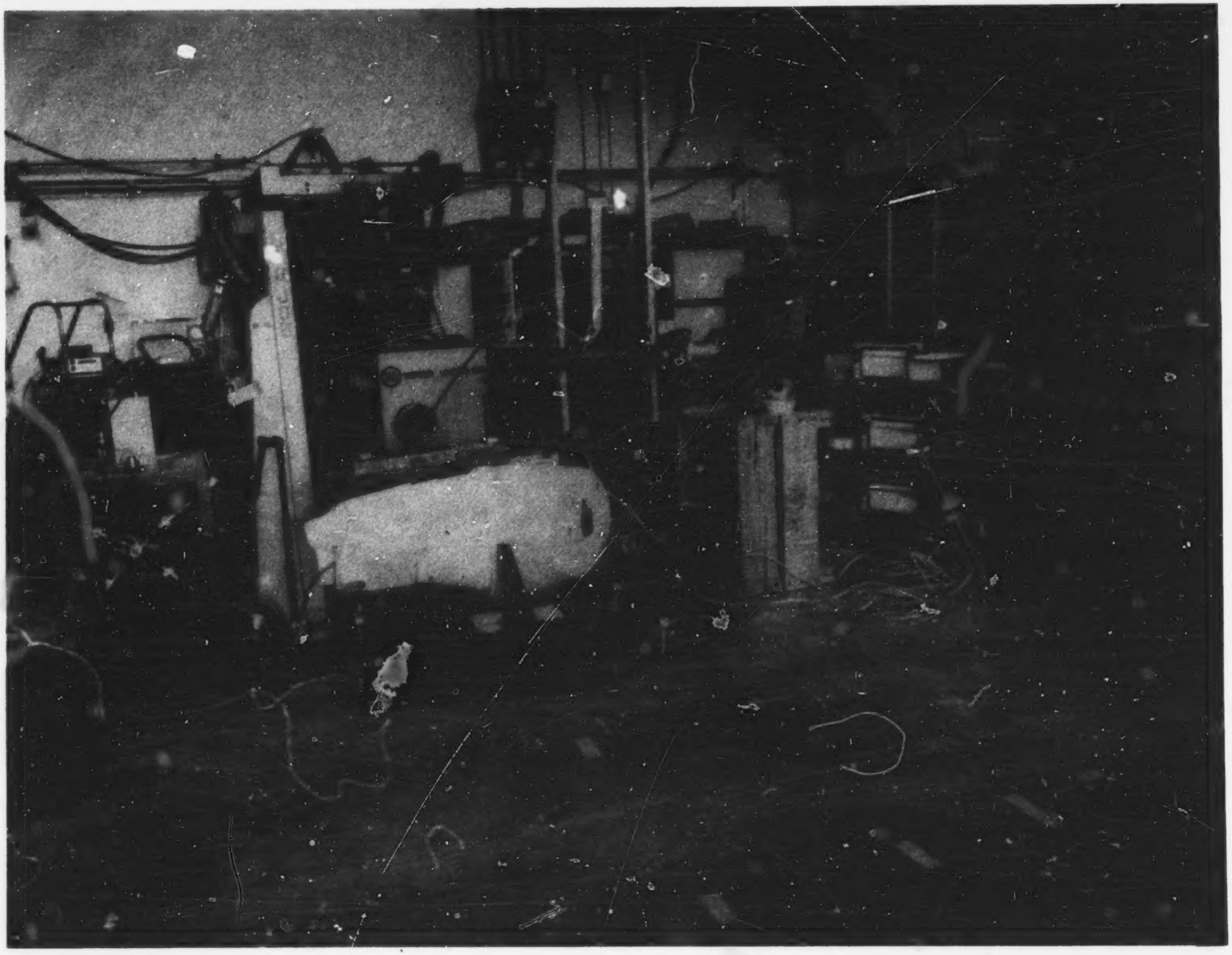

Figure 7 Photograph of the X-ray Source, Image Intensifier and the Instrumentation Tower as Used in Test BURN 1 (SAND Photo C78-6445)

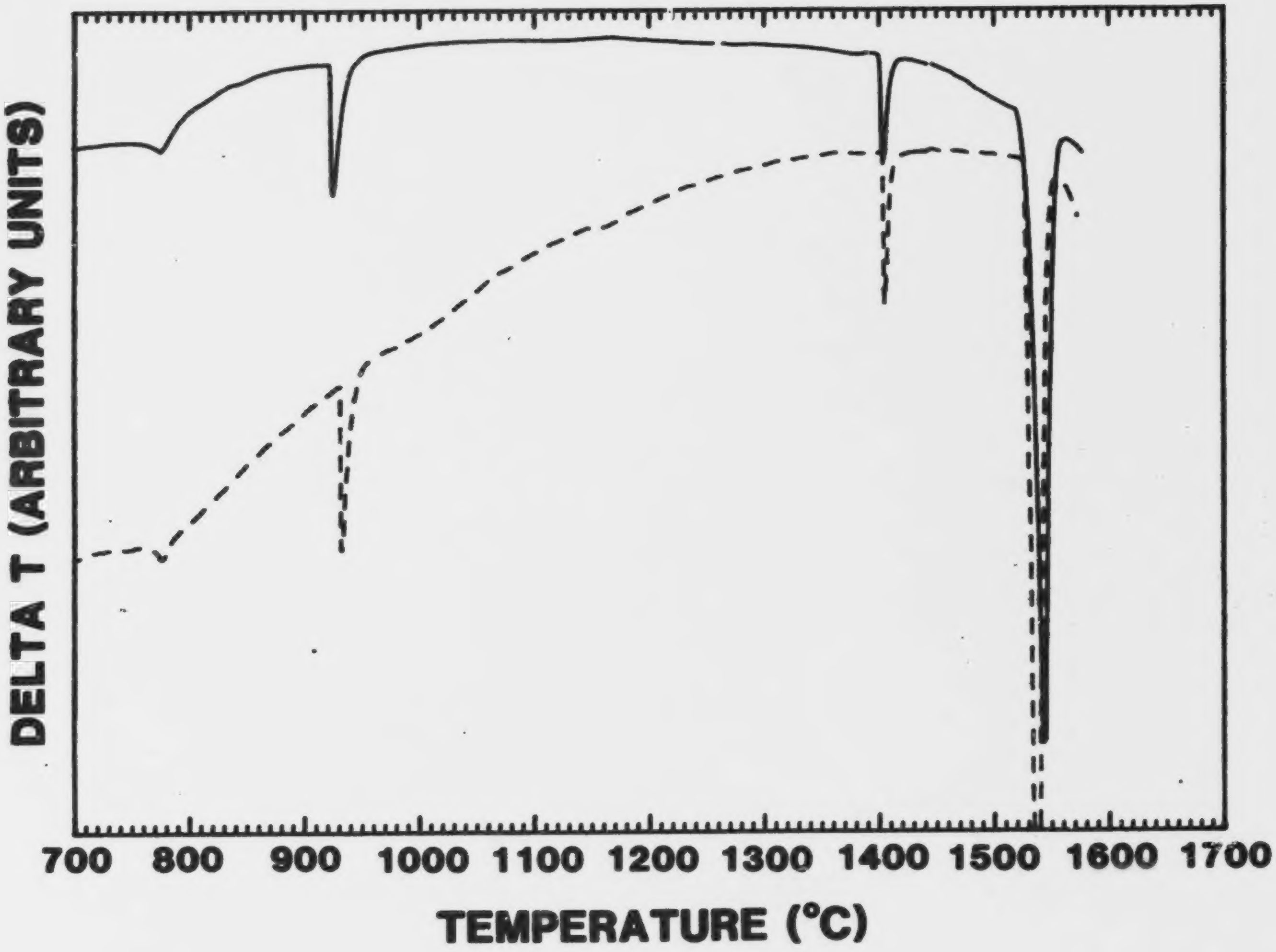

Figure 8 Differential Thermogram of Metal Phase Formed by the Metallothermic Reaction in Test BURN 1 (Solid line). Differential Thermogram of pure iron shown as a dashed line

BEST DOCUMENT AVAILABLE

The concrete used in test BURN 1 has been extensively characterized elsewhere (3). The chemical composition of the concrete is shown in Table II. A differential thermogram of the material is shown in Figure 9. The concrete contained 2.8 w/o water that could be volatilized at temperatures less than 200°C. An additional 2.1 w/o water is lost between 300°C and 500°C. The concrete contained 20.96 w/o CO_2 that could be liberated from the calcareous aggregate over the temperature range of 600-1000°C. A phase transition of the free silica in the concrete produces an endotherm in the thermogram at about 575°C.

TABLE II Chemical Composition of Limestone/Common Sand Concrete

	Wt %
Fe_2O_3	1.44
Cr_2O_3	0.014
MnO	0.03
TiO_2	0.18
K_2O	1.22
Na_2O	0.082
CaO	31.2
MgO	0.48
SiO_2	35.7
Al_2O_3	3.6
CO_2	20.96
SO_2	0.2
Evaporable H_2O	2.8
Bound H_2O	2.1

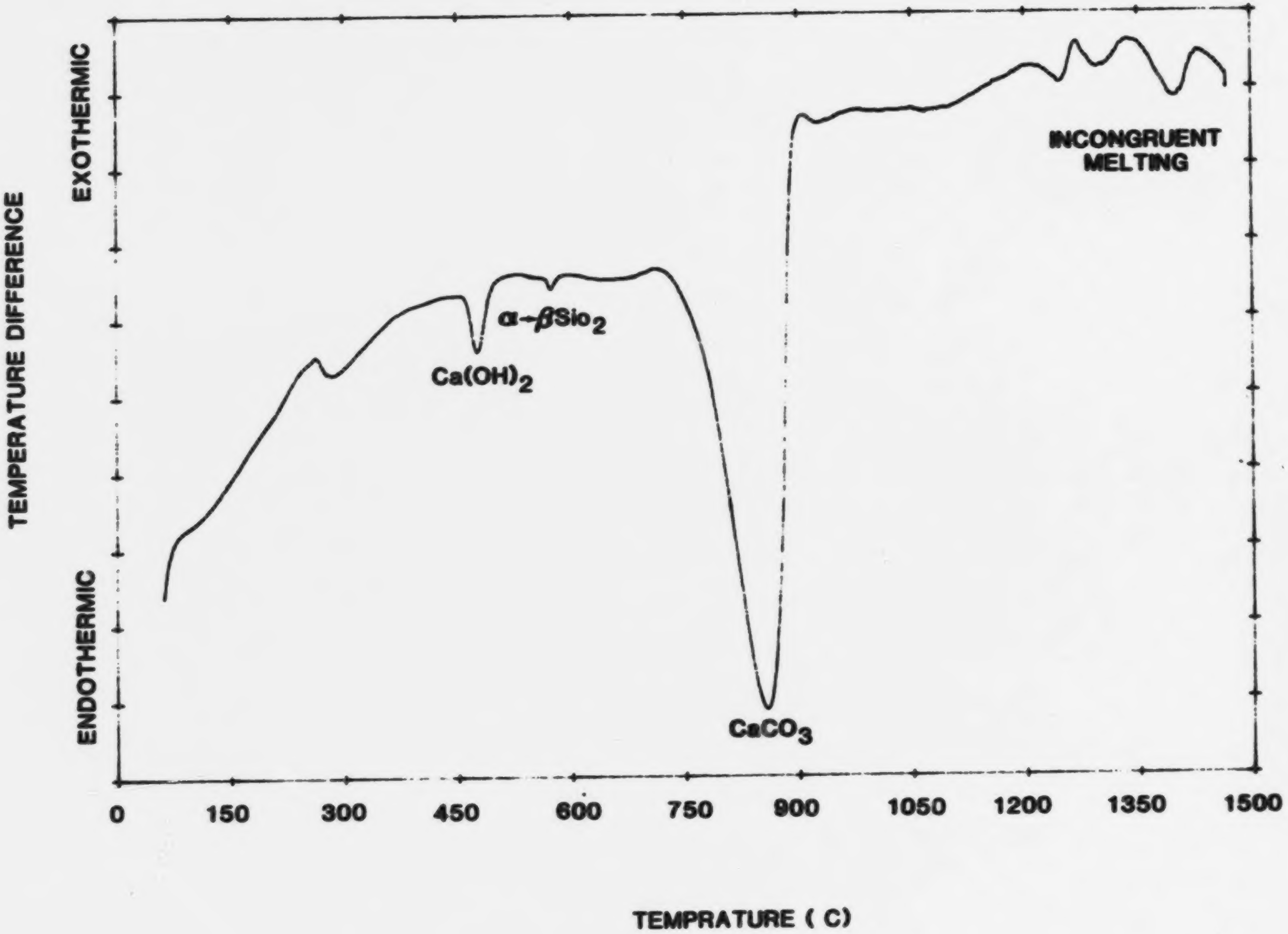

Figure 9 Differential Thermogram of the Limestone/Common Sand Concrete Used in Test BURN 1

II. Performance of the Image Intensification System

At the start of the test, the x-ray image of the crucible cavity had no distinguishing features. Only the edges of the nipple from the baseplate were resolved. The crucible cavity could not be distinguished because the unreacted charge and concrete have similar densities (2.6 and 2.34 g/cm^3) and effective atomic numbers.

A beat frequency developed from the combination of the pulsing of the x-ray source and the scanning of the video camera and produced a bright horizontal bar in the image. This bright bar would migrate up through the image during the test. The bar was bright enough to obscure any image on the screen it crossed.

Once the metallothermic reaction ignited, the melt front and the outline of the cavity could be clearly seen. The metallic portion of the melt was most clearly seen. Oxide phase could be distinguished from the metal by its slightly less opaque image.

A bright halo developed around the metallic phase where it was adjacent to the concrete. The cause of the halo is uncertain. The most obvious causes are the diffraction of x-rays at the sharp melt edges or refraction of x-rays at the discontinuity in material density.

The halo was the major cause of loss of resolution in the image. It was estimated that dimensions could be resolved to no better than ± 0.3 cm. If a continuous gas film between the melt and concrete were to exist, it could not be definitively identified in the x-ray image. A theoretical analysis of the x-ray system and experiments with fine grain x-ray film have shown that the resolution limit with the system is about 0.6 mm. Obviously, real time imaging and the presence of the melt substantially degraded the resolving power of the system. Modern image processing methods could be used to recover some of the lost detail. It is doubtful that these methods could be used to reduce the resolution limit below 0.6 mm.

The x-rays produce a two-dimensional image of the three-dimensional melt. There is no depth to the image and deduction of perspective from the image of the small BURN 1 test is difficult.

Many of the difficulties encountered with the x-ray image, though not the lack of perspective, could be relieved by further enhancement of the video record. Computer averaging of images would improve the image quality with only a modest loss in time resolution. None of this image enhancement has yet been tried.

In spite of the "halo" effect, and the lack of perspective in the image, the image intensification technique provided an outstanding view of melt behavior during interaction with concrete.

III. Test Results

A collection of still photographs of the projected image of the motion picture test record are to be found in Appendix C. The image quality was significantly reduced in this photographic process. Table III lists major events in the melt behavior.

Once ignition of the melt-forming charge began, a distinguishable image could be seen in the test record. The reaction front propagated downward at a uniform velocity of about 5 cm/s. The front was slightly concave - the front on the cavity axis was about 1 cm ahead of the front near the cavity walls. Once the reaction front touched the bottom of the crucible cavity, stratification of the melt into a dense metal layer and an almost transparent (to x-rays) oxidic layer could be easily seen. Stratification may have been well developed before completion of the reaction. Stirring of the melt during reaction and the "halo" effect made it difficult to detect the limits of the oxide phase prior to the melt contacting the cavity bottom.

Immediately after contact with the cavity bottom, the melt was relatively quiet. Two mild surges in the melt occurred about 1 second after contact. These surges were apparently due to gas jets from the cavity walls.

About 2.25 s after contact of the melt with the cavity bottom (4.67 s after ignition) there was a violent eruption of gas. The gas was able to completely levitate the melt. The melt did not levitate as a coherent mass. Rather it was dispersed into globules and stringers. The period of violent gas eruption kept the melt at least partially levitated for about one second. At 5.5 s the molten pool had reformed. Its volume -- especially the volume of the oxide phase -- was definitely less after the violent eruption. Posttest inspection of the instrumentation tower showed that significant quantities of aluminum oxide had frozen to the exposed base plate and within the baffle chamber. The baffle pipe in the chamber was locked firmly in place by the frozen oxide. No metallic phase was detected in the frozen material. Frozen oxidic material also coated the cavity walls. After the first violent eruption, very little of the molten pool could have been oxidic material.

Concrete was largely transparent to x-rays in the test. Consequently, it was not possible to tell if the violent eruption of the melt was associated with spallation of concrete. The observed delay between melt contact and melt levitation is consistant with observed concrete spallation during melt/concrete interactions reported elsewhere (3). The "halo" effect and the nature of the projected image made it difficult to ascertain if the cavity had been enlarged due to spallation. The limits of the cavity did appear less sharply defined. Clearly, the depth of any spallation that did occur was small ($<$ 3 mm). This is consistant with previously observed spallation behavior of limestone/common sand concrete (3).

Three other violent eruptions of the melt occurred at about 6.45, 8.2 and 10.5 s after the start of the test. None was so effective at levitating and dispersing the melt as the first eruption. Throughout the period of 4.7 to about 22 s after the start of the test there were minor eruptions of the melt that caused globules or stringers of liquid melt to be thrown up from the pool.

About 29 s after ignition of the melt-forming reaction, a frozen or glassy crust of low x-ray density material began to form above the high x-ray density metal pool. The crust was thickest at the sides of the crucible cavity. There was insufficient material present to completely span the crucible cavity. Posttest inspection of the crust showed it to be the green glass typical of melt interactions with the limestone/common sand concrete. Because the material was a glass no "melting point" could be determined. The glass did deform and flow at 1200°C.

Throughout the first 20 s of the test no distinct pattern of gas ejection into the melt was obvious. Over the course of the next 20 s some preferred locations for bubble formation developed. Thirty-two seconds after the start of the test almost all of the gas bubbles formed at locations on either side of the cavity axis, at the cavity

Table III Events of Melt Behavior in the Test

Event	Time after Thermite Ignition (s)	Time after Melt Contacts Bottom of the Crucible Cavity (s)
1) Ignition of thermite	0	--
2) Melt contacts the bottom of the cavity	2.42	0
3) Mild surges in melt	3.38 & 3.58	0.96 & 1.16
4) Violent eruption of gas completely levitates and disperses the melt	4.67	2.25
5) Molten pool reforms after the violent surge	5.50	3.08 s
6) Other major eruptions of melt	6.45, 8.2 & 10.5	4.23,5.8 & 8.1
7) A crust of slag forms above the molten pool	29.04 - 38.58	26.62 - 36.16 s
8) Localized bubbling well-developed	35.17	32.75
9) Molten metal becomes viscous enough that distinct bubbles form at the surface	56.42	54.00
10) Pool behaves as a stiff rather than fluid body	63.17	60.75
11) Solidification of the melt is complete	68.04	65.62

bottom, and at locations just below the metal pool surface on the cavity walls.

Frame-by-frame analysis of the motion picture record at the nine locations noted in Figure 10 was used to make quantitative estimates of the time during which melt was in contact with concrete. Intimate melt-concrete contact could not be ascertained from the record because of the "halo" effect. Contact was assumed if the melt was separated from the concrete by less than 6 mm. The estimates of contact do not refer to the presence or absence of a continuous gas film. The distortion due to recording the three dimensional pool on film may also have affected the judgement of whether melt was in contact with the concrete.

Data were averaged over one second intervals to obtain the percent of time melt was in contact with concrete at the location of interest. The average contact time and the associated standard deviations are listed for 10 second intervals in Table IV. Data on the time of contact at the nine locations are plotted with time in Figures 11 to 19. Error bars in these figures are ± 1/N and ± 1 s where N is the number of useful frames in the 1 s interval monitored. (Many frames were not used because the image was obscured by the bright horizontal bar described above.) The error in the percent of contact time thus varied between ± 25% and ± 4%. Note that melt froze away from the concrete at locations P1, P3, P4, P5, and P6.

The melt contact pattern was approximately symmetrical about the cavity axis. The melt at points near the top of the metal pool (P1 and P9) contacted the concrete only 40 to 50% of the time. Most of time, separation of the melt from the concrete at these points was caused by a continuous flow of gas rather than distinct bubbles. Melt contacted the cavity wall near the bottom of the cavity (P2 and P8) 80-90% of the time. Similarly, melt was in contact with concrete at the bottom of the cavity near the walls (P3 and P7) much of the time. Contact at these locations near the intersection of the walls and the cavity bottom was, of course, much less early in the test when melt was being violently levitated than later in the test when more regular gas injection occurred.

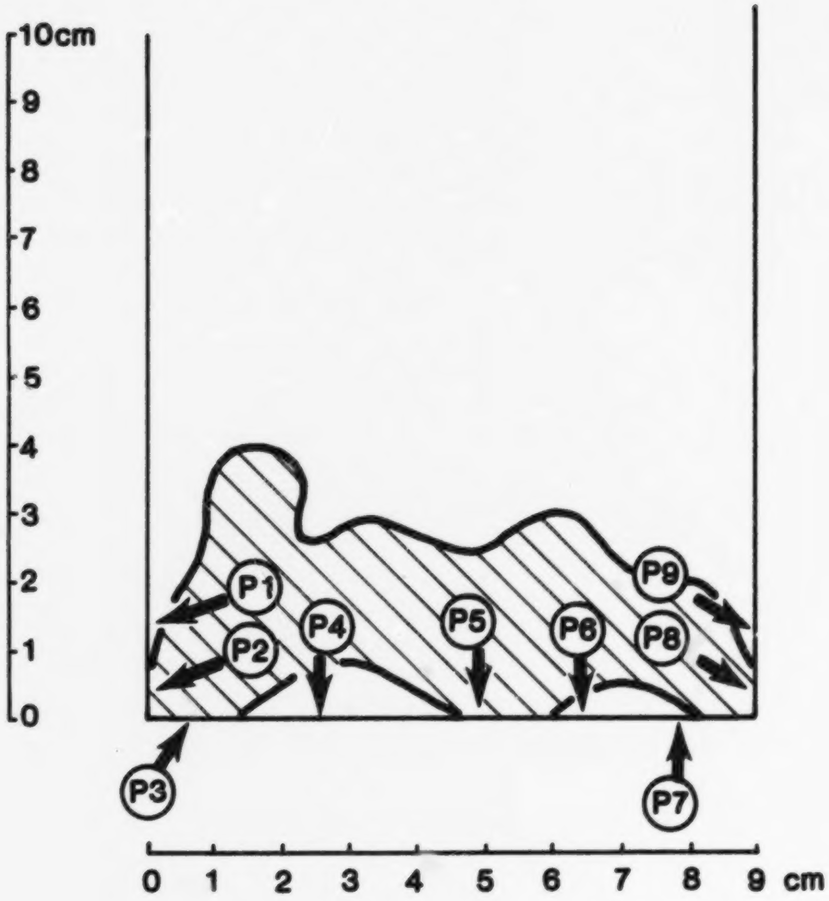
10cm
9
8
7
6
5
4
3
2
1
0
P1
P2
P3
P4
P5
P6
P7
P8
P9
0
1
2
3
4
5
6
7
8
9 cm

Figure 10 Locations Monitored to Determine the Fraction of Time Melt Spent in Contact with the Concrete

Table IV Percent of Time Melt in Contact With Concrete at Various Locations and During Various Time Intervals

Location**	Time Interval (s)*							
	0-9	10-19	20-29	30-39	40-49	50-59	60-67	0-67
P1	31(6)	56(5)	46(4)	48(3)	51(5)	33(4)	4(7)	40(20)
P2	59(9)	87(6)	92(1)	93(1)	89(2)	88(1)	91(4)	86(16)
P3	66(10)	89(6)	97(1)	96(2)	84(3)	68(6)	42(9)	79(20)
P4	19(5)	29(13)	33(6)	31(3)	12(2)	13(2)	3(3)	21(18)
P5	59(5)	74(4)	89(4)	95(2)	94(3)	83(7)	66(4)	80(16)
P6	64(15)	48(7)	29(4)	30(2)	17(3)	9(3)	7(1)	30(23)
P7	40(3)	48(6)	79(14)	91(2)	79(5)	73(2)	62(1)	68(22)
P8	84(3)	92(2)	94(1)	97(1)	95(1)	91(4)	90(2)	92(9)
P9	25(5)	40(4)	44(4)	48(1)	46(3)	41(3)	68(16)	45(22)

---

*Mean % of time that melts contact concrete is outside the parentheses. The standard error of the mean is inside the parentheses.

**Locations depicted in Figure 10.

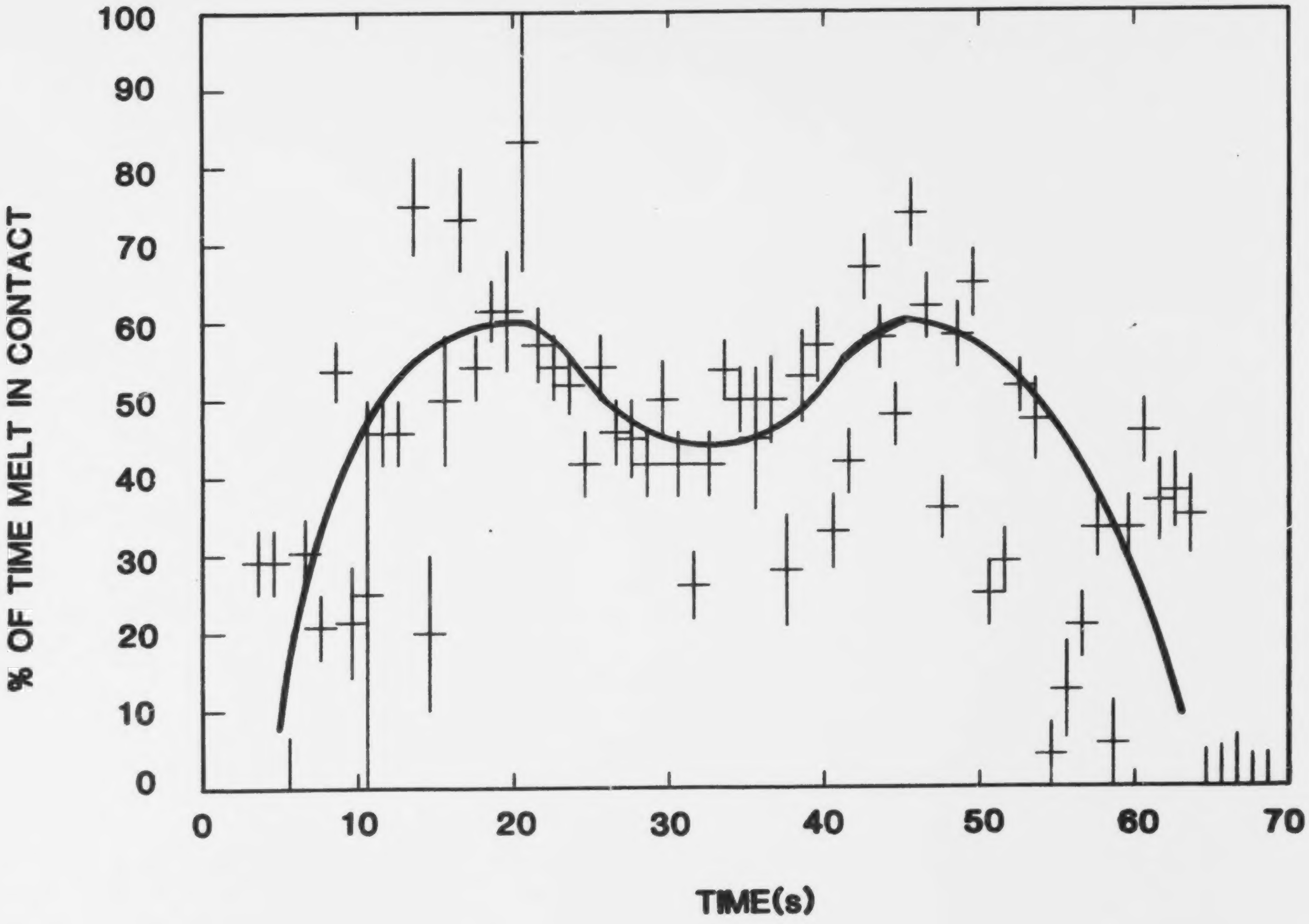

Figure 11 Melt Contact at Location P1

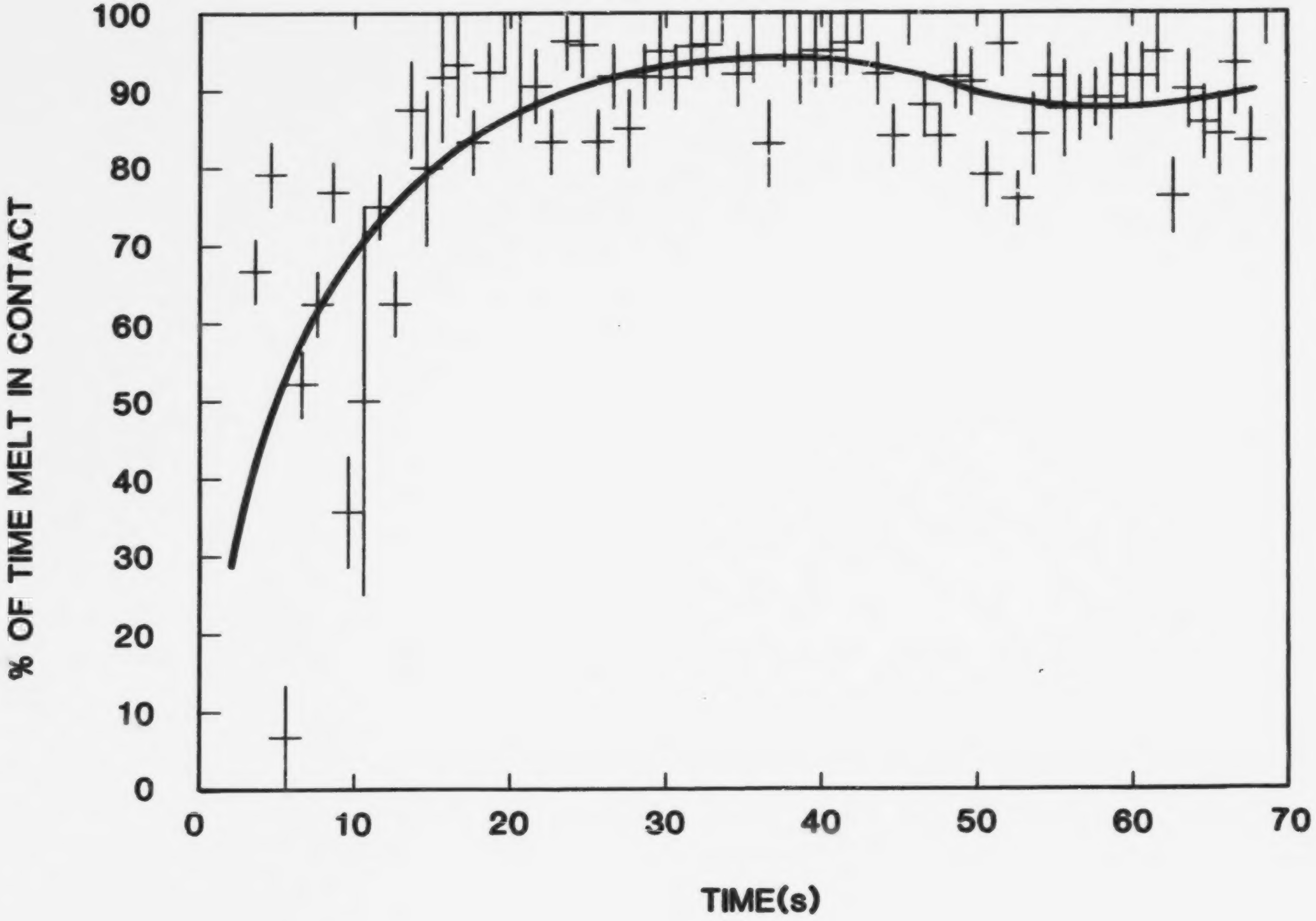

Figure 12 Melt Contact at Location P2

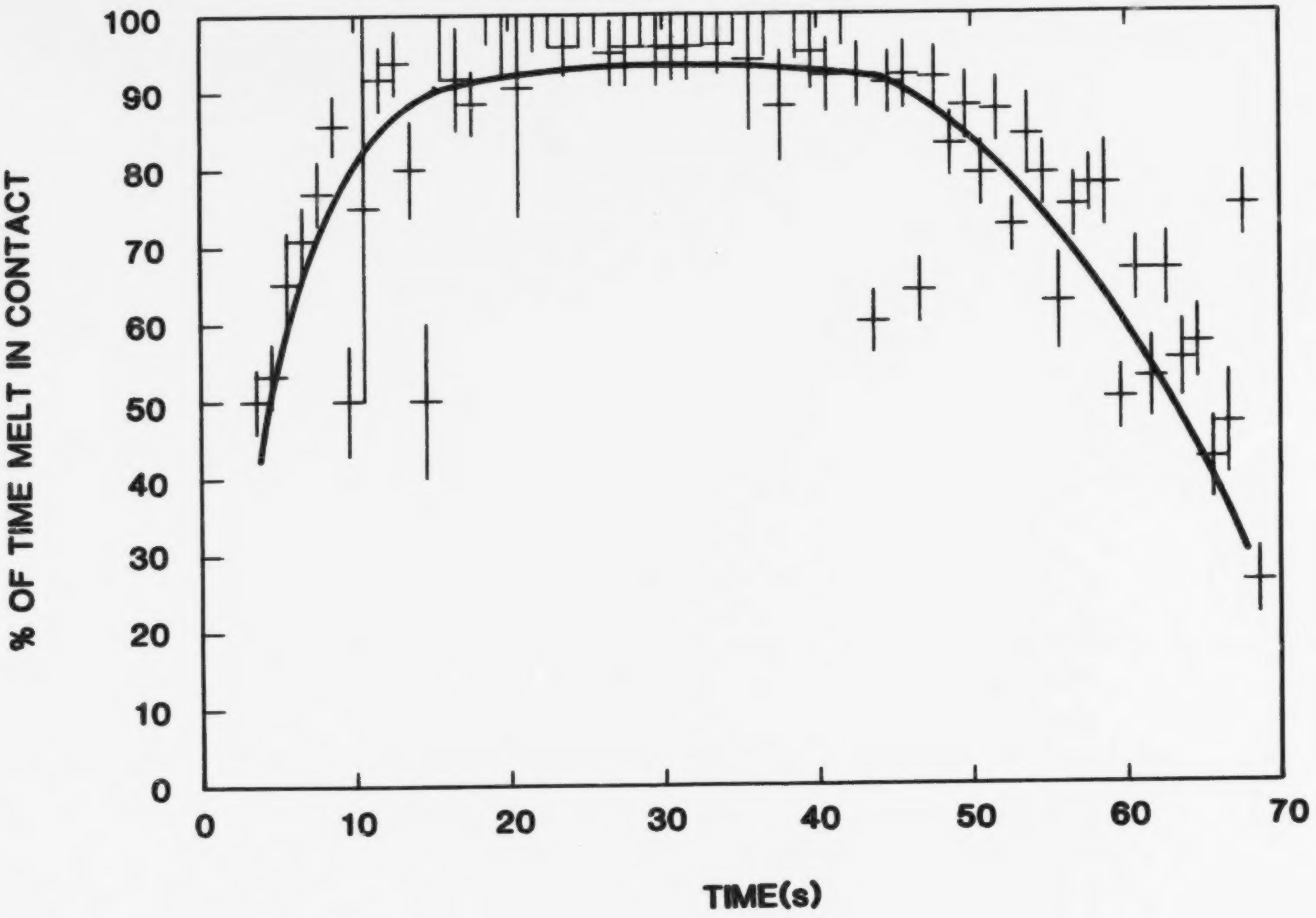

Figure 13 Melt Contact at Location P3

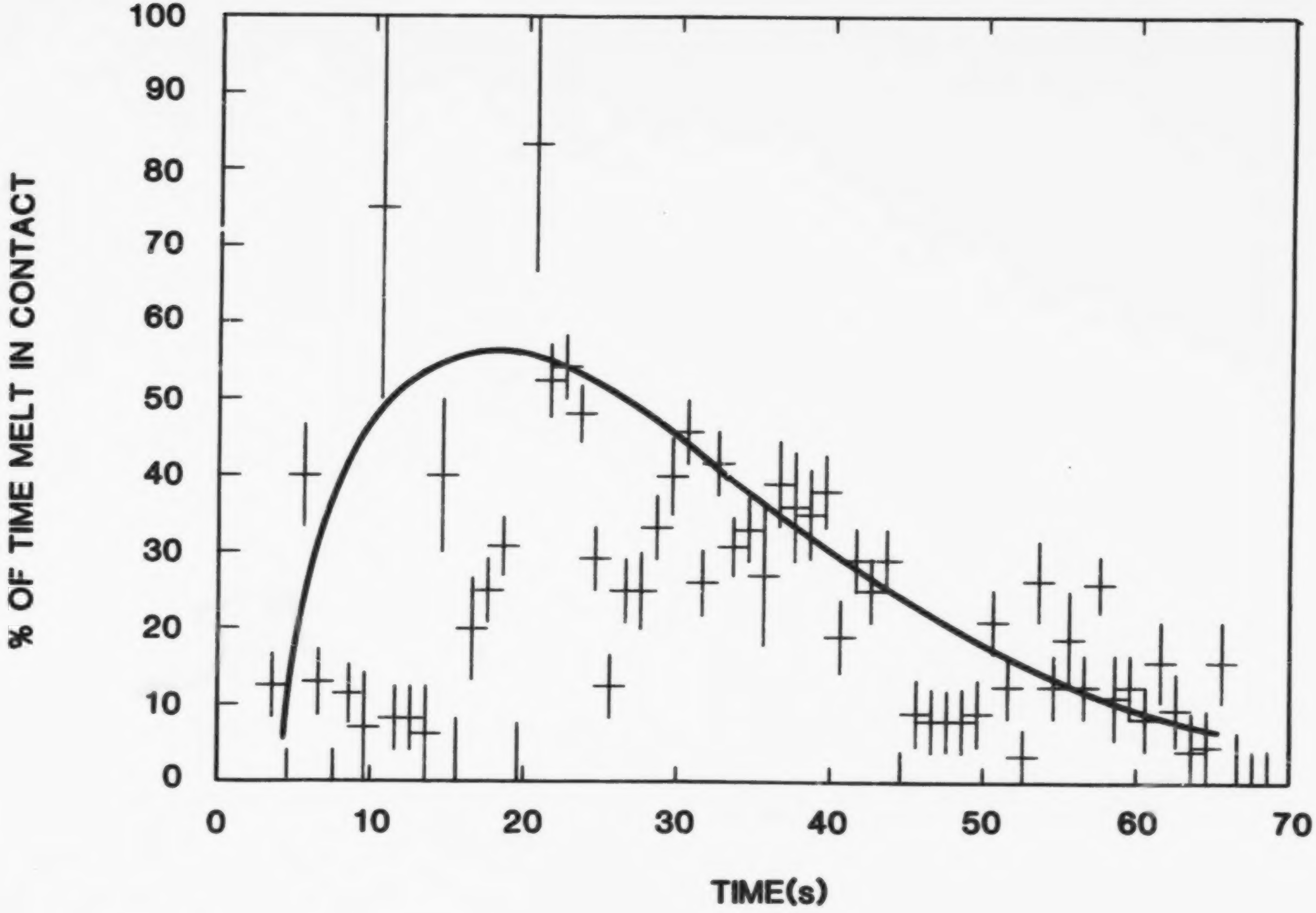

Figure 14 Melt Contact at Location P4

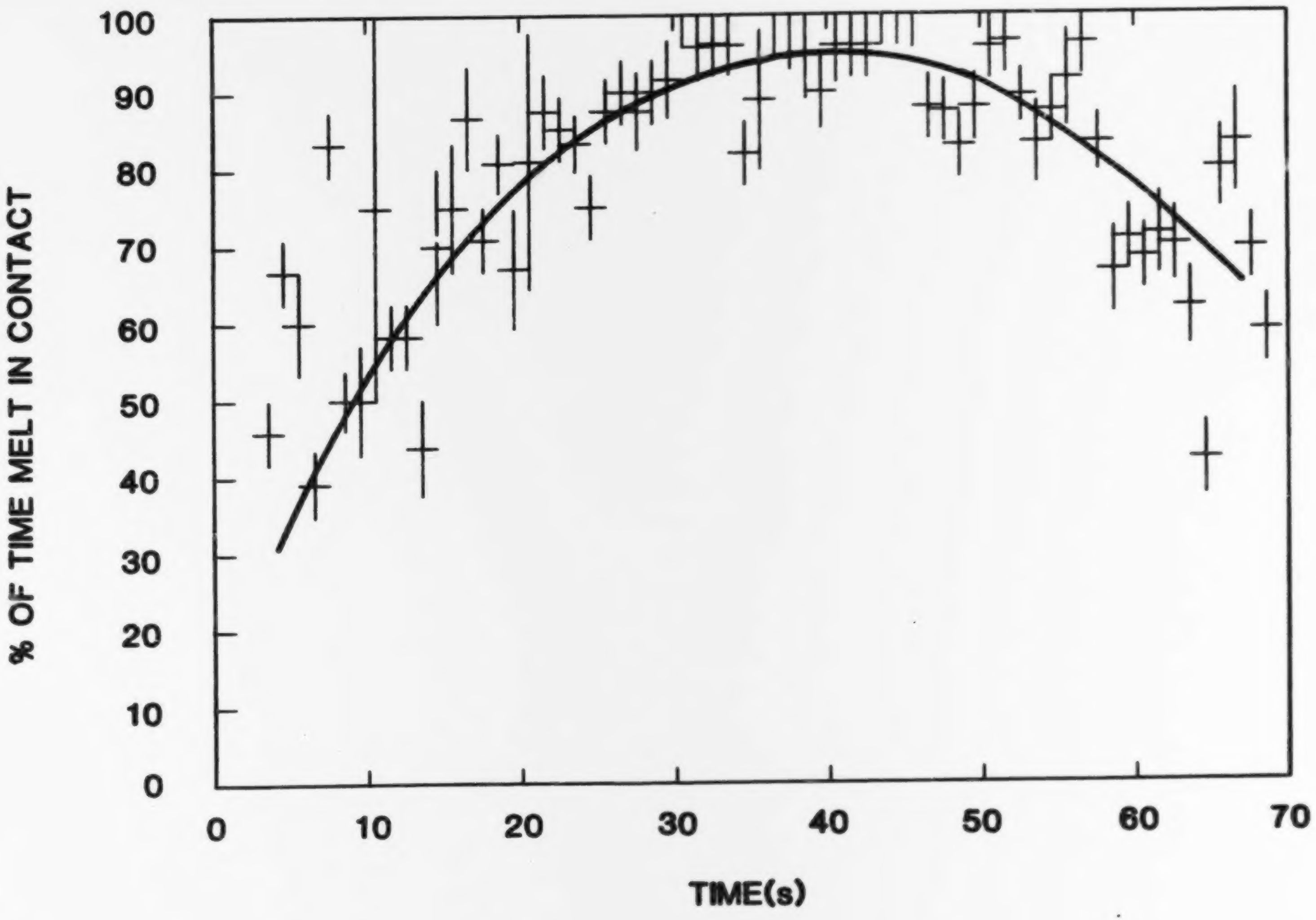

Figure 15 Melt Contact at Location P5

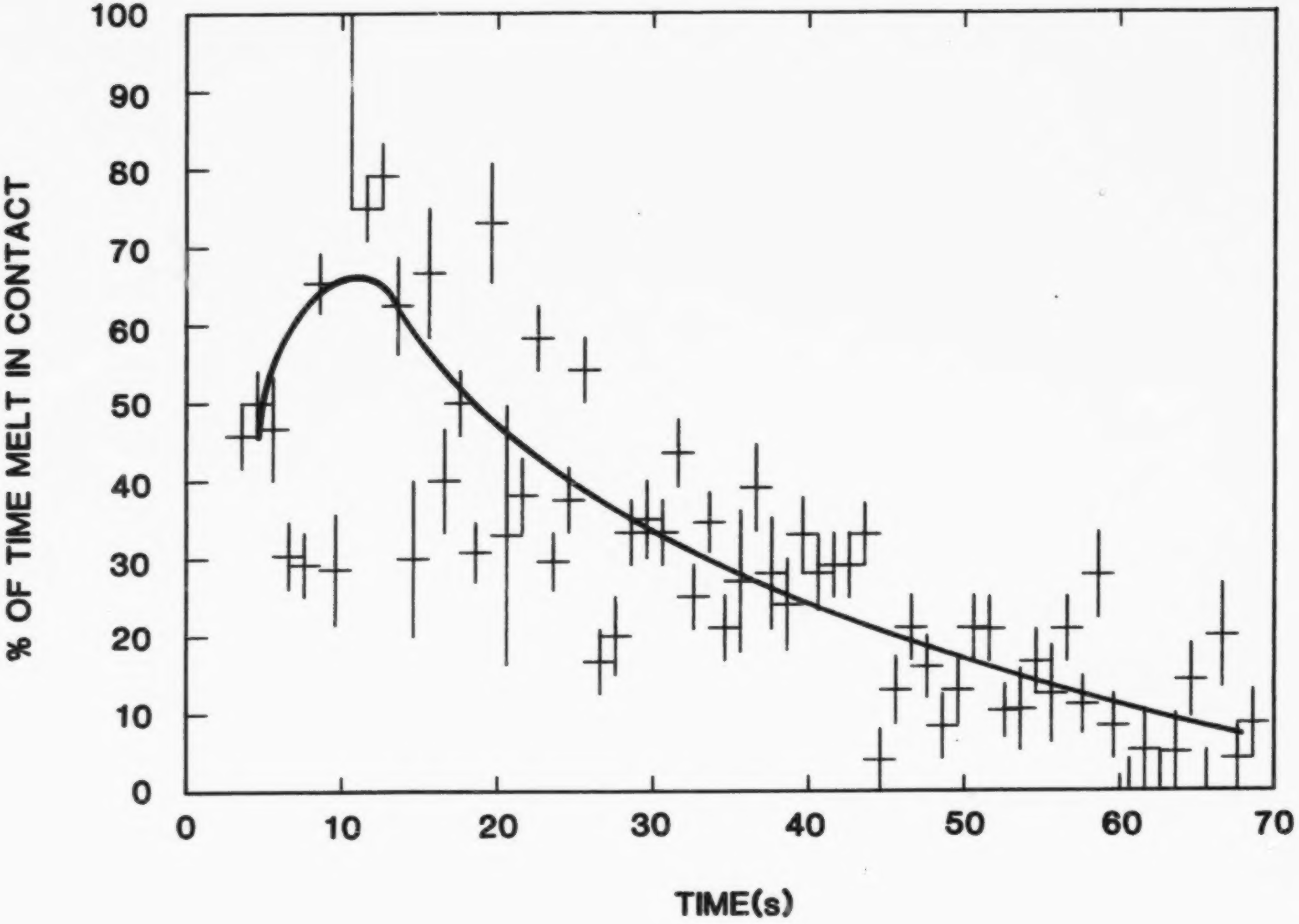

Figure 16 Melt Contact at Location P6

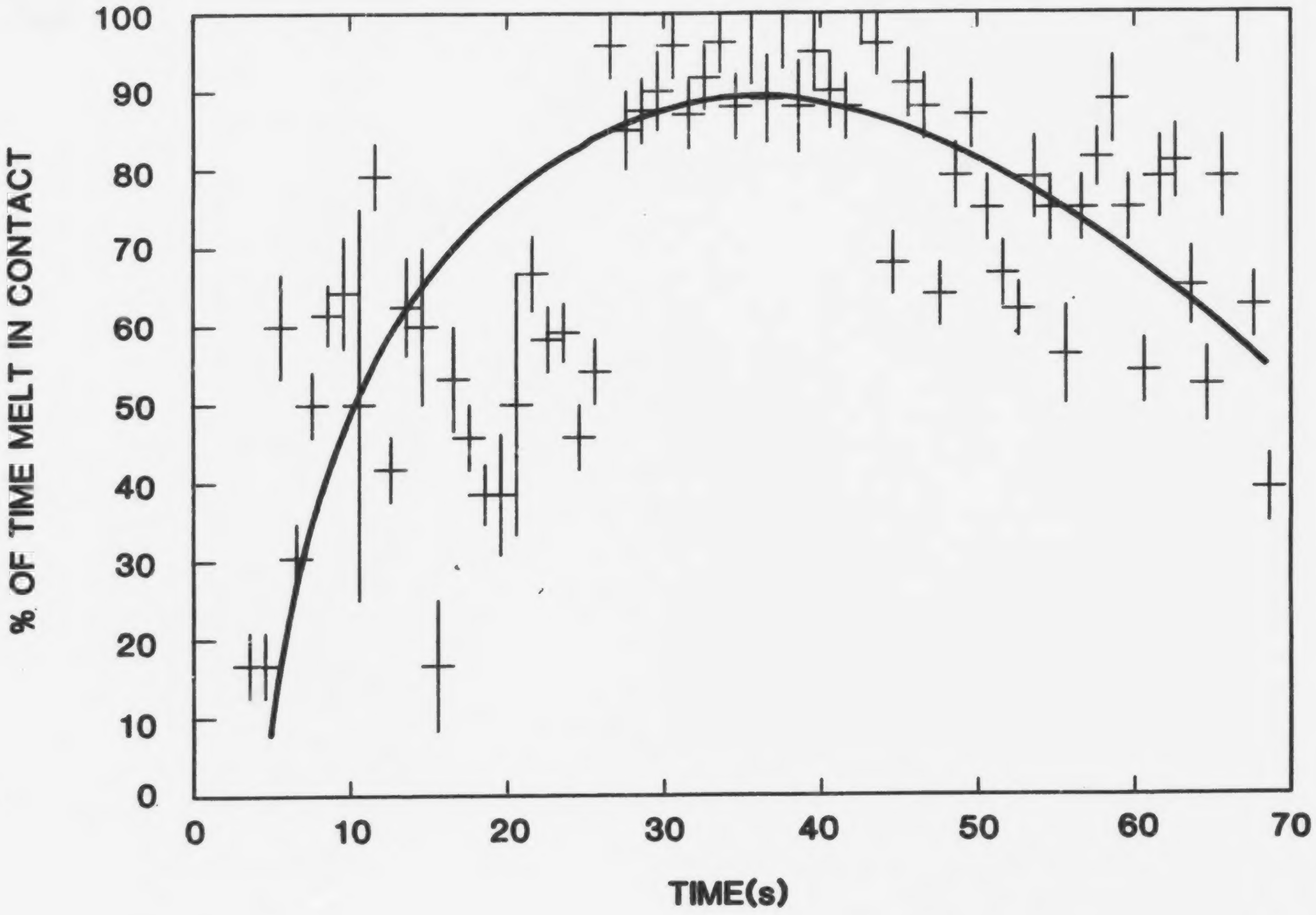

Figure 17 Melt Contact at Location P7

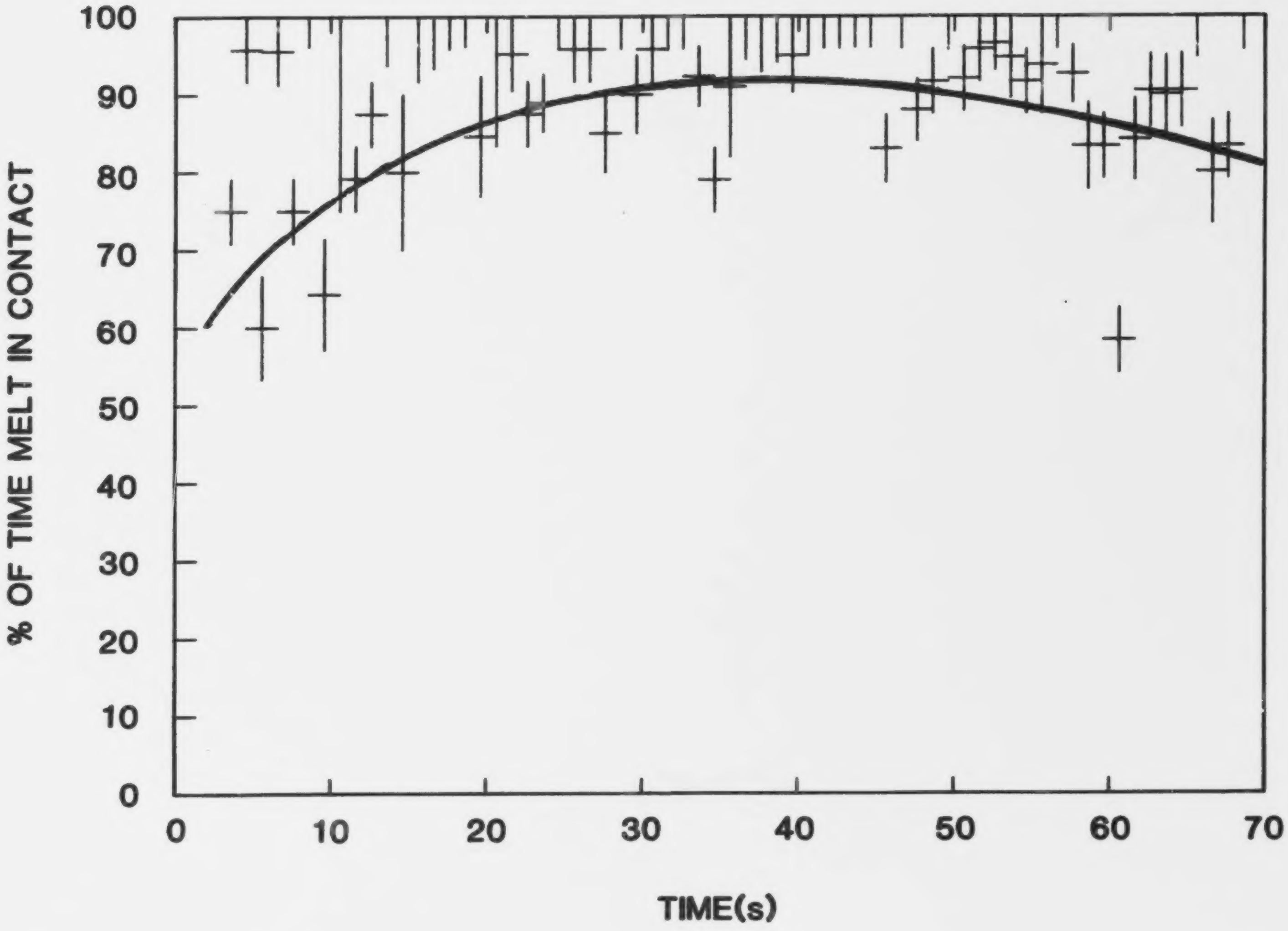

Figure 18 Melt Contact at Location P8

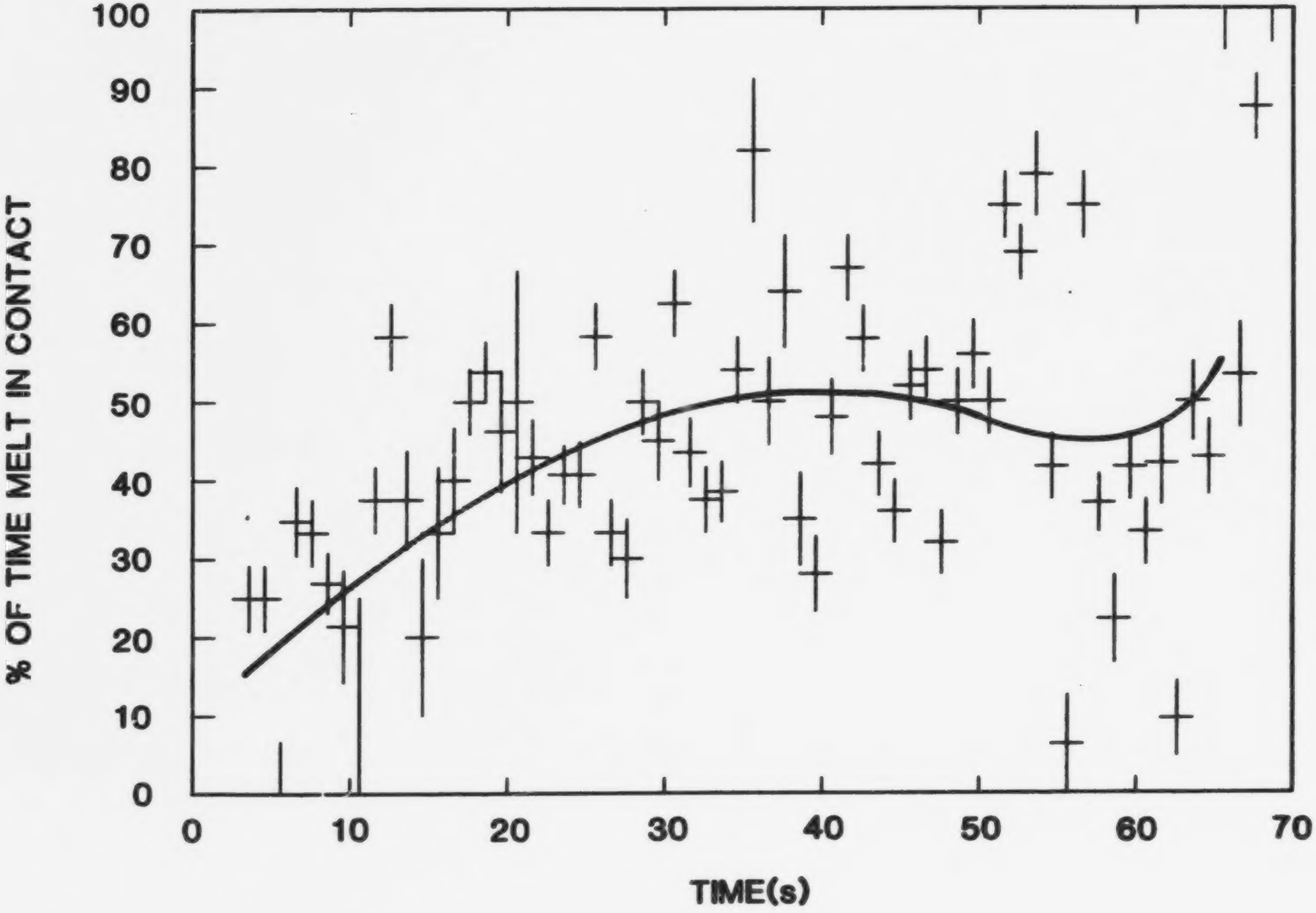

Figure 19 Melt Contact at Location P9

Points P4 and P6 were in contact with the melt only 20 to 30% of the time. The separation of melt at these locations was due to regular bubble formation especially after the interaction had gone for about 30 s.

Melt appeared to be in contact with the concrete at the cavity axis about 70% of the time. Much of the time during which melt was not in contact with concrete at this location was during the violent period (0-30 s) of the test.

As the melt cooled, it became more viscous. Viscosity of liquid iron obeys the Andrade equation.(5,6) At the melting point viscosity is only about 5 centipoises. Investigators know, however, that solid particulate distributed through a liquid causes an apparent increase in the bulk viscosity.(7,8) The increase is approximately linear with volume fraction solids up to about 10 volume percent solids. Apparent viscosity increases more rapidly and non-linearly at higher volume fraction solids. Precipitation of solids was then probably responsible for the very noticeable increase in melt viscosity toward the end of test BURN 1.

About 56 s after the start of the test, viscosity of the melt became high enough that bubbles emerging from the pool made the surface appear foamy. About 63 s after the start of the test, the pool became so viscous that gas bubbles formed at the bottom of the cavity, causing levitation and movement of the entire metal mass. This global disruption of the metal late in the test caused separation of the pool from the concrete at locations other than the site of gas bubble formation.

The metal phase froze abruptly 68 s after ignition of the melt-forming reaction.

The localized sites of gas injection at points on either side of the cavity axis are predicted by the Taylor instability models that give rise to the gas film models of melt-to-concrete heat transfer. The separation of bubble sites predicted by these models is:

$$\lambda = 2\pi\sqrt{3}\,\left(\sigma/g(\rho_\ell - \rho_g)\right)^{1/2}$$

where σ = surface tension of the liquid

g = acceleration of gravity

ρ_ℓ = density of the liquid

$_g$ = density of the gas.

For the conditions of test BURN 1 the predicted bubble separation is 5.3 cm. The observed separation in test BURN 1 is 4 ± 0.7 cm which is in good agreement with calculations in view of the uncertainty of bubble site locations and parameters to use in the predictive equation.

The crucible cavity used in test BURN 1 was quite small. The diameter corresponds to about two characteristic bubble separations according to the gas-film models. The cramped geometry may also have had an effect on the separations between sites of preferred bubble formation on the bottom of the crucible cavity.

The agreement between calculated and observed bubble spacing does not constitute verification that the gas film model of melt-to-concrete heat transfer is appropriate for test BURN 1. The most that can be said is that the test results do not refute the gas film models. Other hypotheses concerning the heat transfer mechanism would also predict the observed bubble spacing.

Posttest inspection of the crucible showed the walls of the cavity to be coated with a light green glass. A ring of this glass adhered to the walls of the crucible about 0.7 cm above the solidified metal. The glass did not completely span the crucible cavity.

Photographs of the top and bottom surfaces of the solidified metal are shown in Figures 20 and 21. The disk-shaped metal weighed 831 g. Differential thermal analysis of the metal suggests it is nearly pure iron. The amount of metal expected based on stoichiometric reaction of the metallothermic charge is 1088 g. Unreacted iron oxides and iron oxides produced by reaction of CO_2 and H_2O from the concrete would account for the rest of the iron. If all the hydrogen and CO measured during the test (see below) were assumed to have been formed by reaction with the metallic pool, the amount of metal formed by the metallothermic reaction would be about 900 g. The metallothermic reaction was then between 76% and 83% complete.

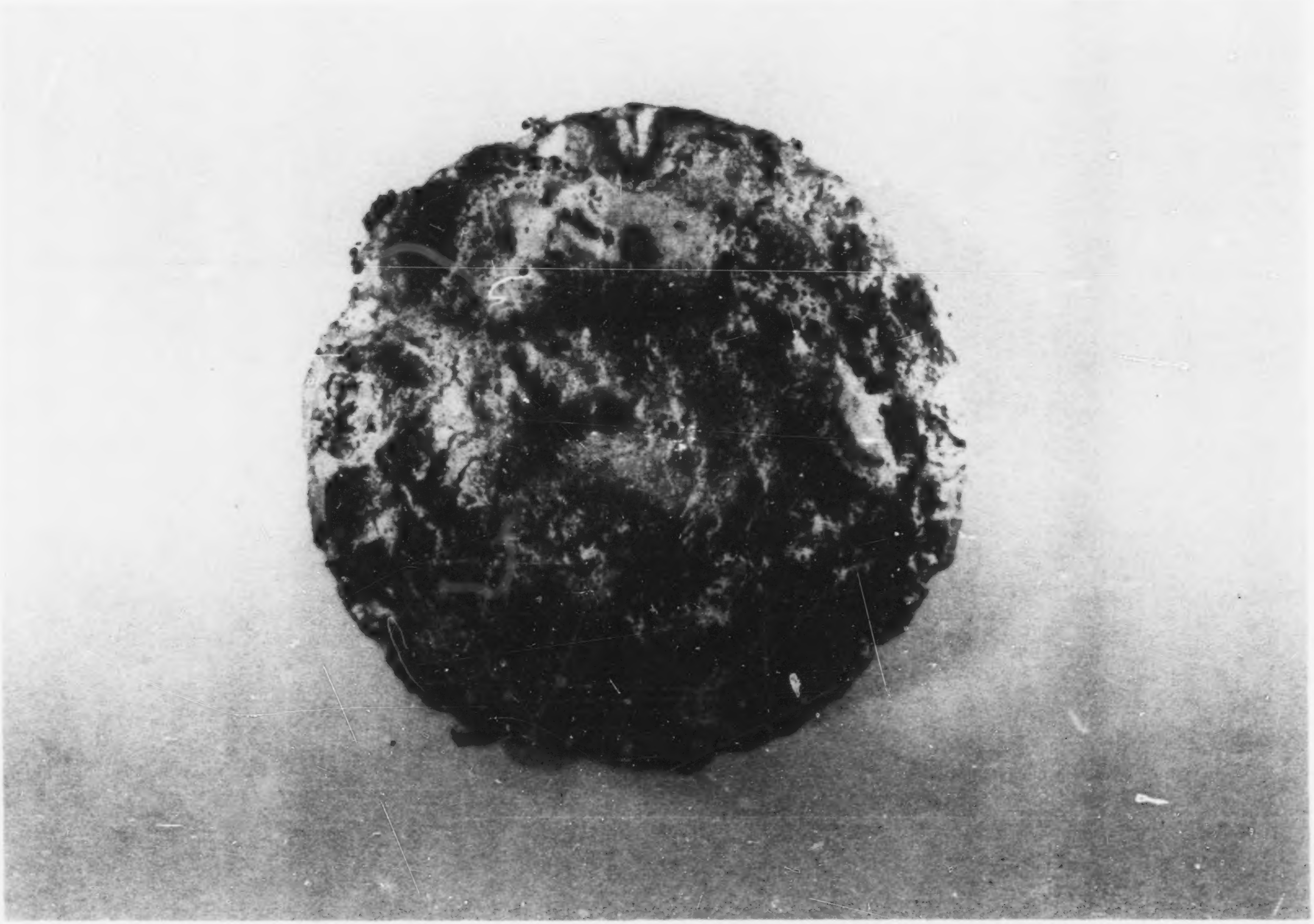

Figure 20   Top Surface of the Solidified Metal Pool
(SAND Photo C78-9402)

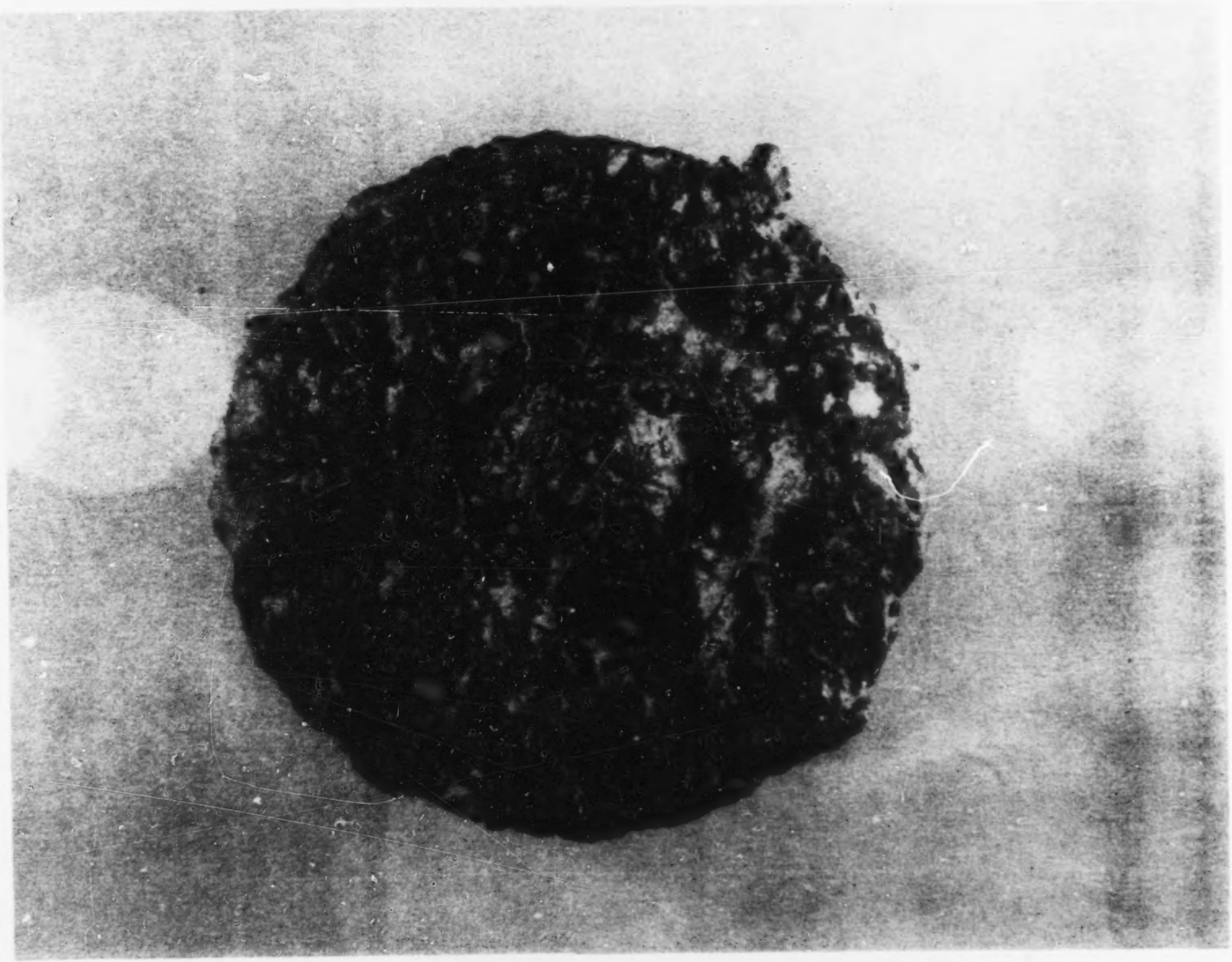

Figure 21 Bottom Surface of the Solidified Metal Pool
(SAND Photo C78-9403)

The top surface of the metal was rough to the touch. Some oxidic slag adhered to the metal. There were no obvious signs of porosity on the top of the metal.

The rapid solidification of the metal phase is reflected by the uniformity of hardness in the metal. Hardness measurements were made at the points indicated in the photograph of a cross-section of the metal slug (Figure 22). The Rockwell A hardness values obtained at these points are also listed in Figure 22. With the exception of two points (Numbers 21 and 30) the hardness values were the same within experimental error. This would indicate that the two-phase mixture of liquid and solid metal was kept well-stirred and homogeneous right up to the time of complete solidification. Certainly the x-ray image gave no indication of the formation of a coherent crust prior to complete solidification of the melt.

The underside of the solidified metal was marked by numerous cavities formed by gas bubbles trapped when the metal froze. The metal about these crevices was smooth to the touch and was coated by a thin adherent layer of metal oxide. The crevices in the metal varied in diameter from 0.2 to 4 cm. The mean diameter of 21 such crevices was 0.86 ± 0.85 cm.

Measuring the bubbles formed during the test was difficult from the recorded melt image. The molten pool was shallow in comparison to the bubble diameter so that a well-formed, isolated bubble was seldom seen. The gas film models would predict bubble sizes of 1.1 to 1.3 cm. These predictions are somewhat smaller than the bubble sizes observed in the x-ray image (~ 2 cm) and somewhat larger than those bubbles found frozen in the metal pool.

The interfacial material immediately below the solidified metal had the appearance observed in previous melt/concrete interaction tests (3). A layer of dark brown, solidified, crystalline slag was present. This layer was 1 to 3 mm thick. The solidified layer adhered tenaciously to a layer of powdery material below. This white powdery material was about 5 mm thick on the bottom of the cavity and about 3 mm thick on the cavity walls adjacent to the frozen metal.

Very little erosion of the concrete occurred during the short test. About 6 mm of concrete had been removed from the cavity walls adjacent to the metal. The erosion pattern at the base of the cavity was not uniform. Maximum erosion occurred in a ring about the cavity axis about

Figure 22 Photograph of a Cross Section of the Metal Slug Showing the Positions of Hardness Determinations

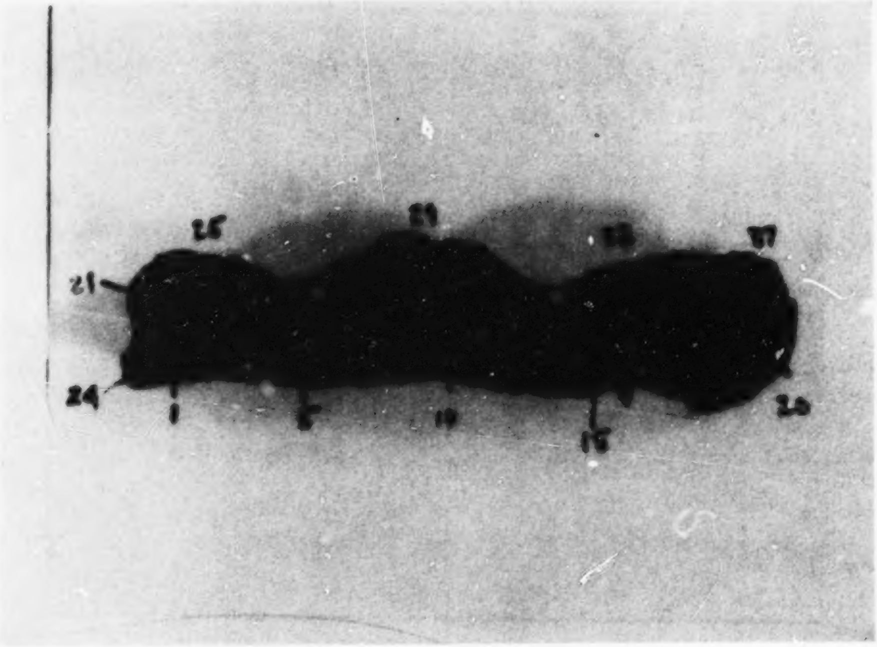

HARDNESS DETERMINATIONS
(Rockwell A 60 Kg Load)

Position	Hardness	Position	Hardness	Position	Hardness
1	46.2	15	48.8	29	49.2
2	49.0	16	49.0	30	35.0
3	44.0	17	49.4	31	48.3
4	46.2	18	49.0	32	49.0
5	47.8	19	48.2	33	47.8
6	47.2	20	50.3	34	50.2
7	48.5	21	52.1	35	49.5
8	47.9	22	49.2	36	49.4
9	48.6	23	49.2	37	49.5
10	47.9	24	48.3	38	49.8
11	49.5	25	48.9	39	49.0
12	48.6	26	49.6	40	49.6
13	47.0	27	48.9		
14	49.1	28	48.6		

5.5 cm in diameter. Erosion depth in this ring was about 9.5 mm. Minimum erosion ($\sim$5 mm) occurred at the center of the ring. Erosion outside the ring was 6-7 mm.

The ring of accentuated erosion on the bottom of the cavity was nearly coincident with the sites of preferred bubble formation observed in the x-ray image. Close inspection showed nothing unusual about the concrete under the ring relative to concrete within and outside the ring.

Analysis of the motion picture record of the test was used to determine the swelling of the pool due to entrained gas. Tracings of the projected image of the molten pool were made at one second intervals. The pool depth was measured at 30 locations on each of these tracings. Mean and maximum depths were calculated. Obviously, tracings of the pool early in the test when the pool was violently levitated and dispersed by vigorous gas evolution were difficult to make. The data for the pool depths are most uncertain for the period of 6 to 12 seconds after the start of the test.

The mean and maximum pool depths were normalized by dividing by the depth expected for a quiescent pool weighing 831 g and having a density of 6.5 g/cm^3. Plots of maximum and mean pool depths with time are shown in Figures 23 and 24. The maximum pool depth varied between 2.8 and 4.3 times the depth of a quiescent pool for the first 20 s of the test. The maximum pool depth varied between about 2 and 2.7 for the next 30 s. The maximum pool depth fell sharply in the last 12 s of the test. The pool depth after solidification was greater than expected for a quiescent pool because of gas bubbles trapped in the metal.

The mean depth of the pool fell over the first forty seconds of the test from about 3.3 to about 1.8 times the quiescent pool depth. The depth of the pool held approximately constant at this level until the metal became so viscous that individual bubbles produced global displacement of the melt. Again, the molten pool was swollen at the conclusion of the test because of the trapped gas bubbles.

The swelling of the pool observed in this test is indeed quite large. The very shallow nature of the pool probably was responsible for the absolute magnitude of the results. Consequently, the results, in absolute value, are not generally applicable. The trends in the variations of level swelling may be more generally useful.

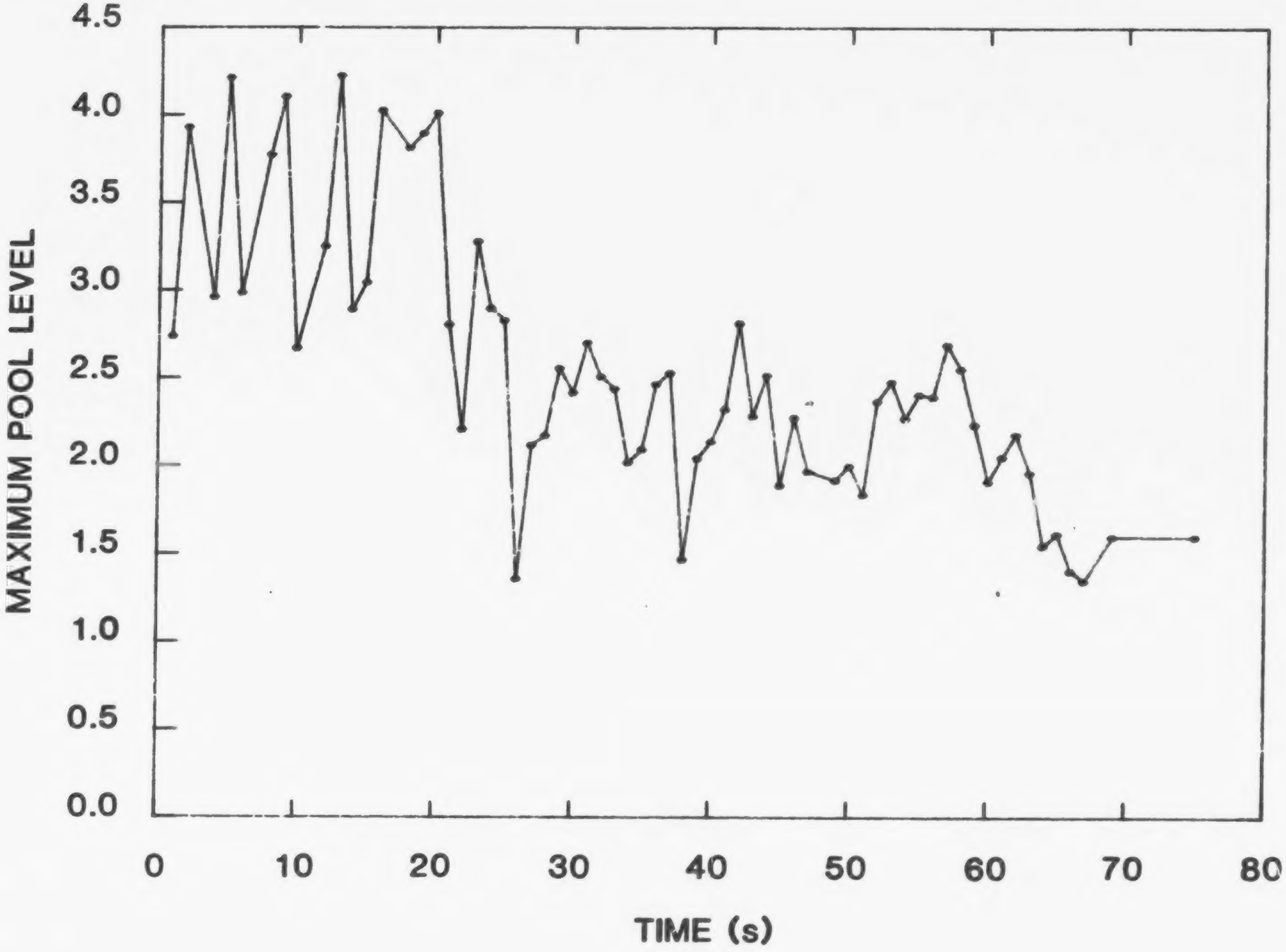

Figure 23 Time Dependence of The Maximum Pool Depth in Test BURN 1. Pool Depth is in Units of Fraction of the Expected Quiescent Pool Depth

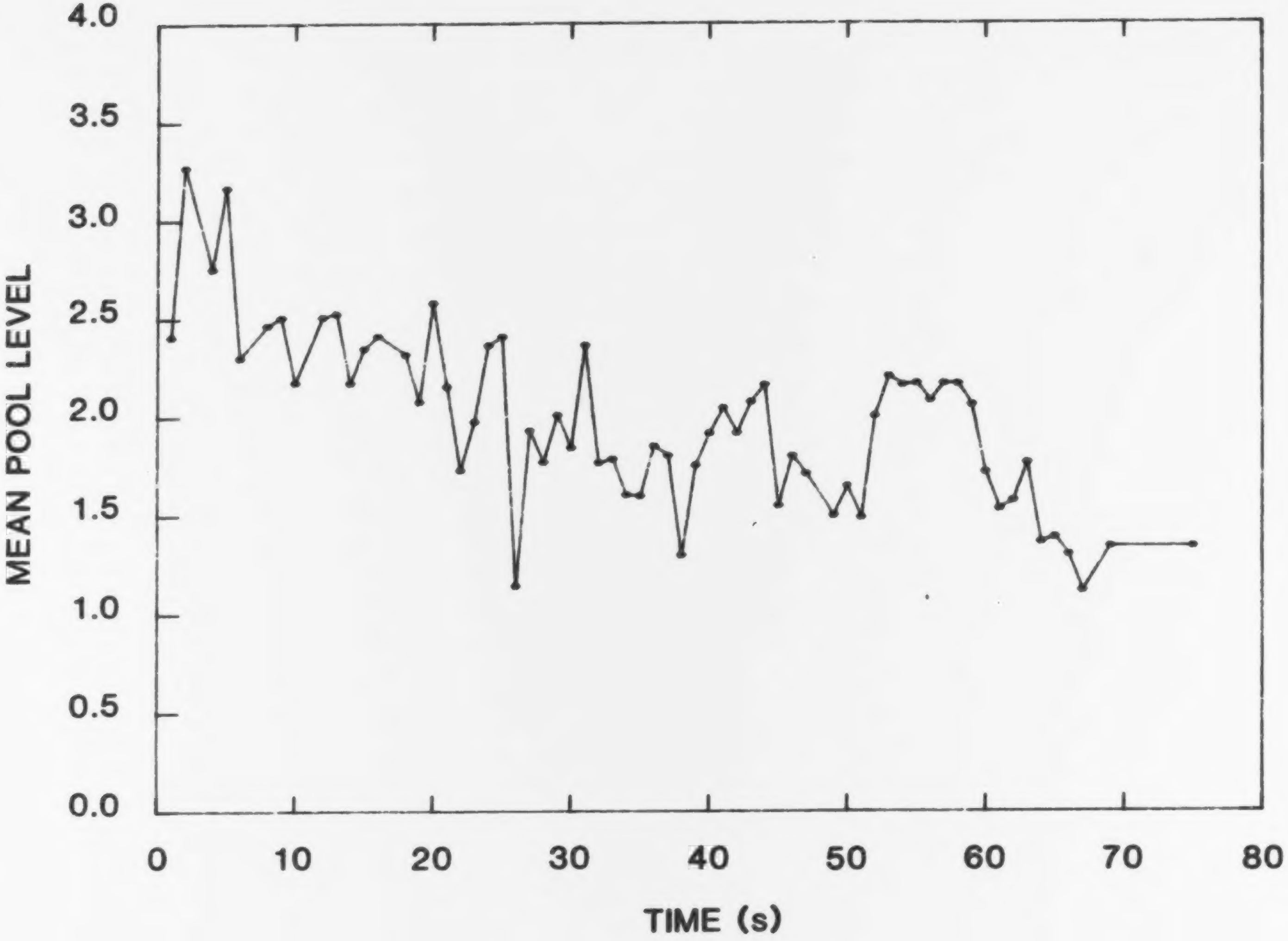

Figure 24 Time Dependence of the Mean Pool Depth in Test BURN 1. Pool Depth is in Units of Fraction of the Expected Quiescent Pool Depth

IV. Quantitative Data

Data on the following topics were collected during test BURN 1:

1) gas composition
2) gas generation
3) concrete temperatures

These data are reported in separate sections below.

A. Gas Composition

The compositions of gas samples drawn from the instrumentation tower and the times of sampling are shown in Table V. The first gas sample (drawn 1.5 s after the start of the test) is air in the instrumentation tower forced through the tower by gas generated within the reaction chamber. The composition of the first gas sample, when compared to the accepted composition of air (9), indicates probable errors in the analytic compositions of:

Nitrogen	± 0.5% of the observed value
Oxygen	± 2.4%
Argon	± 12.8%
Carbon Dioxide	± 6.1%

The rather large error associated with the argon determination arises because of the small amount of argon in the sample and because the argon peak in the chromatogram is close to the large oxygen peak and not distinctly resolved. The error associated with the CO_2 determination is large because there is so little CO_2 in air relative to the amount encountered in gases evolved during the test. This comparison of the composition of the sample drawn at 1.5 s with the composition of air adds credence to the belief that amounts of major constituents of the samples in Table V are accurate to at least ± 10%.

The second and possibly the third gas samples also contain air that was in the instrumentation tower prior to the test. The ratio of N_2:O_2:Ar in the second sample agrees well with that expected for air. The oxygen and

Table V Gas Compositions of Samples Drawn During Test BURN 1

Time* of Gas Sampling (s)	Volume %							
	H_2	N_2	O_2	Ar	CO	CH_4	CO_2	C_2H_4
1.5	0	77.71	21.44	0.814	0	0	0.035	0
6.6	18.51	47.69	12.85	0.507	19.14	0.166	0.858	0.281
10.2	23.81	3.48	0.838	0	61.37	0.179	10.25	0.070
19.8	22.62	1.42	0.338	0	55.110	0.120	20.34	0.056
30.6	23.14	1.26	0.306	0	45.55	0.073	29.60	0.072
39.9	20.28	0.622	0.128	0	34.04	0.066	44.82	0.055
48.15	18.03	0.449	0.088	0	26.81	0.044	54.55	0.028
56.25	19.14	0.638	0.110	0	25.19	0.040	54.88	0.005
63.0	24.05	0.685	0.148	0	31.56	0.037	43.52	0.005
69.0	26.38	0.342	0.005	0	35.21	0.039	38.02	0.005
75.3	29.24	0.677	0.147	0	36.96	0.035	32.95	0.005
92.1	32.70	0.309	0.005	0	38.45	0.032	28.50	0

*Seconds after ignition of the melt-forming reaction nitrogen in gas samples taken 10 s and later may have come from gas trapped in the gas sampling lines.

The presence of oxygen in the samples is clearly inconsistent with the strongly reducing character of other constituents of the gases. The possibility that the observed amounts of CO and H_2 are low because of reaction with oxygen may be evaluated by comparing the observed oxygen to nitrogen ratios with those expected for air. The observed ratios are listed in Table VI. These ratios decrease over the course of the test. Oxygen loss may have occurred because of oxygen reaction with CO, H_2, the hydrocarbons or with hot steel in the instrumentation tower. To assess what error oxygen reaction might have produced in the observed gas chemistry, the maximum possible changes in the CO/CO_2 ratio and the hydrogen content of the gas samples were computed. Results are also shown in Table VI. With the exception of Sample 2, all the changes are well within the analytic uncertainty. Oxygen clearly cannot participate in the chemistry that yields the reduced gas species. Any distortion of this chemistry once air does enter the mixture is small.

The method of chemical analysis of the gas was not well-suited for determination of water content in the gas. Calibration runs using liquid water yielded broad, ill-defined peaks. At low concentrations, the breadth of the peaks would be too great to allow accurate detection. Water was undoubtedly present in the gas. Relative humidity of the ambient atmosphere at the time of the test was about 28%. Liquid water was seen in the sidearm of the instrumentation tower a few minutes after the start of the test.

As gases emerged from the reaction zone, they entered the baffle chamber and were quickly "quenched" by the cool steel. That is, the temperature of the gas fell sufficiently low that reaction kinetics became too slow to allow the gas to remain in equilibrium with its surroundings. If reactions involving all species in the gas stream are assumed to quench at the same time, then equilibrium analysis of the gas is possible. Such analysis can be used to determine the temperature at which the gas was last in equilibrium -- the quench temperature -- and to provide an estimate of the water content in the gas. This procedure has been successfully used to analyze volcanic gases sampled under similarly difficult situations.(10,11)

Table VI Oxygen/Nitrogen Ratios in the Gas Samples

Time Sample Drawn (s)*	O_2/N_2 Ratio	Maximum Possible Change In CO/CO_2 Ratio (in %)	Maximum Possible Change In H_2 Content (in %)
1.5	0.276	-	-
6.6	0.270	252.0	3.33
10.2	0.241	2.9	1.03
19.8	0.238	0.73	0.47
30.6	0.242	0.47	0.37
39.9	0.206	0.45	0.43
48.15	0.196	0.40	0.40
56.25	0.172	0.77	0.69
63.0	0.216	0.45	0.34
69.0	0.015	0.98	0.68
75.3	0.217	0.46	0.27
92.1	0.016	0.99	0.49

*Time in seconds after the ignition of the melt-forming reaction

Predominant reactions in the gas in the neighborhood of the quench temperature are:

(1) $CO + 3H_2 \rightleftharpoons CH_4 + H_2O$

$$\Delta G_1 = -\Delta G_f\ (CO) + \Delta G_f\ (CH_4) + \Delta G_f\ (H_2O)$$

(2) $CO + H_2O \rightleftharpoons CO_2 + H_2$

$$\Delta G_2 = -\Delta G_f\ (CO) - \Delta G_f\ (H_2O) + \Delta G_f\ (CO_2)$$

where ΔG_i = free energy of the i^{th} reaction and $\Delta G_f(j)$ = free energy of formation of the species j.

Solution of the equations:

$$\frac{\Delta G_1}{RT} + \ell n \left[\frac{M_{CH_4}\ M_{H_2O}\ S^2}{M_{CO}\ M_{H_2}^3\ P^2} \right] = 0$$

$$\frac{\Delta G_2}{RT} + \ell n \left[\frac{M_{CO_2}\ M_{H_2}}{M_{CO}\ M_{H_2O}} \right] = 0$$

$$S = \sum_{i=1}^{N} M_i$$

where
R = gas constant
T = absolute temperature (K)
M_i = moles of the i^{th} species in the gas
P = total pressure of the gas (atmospheres)

can be used to obtain T and M_{H_2O}. The temperature found in this way is the quench temperature. The partial pressure of H_2O in the gas is M_{H_2O} P/S.

Results of such an analysis of the gas samples are shown in Table VII. As might be expected, the results are fairly independent of the assumption made concerning the treatment of oxygen and nitrogen except for the sample extracted at 6.6 s. If the diluting effect of oxygen and nitrogen is ignored, (oxygen clearly could not be participating in the reaction chemistry), the quench temperature rises by a few degrees. If oxygen depletion is assumed to have been due to reaction with either CO or H_2 in the gas, this also raises the estimate for the quench temperature -- but only by an insignificant amount.

The estimates of water content in the gas indicate that, except for the sample drawn at 6.6 s, water was a significant constituent of the gas. Once the gas cooled in the instrumentation sidearm, this water would condense so that gas emerging from the sidearm would be saturated with water. This result is consistant with the liquid water found in the sidearm shortly after the test.

The availability of estimates of water content in the gas stream allows comparison of observed hydrogen-carbon ratios with ratios based on the composition of concrete. The observed ratios are shown in Table VII. The H_2/C ratio calculated from the composition of the concrete is 0.561. The observed ratio for the gas sample drawn at 6.6 s is 0.936. The ratio drops sharply to 0.4 at 10.2 s and thereafter increases smoothly. Forty-eight seconds after the start of the test, the ratio exceeds the nominal value expected from the stoichiometry of the concrete. At about 92 s after start of the test, the ratio is 0.899.

The observed variation in the H_2/C ratio in the gases is entirely consistent with the expected heating and decomposition of the concrete. Shortly after melt contacts the concrete, temperatures are reached that are sufficient to dehydrate, but not decarboxylate the concrete. The H_2/C ratio is then quite high in the gas. With further heating decarboxylation occurs and because water in the heated concrete has been depleted, the H_2/C ratio falls to a low value. However, as the melt cools, greater volumes of concrete are dehydrated than are decarboxylated so the H_2/C ratio rises and eventually exceeds the stoichiometric ratio.

Table VII Estimated Quench Temperature and Gas Compositions

Time of Gas Sampling (s)	Volume%									T Quench (K)	H_2/C Molar Ratio
	H_2	N_2	O_2	Ar	CO	CH_4	CO_2	C_2H_4	H_2O		
6.6	18.34	47.25	12.74	0.50	18.97	0.165	0.850	0.279	0.904	1104	0.936
10.2	22.78	3.33	0.80	0	58.73	0.171	9.81	0.067	4.307	1112	0.400
19.8	20.83	1.31	0.311	0	50.75	0.111	18.73	0.052	7.91	1084	0.417
30.6	20.16	1.10	0.266	0	39.68	0.064	25.78	0.063	12.89	1072	0.507
39.9	16.63	0.51	0.105	0	27.91	0.054	36.75	0.045	17.99	1024	0.537
48.15	14.11	0.352	0.069	0	20.99	0.034	42.72	0.022	21.70	1003	0.563
56.25	14.54	0.485	0.084	0	19.14	0.030	41.71	0.004	24.00	1004	0.634
63	18.51	0.527	0.114	0	24.28	0.028	33.49	0.004	23.05	1048	0.720
69	20.66	0.268	0.004	0	27.56	0.031	29.78	0.004	21.68	1068	0.739
75.3	22.95	0.531	0.115	0	29.01	0.027	25.86	0.004	21.50	1090	0.811
92.1	25.66	0.242	0.004	0	30.17	0.025	22.36	0	21.53	1112	0.899

An especially pleasing outcome of the analysis was the consistency of the quench temperature estimates obtained for the gas samples - 1066 ± 40 K. Deviations from the mean of the estimates for the various samples is insignificant in comparison to the estimated accuracy of the composition data.

The consistant quench temperature observed for the gas samples makes it possible to attempt to determine what controls the observed gas composition. It is likely that oxygen fugacity in the system is controlled by the oxidation of iron in the neighborhood of the quench temperature. To check this likelihood, the observed ratios of carbon monoxide and carbon dioxide may be compared to those predicted for the following equilibria:

$$(1) \quad 0.947\ \mathrm{Fe}\ (s) + \mathrm{CO_2} \qquad \mathrm{Fe_{0.947}O}(s) + \mathrm{CO}\ (g)$$

$$G_1 = G_f\ (\mathrm{Fe_{0.947}O}) - G_f\ (\mathrm{CO_2}) + G_f\ (\mathrm{CO})$$

$$(2) \quad 3\mathrm{Fe}(s) + 4\mathrm{CO_2}(g) \qquad \mathrm{Fe_3O_4}(s) + 4\mathrm{CO}\ (g)$$

$$G_2 = G_f\ (\mathrm{Fe_3O_4}) - 4\ G_f\ (\mathrm{CO_2}) + 4\ G_f\ (\mathrm{CO})$$

This comparison is made in Figure 25. Data from the JANAF tables were used to compute the predicted ratios.(12) Error bounds corresponding to 1 kcal uncertainty in the free-energy of reaction are included in plots of the predicted CO/CO_2 ratios for the above two reactions.

The observed CO/CO_2 ratios do not fit either predictions well. The observed ratios come closest to predictions for the $Fe/Fe_{0.947}O$ equilibria. The observed data might fit this reaction well if the activity of iron in steel were taken into account. The evidence for the equilibrium of iron and $Fe_{0.947}O$ as the controlling mechanism for the composition of evolved gases is not overwhelming.

B. Gas Generation Rates

For the test fixture used in test BURN 1, the rate of gas flow through the sidearm of the instrumentation tower is indicative of the rate of gas generation at the

FIGURE COMPARISON OF OBSERVED CO/CO2 RATIOS TO THOSE PREDICTED FOR TWO IRON OXIDATION REACTIONS

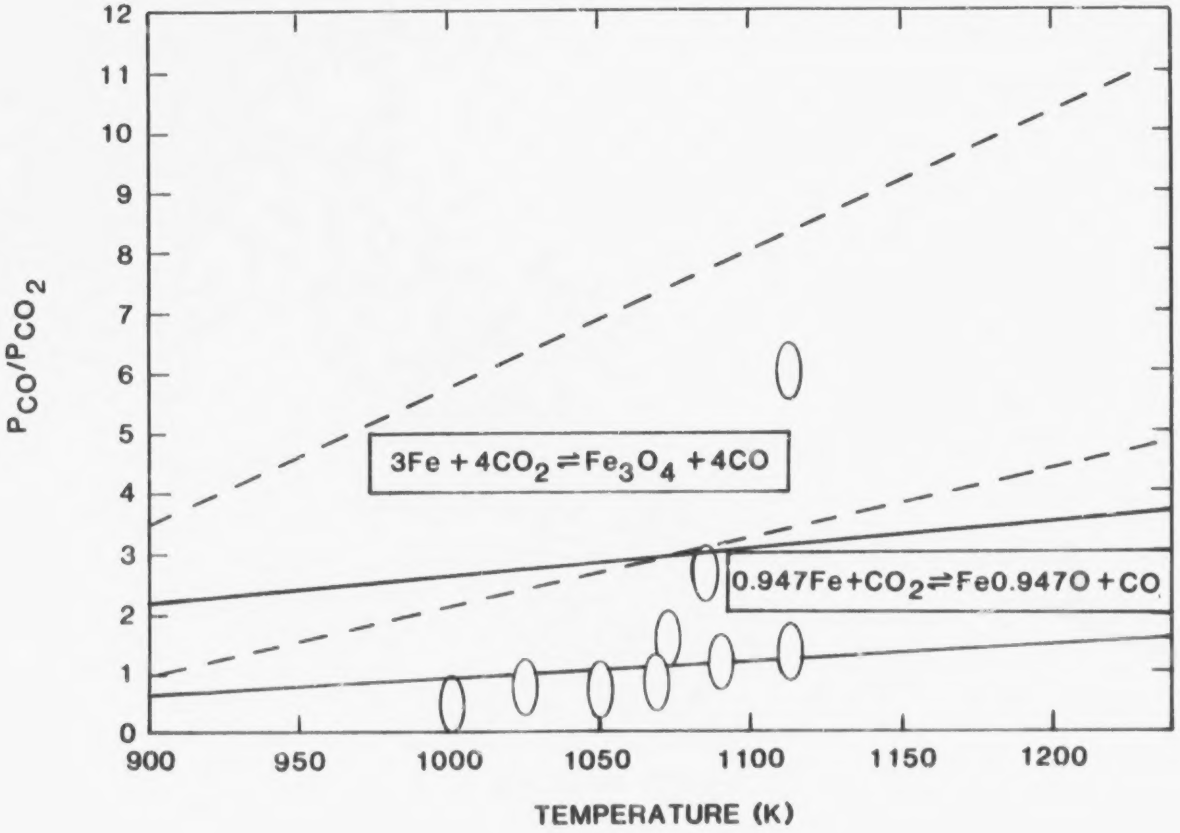

Figure 25 Comparison of Observed CO/CO$_2$ Ratios to Those Predicted for Two Iron Oxidation Reactions

site of melt interactions with concrete. The pressure drop across the laminar flow element in the sidearm is dependent on the gas viscosity which, in turn, is weakly dependent on gas composition. The discussions above indicate that gases in the instrumentation sidearm were saturated with water after about 5 secs. of the test. Compositions listed in Table V were corrected to include water and the resulting compositions used to estimate the viscosity of the gas mixtures by the Herning-Zipperer equation (see Appendix B). Gas samples drawn at times less than 6 s after ignition of the metallothermic charge were assumed to have a relative humidity of 28%. Gas compositions were linearly interpolated to obtain compositions at times not coincident with gas sampling.

The gas flow data are shown in Figures 26 and 27. The gas flow data are consistent with the observed melt behavior during the test. There was a brief pulse of gas at ignition. Steady, but low gas flow took place for about 2.5 seconds. There was another pulse of gas when melt contacted the bottom of the crucible. At about 5 seconds, the gas flow rose sharply to a peak of 209 liters-STP/min. Other peaks of nearly equal magnitude in the gas flow rate occurred at 5.9, 8.5 and 10 seconds after ignition. These eruptions of gas correspond to eruptions of the melt observed in the x-ray image data. The gas flow rate began to decline after about 10 s. At the time the melt froze, the flow rate was about 12 l-STP/min. At 5 minutes following ignition, the flow rate had fallen to only 1.5 l-STP/min.

The investigators suspect that the gas generation rate in the concrete cavity after the melt froze was substantially higher than the rate of gas flow through the laminar flow device. Steam generated in the concrete cavity would condense during passage through the instrumentation tower and would not contribute to the observed flow rate.

The gas flow data were numerically integrated to obtain the cumulative gas production which is shown as a function of time in Figure 28. Similar integrated flow data for H_2, CO, and CO_2 are shown in Figure 29. The total volume of gas and the volumes of the various constituents of the gas evolved during the first five minutes of the test were:

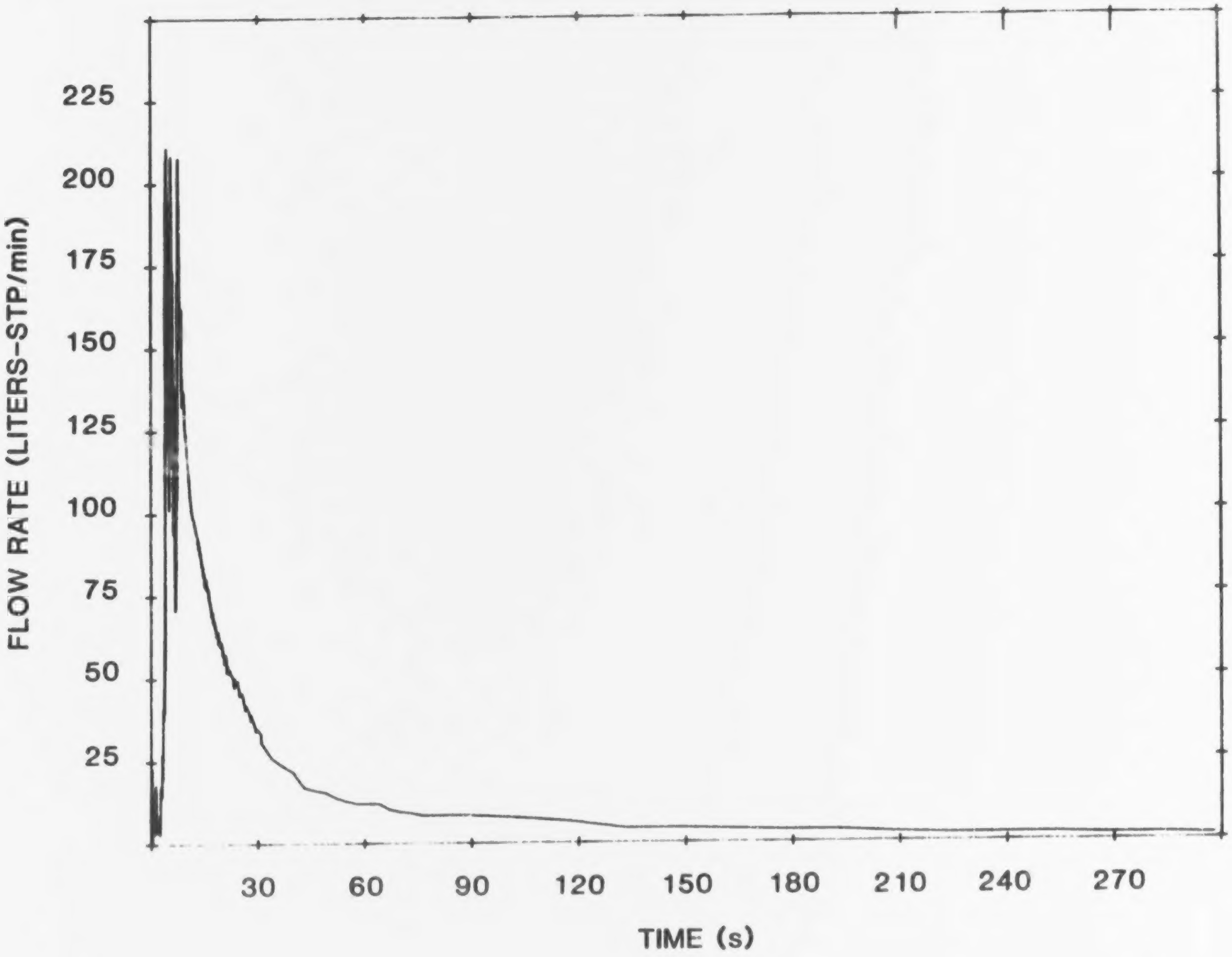

Figure 26 Gas Flow Rate Test BURN 1

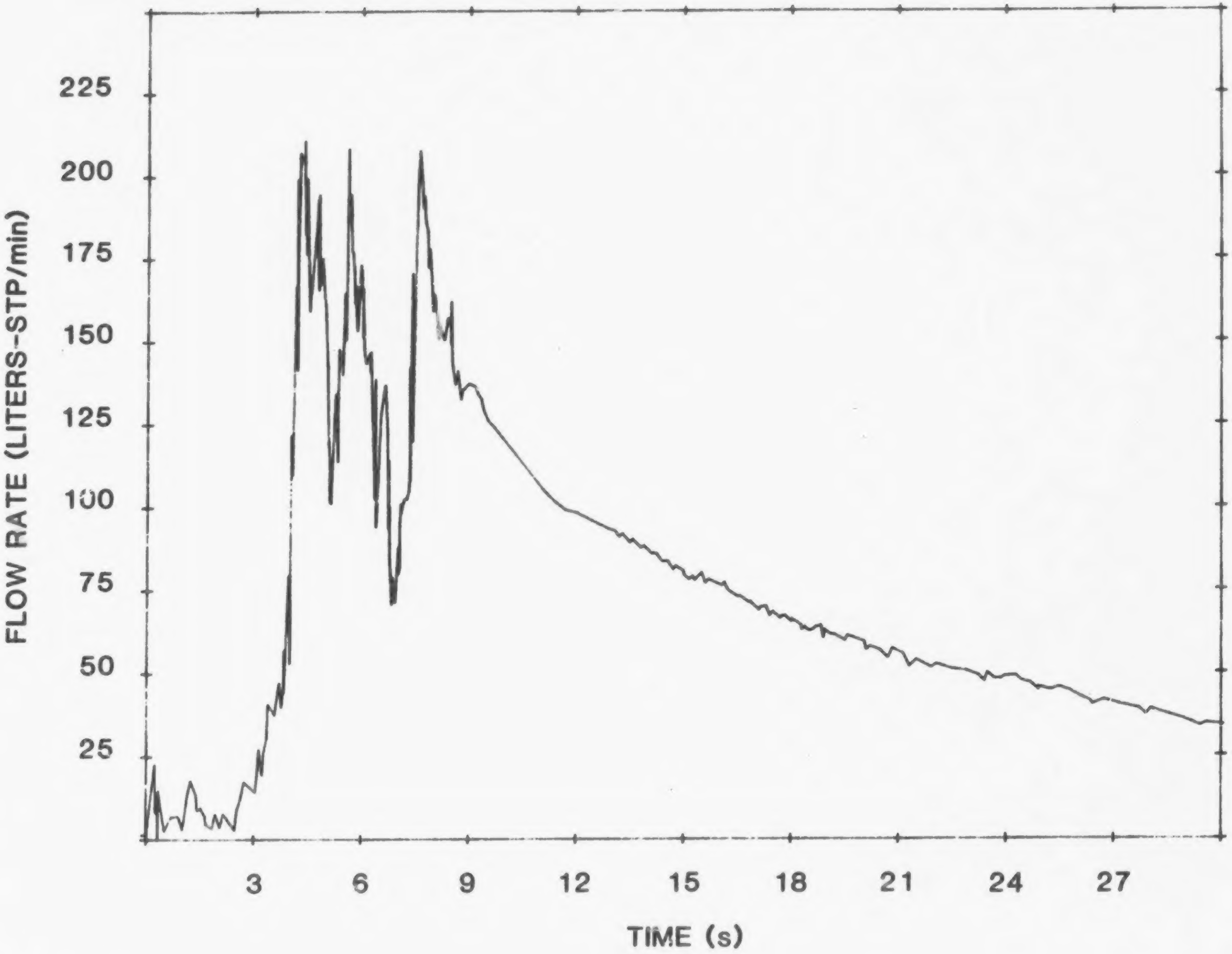

Figure 27 Gas Flow Rate in the First 30 Seconds of Test BURN 1

BEST DOCUMENT AVAILABLE

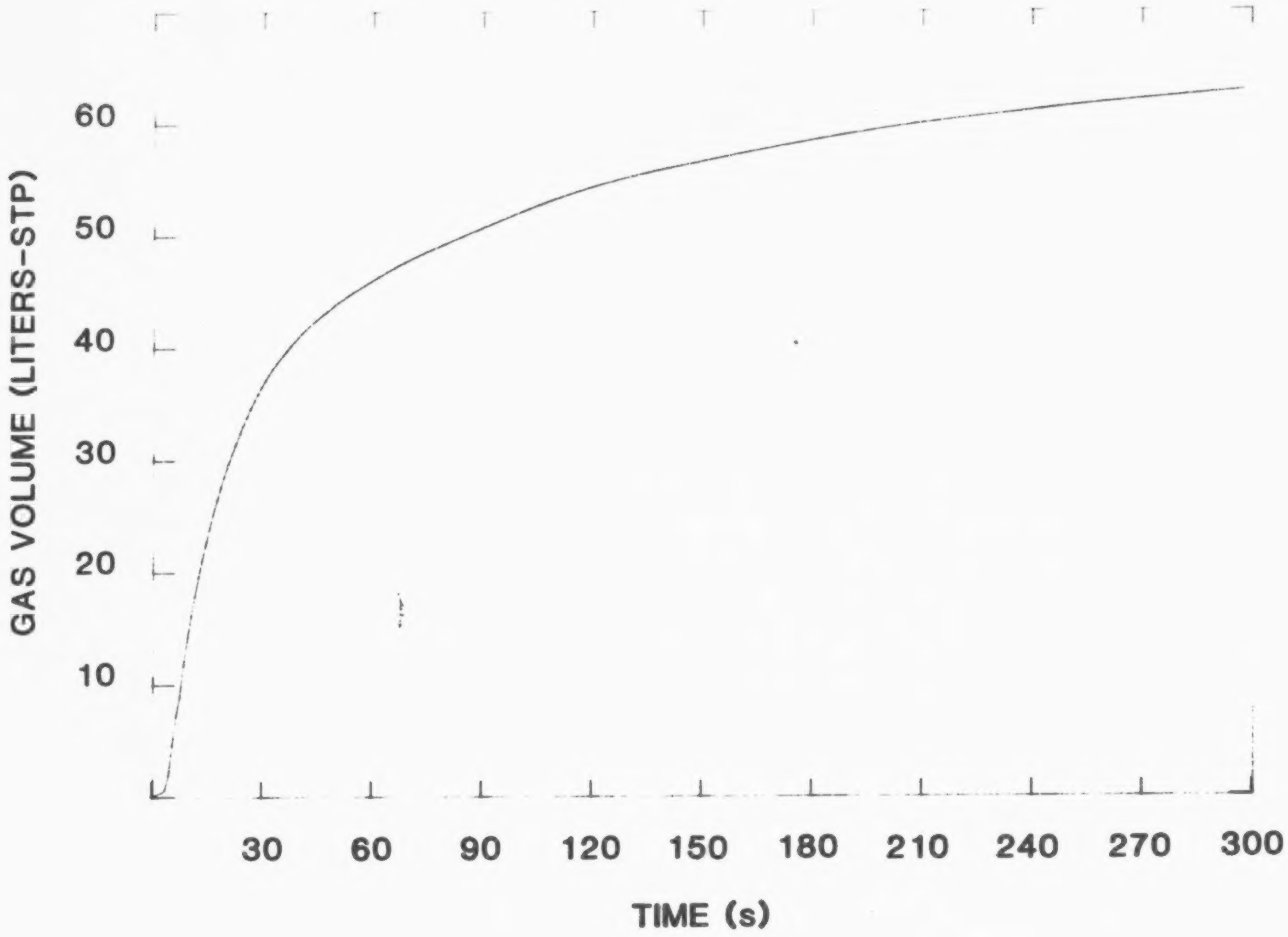

Figure 28 Cumulative Gas Production During Test BURN 1

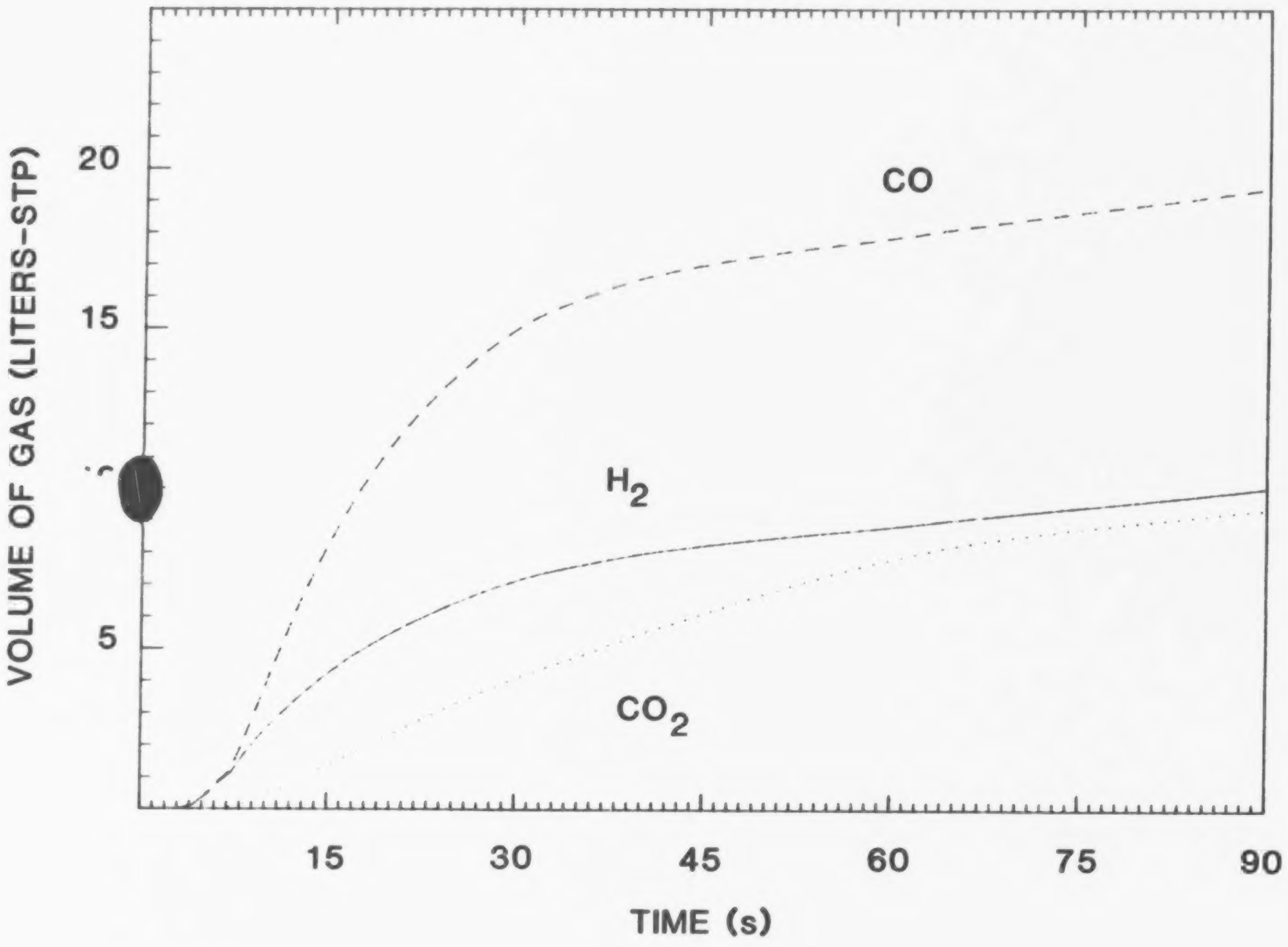

Figure 29 Cumulative Production of H_2, CO, and CO_2 During Test BURN 1

GAS	TOTAL VOLUME (Liters-STP)
all gas	62.78
H_2	13.53
N_2	6.96
O_2	1.86
Ar	0.07
CO	23.50
CH_4	0.06
CO_2	12.44
C_2H_4	0.04
H_2O	2.71

The value of water volume generated does not reflect the water condensed within the instrumentation tower. When this water is included, based on the estimation described above, the volume of water vapor released is about 11 liters-STP.

Oxygen and nitrogen in the gas samples were attributed to air in the instrumentation tower and residual gas in the sample bottles or sampling lines. The internal volume of the instrumentation tower ahead of the laminar flow element is estimated to be about 8.1 liters. This would contain 6.7 liters-STP of air prior to the test. This is about 25% less than the integrated flow of air constituents. If nitrogen and oxygen in the gas samples 10 s and later after ignition are assumed to be due to residual air in the gas sampling lines, the discrepency is reduced to less than 10%. In view of the linear interpolation of the variation in gas composition, this is quite good agreement.

The integrated volume of carbonaceous species evolved during the test is indicative of the decarboxylation of 337 g of concrete. This would correspond to a layer 0.78 cm thick surrounding the volume occupied by the solidified melt. This is in good agreement with the posttest observations.

The integrated flow of hydrogen-containing species corresponds to the dehydration of only 414 g of concrete. Posttest inspection of the crucible and the thermocouple data all suggest that the concrete to at least a distance of 2.7 cm from the cavity boundaries or about 1250 grams of concrete was dehydrated. The total flow of hydrogen-containing species is not indicative of the amount of concrete dehydrated in the test. Hydrogen-containing species released later than five minutes after the start of the test are not included. Water vapor that condensed during its passage from the cavity to the flow measuring device was not detected.

The maximum and mean pool depths as fractions of the quiescent pool depth are plotted against the superficial gas velocity in Figures 30 and 31. The superficial gas velocity was computed using the gas flow rate at standard temperature and pressure (25°C and 1.0 atms) and assuming flow through an opening 8.9 cm in diameter. Because of the high temperatures in the pool, the actual superficial gas velocities must have been much higher.

Both maximum and mean pool depths showed a sharp increase toward an asymptotic limit with superficial gas velocity. The depth data were fit by nonlinear least squares methods to the equations:

$$\text{Mean depth} = 1 + (1.549)\exp(-2.774/V_s)$$

$$\text{Maximum depth} = 1 + (2.645)\exp(-3.353/V_s)$$

where V_s = superficial gas velocity (cm/sec STP).

Again, the absolute magnitudes of these correlations probably have little significance beyond this particular test. The asymptotic dependence of pool depth on gas velocity may be a more general result.

C. Temperature Data

Temperature data from thermocouple TC5 located below the cavity bottom are shown in Figures 32 and 33. Temperature data from thermocouple TC4, located on the external wall of the crucible are shown in Figures 34 and 35. Both thermocouples indicate an arrest in the temperature rise between 90°C and 100°C. This temperature rise has been attributed to the endothermic process of vaporizing the so-called evaporable water from the concrete. The downward velocity of the 90°C isotherm is estimated to be 0.020 cm/s. The radial velocity of the isotherm is 0.018 cm/s. This approximate uniformity in temperatures in the radial and axial directions is reflected in all the temperature data up to 300 seconds after the start of the

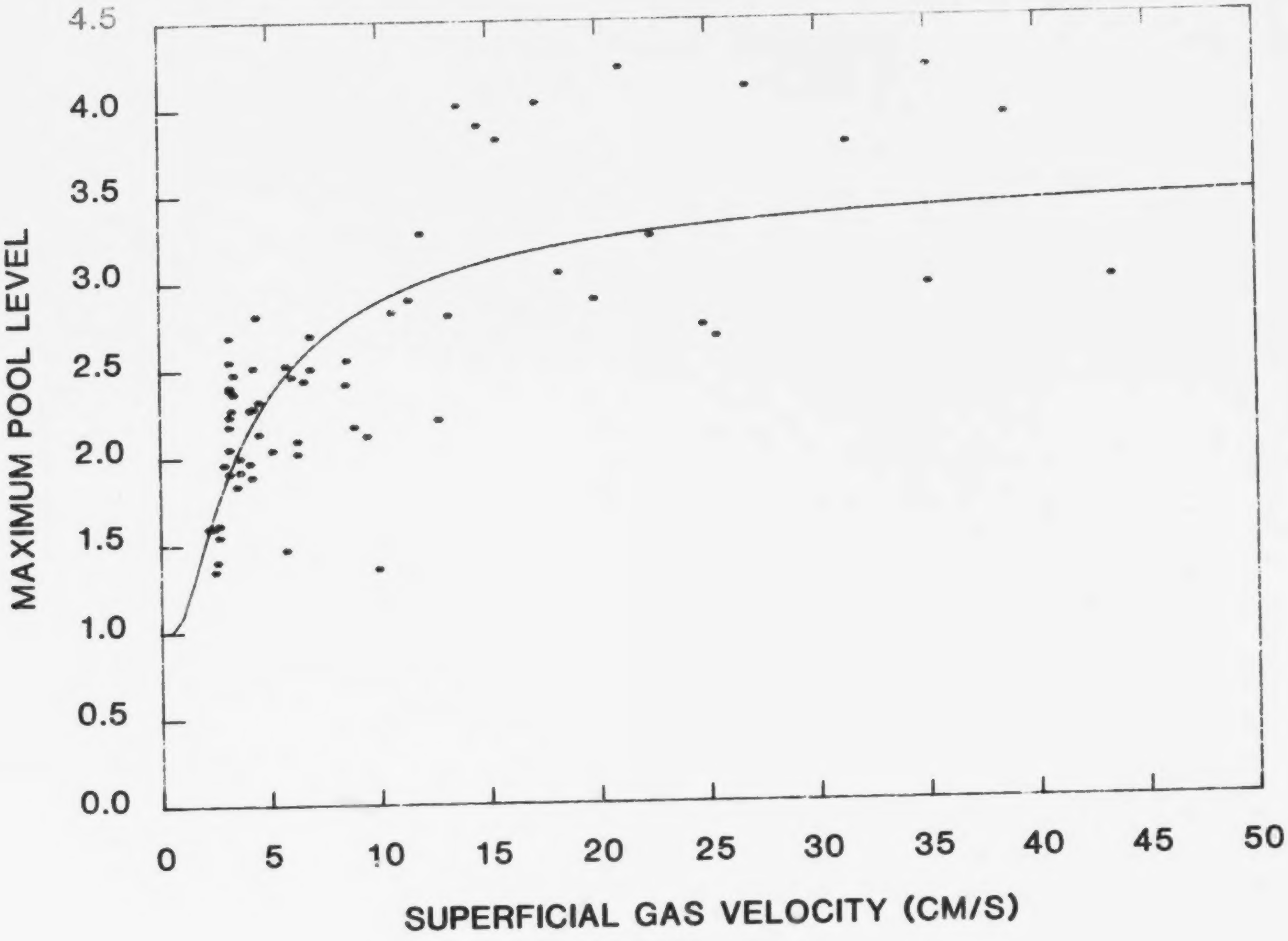

Figure 30 Maximum Pool Depth as a Function of Superficial Gas Velocity (STP). Pool Depth Is in Units of Fraction of the Expected Quiescent Pool Depth

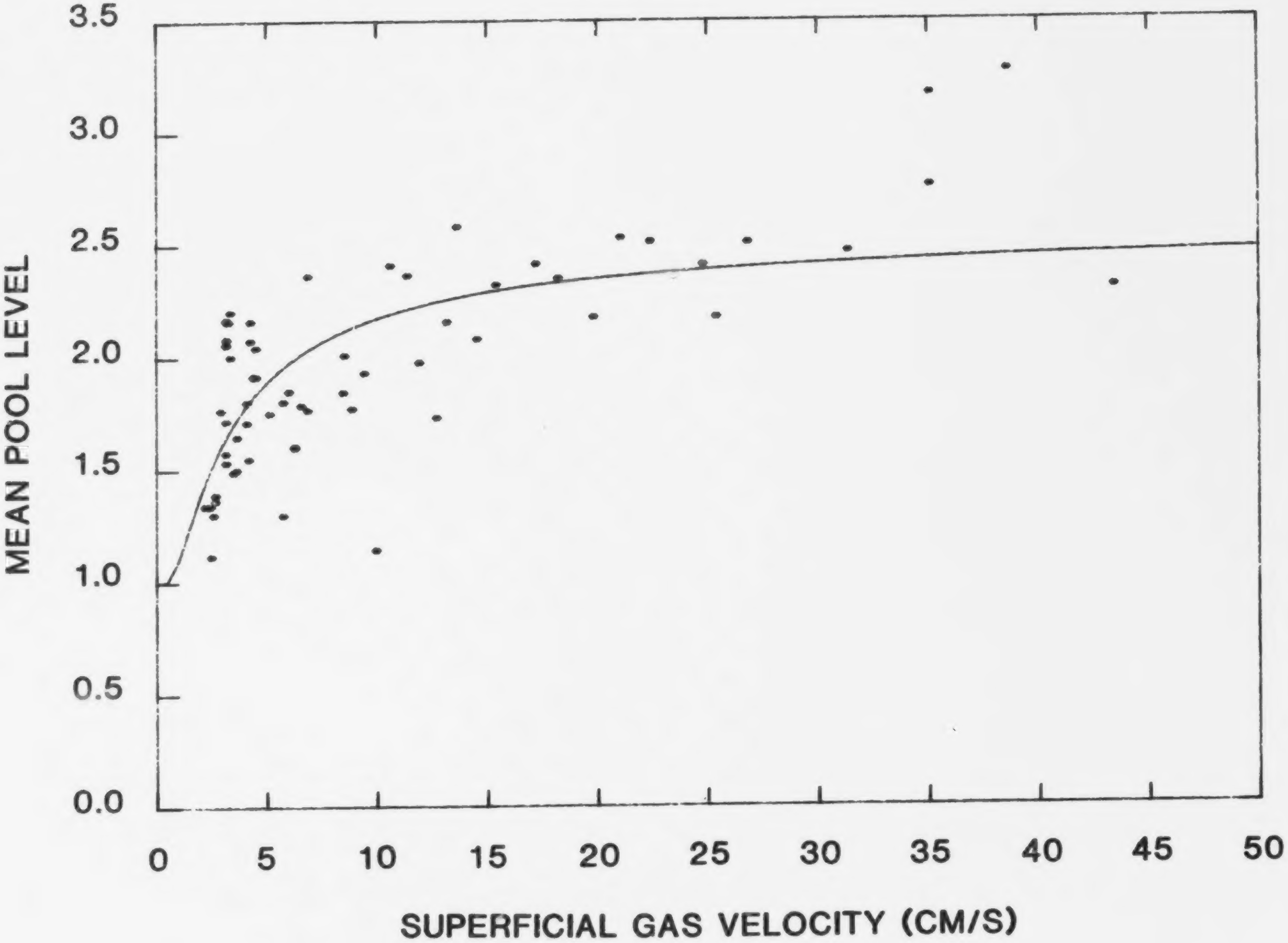

Figure 31 Mean Pool Depth as a Function of Superficial Gas Velocity (STP). Pool Depth Is in Units of Fraction of the Expected Quiescent Pool Depth

BEST DOCUMENT AVAILABLE

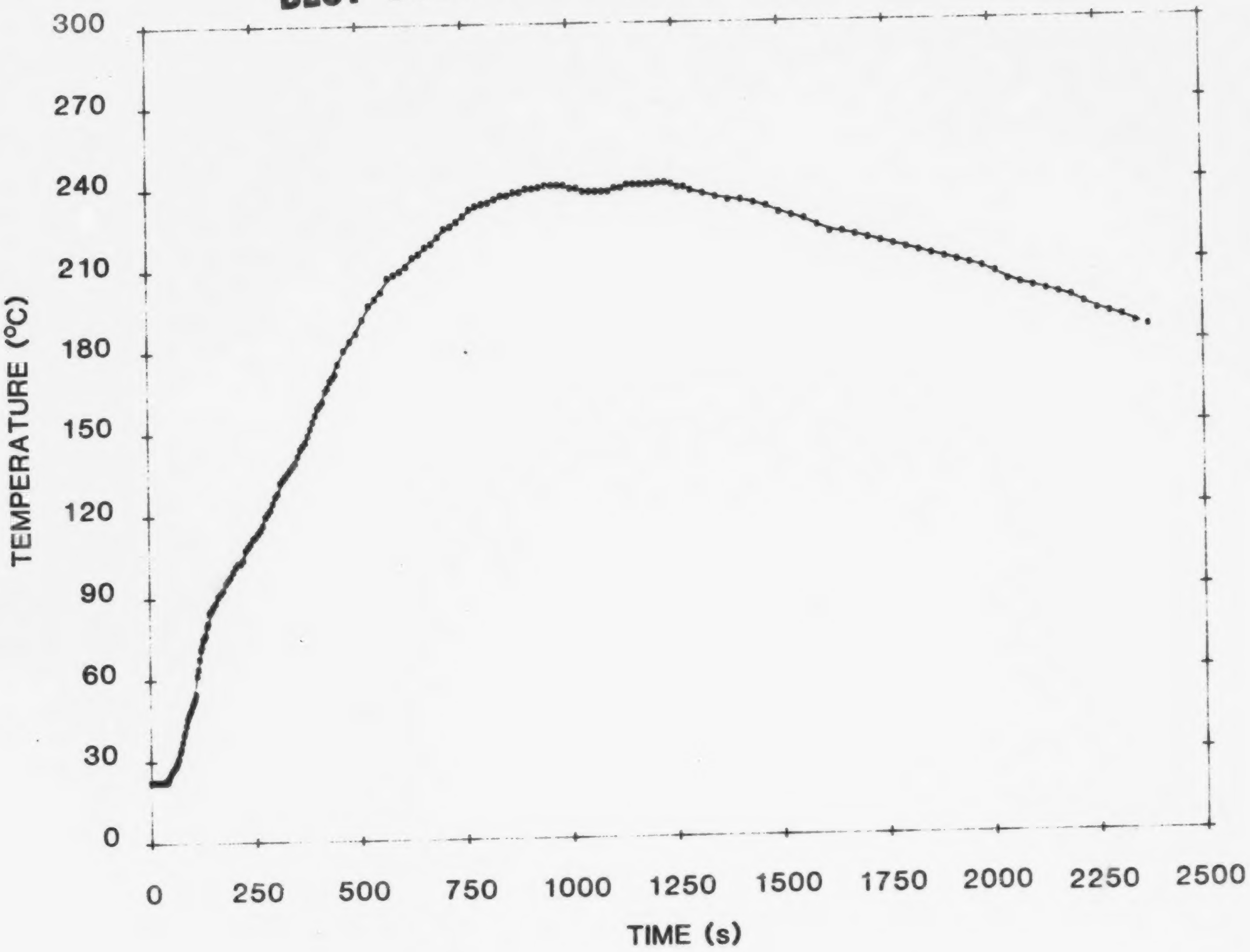

Figure 32 Temperature Data from Thermocouple TC5
Below the Bottom of the Crucible Cavity

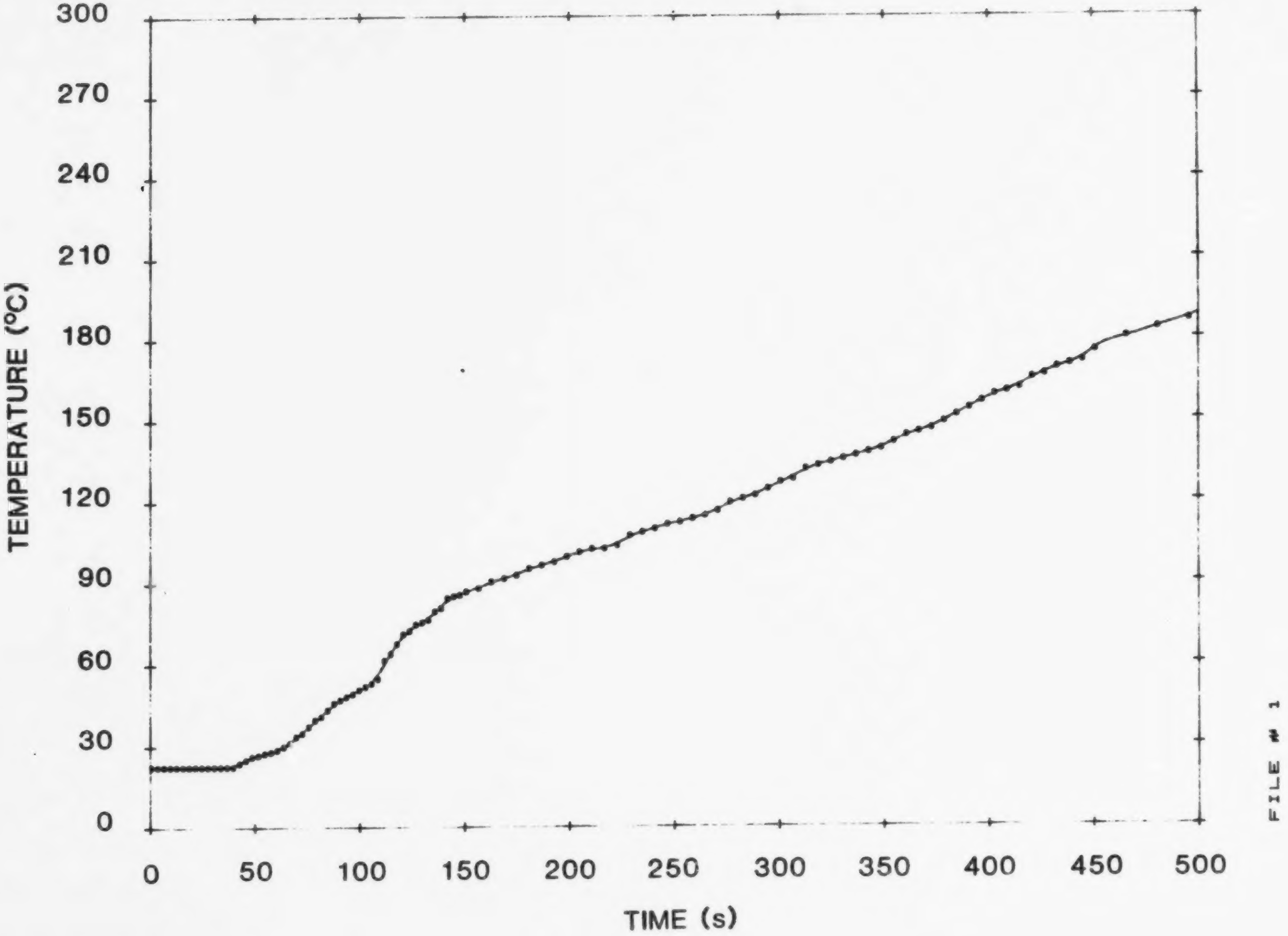

Figure 33 Temperature Data from Thermocouple TC5 for the First 500 s of Test BURN 1

BEST DOCUMENT AVAILABLE

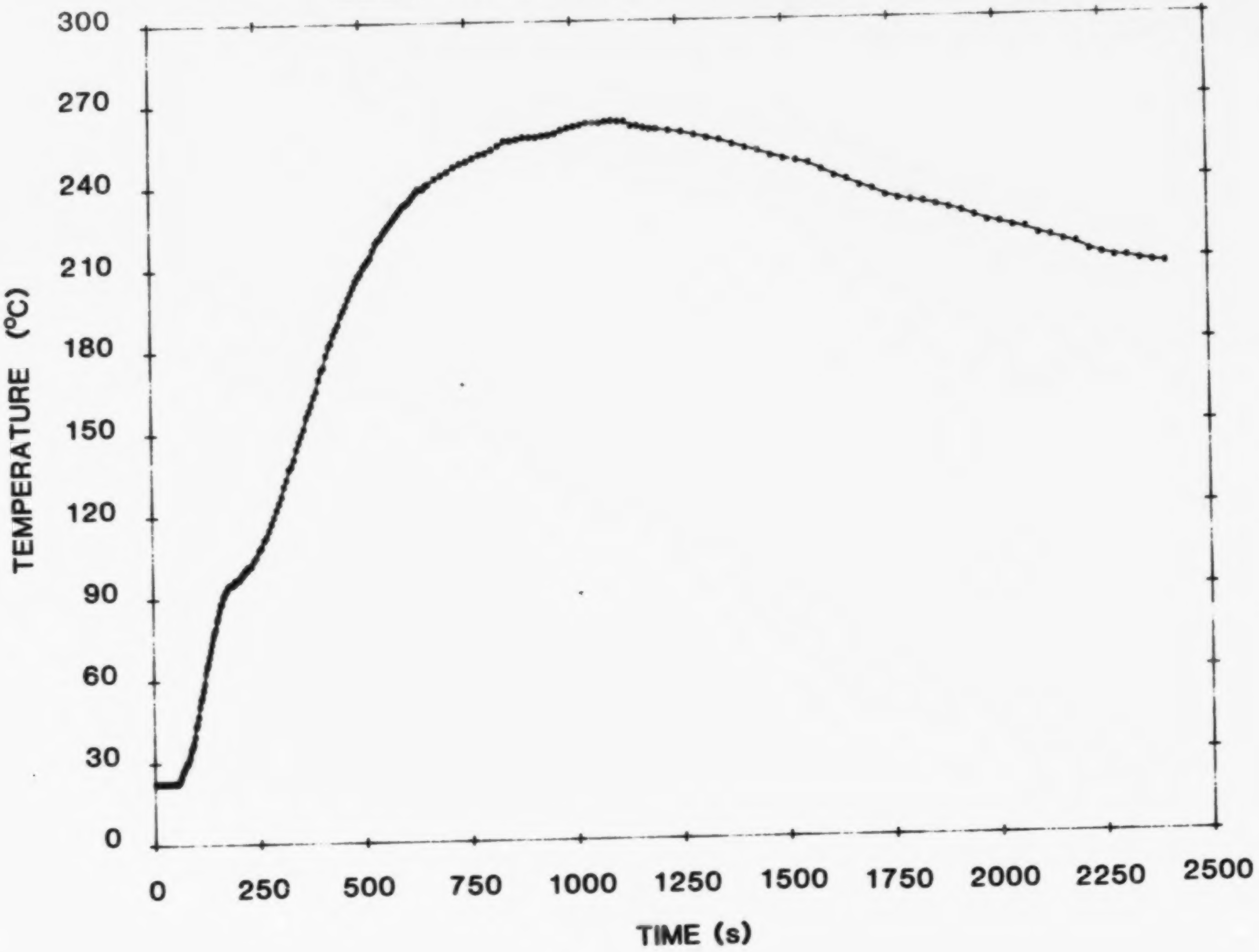

Figure 34 Temperature Data from Thermocouple TC4 on the External Wall of the Crucible

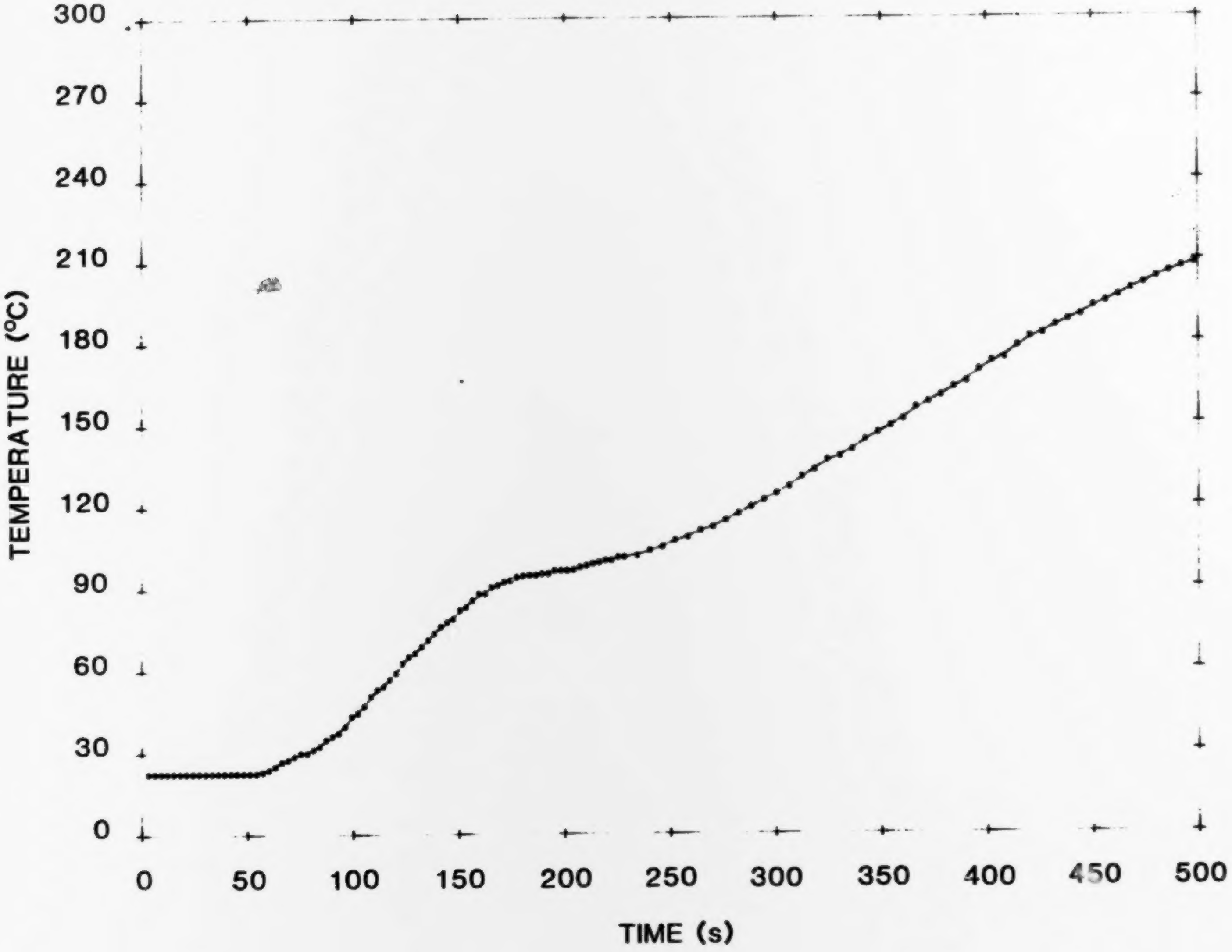

Figure 35 Temperature Data from Thermocouple TC4 for the First 500 s of Test BURN 1

test. At later times, the base thermocouple indicated higher temperatures than the wall thermocouple. This may reflect both the higher downward erosion and convective cooling of the crucible walls.

Temperature data from the wall thermocouple shows a brief, unexplained, arrest at about 50°C. Otherwise, neither of the temperature curves shows a behavior that might be correlated with melt behavior.

V. Summary

The feasibility of using x-ray image intensification as a method for directly observing melt behavior during high-temperature melt interaction with concrete has been demonstrated. The technique allows the mode of melt contact with the concrete to be quantitatively monitored. The extent of melt swelling due to entrained gas can be measured. Gas bubbles formed at the interface between the melt and the concrete can be seen escaping into the melt. Both freezing of the melt, and the formation of crusts can be precisely determined using the image intensification method.

The technique will probably not be adequate for detecting a continuous gas film between the melt and concrete as predicted by some models of the melt-to-concrete heat transfer. The image intensification method does allow verification of other predictions of these models such as the spacing and size of gas bubbles at the melt/concrete interface.

In test BURN 1, the swelling of the melt due to entrained gas ( ) could be correlated with the superficial gas velocity (V_s) by an expression of the form:

$$= A \exp(-b/V_s)$$

where A and b are constants.

Gas injection into the melt became localized after an initial period of intense gas generation. The spacing of the sites of localized gs generation were similar to the spacing predicted by the "gas film" model.

The melt used in test BURN 1 did not contain large amounts of oxide. What oxidic melt existed formed a crust that did not remain in contact with the pool. The metallic phase did not form a crust.

The compositions of gases evolved during test BURN 1 indicate the gases were quenched at temperatures between 1000 and 1120 K. If reaction of the gas with steel structures above the melt was not significant, the gas composition data suggests that CO_2 and H_2O liberated from the concrete are reduced to thermochemical equilibrium as the gases passed through the melt.

Acknowledgement

This work was supported by the U.S. Nuclear Regulatory Commission. The authors tha[illegible] Egar, F. A. Hasenkamp, and D. Ballard for their assistance in obtaining the x-ray images of the melt.

VI. References

(1) USAEC, An Assessment of Accident Risks in U.S. Commercial Nuclear Power Plants, WASH-1400 (August 1974).

(2) D. A. Powers, D. A. Dahlgren, J. F. Muir, and W. B. Murfin, Exploratory Study of Molten Core Material/Concrete Interactions July 1975 - March 1977, SAND77-2042 (Albuquerque, NM: Sandia Laboratories, February 1978).

(3) D. A. Powers and F. E. Arellano, Large Scale, Transient, Tests of the Interaction of Molten Steel With Concrete, (Albuquerque, NM: Sandia National Laboratories, in press).

(4) D. P. Mouser, P. C. Ruggles, and N. A. Stark, The Television Soc. J., 11, 261 (1967).

(5) G. Cavalier, Proc. Natn. Phys. Lab., 2 4D (1958).

(6) E. N. da C. Andrade, Phil. Mag., 17, 497, 698 (1934).

(7) M. Kunitz, J. Gen. Physiol., 9 715 (1926).

(8) A. P. Ting and R. H. Luebbers, AICHE Journal, 3 111 (1957).

(9) R. C. Weast, editor-in-chief, Handbook of Chemistry and Physics, 45th edition, (Cleveland, OH: Chemical Rubber Co., 1964).

(10) T. M. Gerlach, J. Volcan. Geoth. Research, 7 295 (1980).

(11) B. E. Nordlie, Am. J. Sci., 271 417 (1971).

(12) D. R. Stull and H. Prophet, JANAF Thermochemical Tables, 2nd edition NSRDS - NBS37, U.S. Department of Commerce, National Bureau of Standards, June 1971.

BLANK PAGE

Appendix A

Temperatures in Thermitic Melts

The classic Thermite reaction is:

$$8Al + 3Fe_3O_4 \rightarrow 9Fe + 4Al_2O_3 + \text{heat.}$$

Because this is a heterogeneous reaction and achieves very high temperatures, it does not go to completion. The completeness of the reaction depends on details of the conditions of the reaction such as the mass, geometry and containment of the reactants. The extent of reaction is limited because some of the iron oxide is stabilized as $FeAl_2O_4$ (hercynite) or aluminum is dissolved in the product iron as Fe_3Al. A more realistic description of the thermite reaction is:

$$8Al + 3Fe_3O_4 \rightleftharpoons (27\xi - 18)Fe + 9(1 - \xi)\,FeO + (12\xi - 8)Al_2O_3 + 6(1 - \xi)Fe_3Al$$

where ξ is the extent of reaction $(0 < \xi < 1)$.

The limit on temperature achieved in the reaction mixture is usually provided by vaporization of one of the reaction products. For the idealized reaction, vaporization of iron would limit the reaction temperature. When the reaction is incomplete, vaporization of other species could provide the limit. The phase transitions of the reaction products are described in Table A-I.

The maximum temperature during a thermite reaction as a function of the extent of reaction is plotted in Figure A-1. These temperature data were computed using the thermochemical cycle

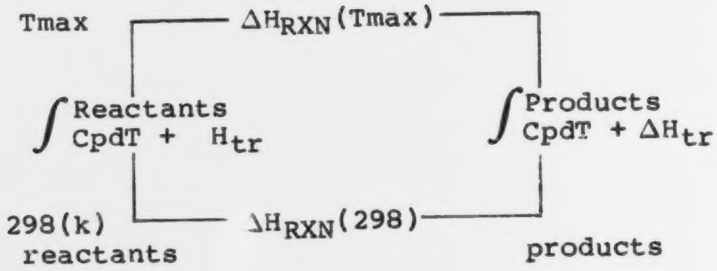

Table A-1 Phase Changes in Thermite Reaction Products

Species	Type of Phase Change	Temperature of Phase Change (K)	Heat of Phase Change (cal/mol)
Fe	melting	1809	3630
Fe	boiling	3145	83679
FeO	melting	1650	5750
FeO	decomposes	3687	
Al_2O_3	melting	2315	28300
Al	melting	933	2560
Al	boiling	2767	69497

where

T_{max} = maximum temperature

$\Delta H_{RXN}(T)$ = heat liberated by reaction at temperature T

C_p = heat capacity

ΔH_{tr} = heat of phase changes

Data for the calculations were from the JANAF Tables (1). In making these calculations the thermite reaction was simplified to

$$8Al + 3Fe_3O_4 \rightarrow 9\xi Fe + 9(1 - \xi)FeO + (1 + 3\xi)Al_2O_3 + 6(1 - \xi)Al.$$

Neglecting heat produced by formation of hercynite or intermetallics is probably not serious.

No heat losses were considered in the calculation of data depicted by the solid line in Figure A-1. For reactions that proceed to less than 85% completion the maximum temperature is controlled by the behavior of excess aluminum in the products. When the reaction goes further toward completion sufficient energy is liberated to vaporize the excess aluminum. The extent of the reaction must be in excess of 94% for the boiling of iron to control the temperature.

The thermite reaction is so fast that heat losses do not greatly alter the conclusions from the adiabatic calculation. The dashed line in Figure A-1 was calculated assuming that blackbody radiant heat was lost for 2.3 s from the top surface of a reaction mixture configured as that in test BURN 1. The results are shifted to only slightly higher (< 2%) reaction extents than those calculated assuming adiabatic conditions. These differences are of the same order as errors induced in the adiabatic calculations by uncertainties in the thermochemical data.

Actual measurements of the temperature of metallothermic reaction fronts is most difficult. Meyer(2) has used an optical pyrometer technique to determine the temperature of the classic thermite reaction to be 2983 K. Wartenberg and Wehner(3) reported a value of 2673 ± 50 K also based on pyrometry. Bogolyubov(4) used a heavily shielded and

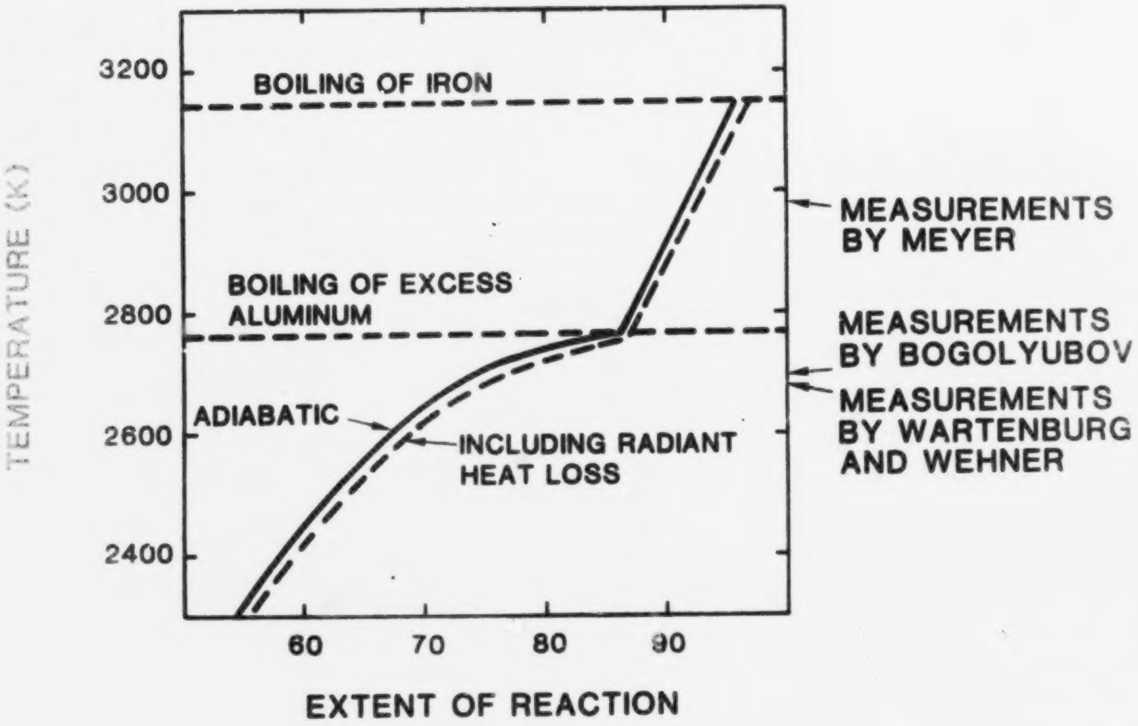

Figure A-1 Maximum Temperature of A Thermitic Melt preheated tungsten-molybdenum thermocouple to obtain a value of 2693 K. He did not, however, correct for thermal inertia of his sensor except to preheat to 1000°C, so this value must be a lower bound on the actual temperature. (Bugolyubov's theoretical calculations of thermite temperatures are based on room temperature thermal properties which leads to low estimates of the adiabatic reaction temperature).

The above measurements of the thermite reaction temperatures are compared with the calculated temperatures in Figure A-1. None of the authors reported details on the extents of the reactions they studied. If investigators recognize that all measurements must be lower bounds on the true temperature, the measurements and calculations agree well. An estimated initial temperature for the melt in test BURN 1 of 2700 K would be in accord with both the calculations and the measurements.

References

(1) D. R. Stull and H. Prophet, JANAF Thermochemical Tables, 2nd edition, NSRDS-NBS 37, U.S. Department of Commerce National Bureau of Standards, June 1971.

(2) Meyer, Die Temperatur des Eisenthermit Reaction, Dissertation, Munich, 1932 as quoted in Reference 4.

(3) H. V. Wartenberg and G. Wehner, Z. Elektrochem. 42, 293 (1936).

(4) V. A. Bogulyubov, Stad 17, 531 (1957).

Appendix B

Viscosity of Mixtures

Formulae available for predicting the viscosities of gaseous mixtures are summarized below:

(1) Herning-Zipperer(1)

$$\mu_m = \sum_{i=1}^{N} X_i \ \mu_i \ M_i^{1/2} \Big/ \sum_{i=1}^{N} X_i M_i^{1/2}$$

(2) Wilke(2)

$$\mu_m = \sum_{i=1}^{N} \mu_i \ / \ (1 + 1/X_i \sum_{\substack{j=1 \\ j\neq i}}^{N} X_j \ \psi_{ij})$$

$$\psi_{ij} = [1 + (\mu_i/\mu_j)^{1/2} \ (M_j M_i)^{1/4}]^2/2.828 \ (1+ M_i/M_j)^{1/2}$$

(3) Buddenberg - Wilke(3,4)

$$\mu_m = \sum_{i=1}^{N} \mu_i/ [\ 1 + \frac{1.385\,\mu_i}{X_i \rho_i} \sum_{\substack{j=1 \\ j\neq i}}^{N} X_j/D_{ij}]$$

$$D_{ij} = \frac{0.0606T^{1.78}}{P(V_i^{1/3} + V_j^{1/3})} \ \frac{(1 + \sqrt{M_i+M_j})}{\sqrt{M_i \ M_j}}$$

where μ_m = viscosity of the gas mixture

X_i = mole fraction of the i^{th} species in the gas mixture

μ_i = viscosity of the pure i_{th} species when pure

M_i = gram molecular weight of the i^{th} species

ρ_i = density of the i^{th} species when pure

P = pressure of the gas mixture

V_i = molecular volume of the i^{th} species when pure

T = absolute temperature of the gas mixture

N = number of species of the gas mixture

The Herning-Zipperer equation was used to calculate the viscosity of air. The comparison of the calculated and observed viscosities over the temperature range of 0-240°C is shown in Table B-I. The standard deviation between the calculated and observed viscosities is about 0.6%. The errors are serially correlated and increase from about 0.1% at 0°C to about 0.8% at 240°C. These errors are, however, completely inconsequential to the uses made of the Herning-Zipperer equation for reducing data for the laminar flow element as described in the text.

Table B-I Comparison of Calculated and Observed Viscosities of Air

Temperature (°C)	Viscosity (Micropoises) Observed*	Viscosity (Micropoises) Calculated** (Herning-Zipperer Eqn.)
20	182.5	182.3
40	190.6	190.2
60	198.8	198.2
80	206.9	206.1
100	215.0	214.0
120	223.1	222.1
140	231.2	230.0
160	239.4	237.9
180	247.5	245.8
200	255.6	253.8
220	263.7	261.7
240	271.9	269.7

*Obtained by linear interpolation of experimental data over the temperature range of 0-410°C in Reference 5.

**Calculation based on the linearly interpolated data over the temperature range of 0-410°C in Reference 5. The composition of air was taken to be 78.084% N_2, 20.946% O_2, 0.033% CO_2, and 0.934% Ar.

References

(1) F. Herning and L. Zipperer, Gas Wasserfach., 79, 49-54, 69-73 (1936).

(2) C. R. Wilke, J. Chem. Phys., 18, 517 (1950).

(3) J. W. Buddenberg and C. R. Wilke, Ind. Eng. Chem., 41, 1345 (1949).

(4) L. Andrussow, Z. Elektrochem., 54, 567 (1950).

(5) R. C. Weast, editor-in-chief, Handbook of Chemistry and Physics, 55th edition (Cleveland, OH: The Chemical Rubber Co., 1974).

Appendix C

Photographs of the Melt Image

Photographs taken from the motion picture copy of the video-tape record of the test are collected in this appendix. Times in the captions of the photographs are in seconds after ignition of the melt-forming reaction.

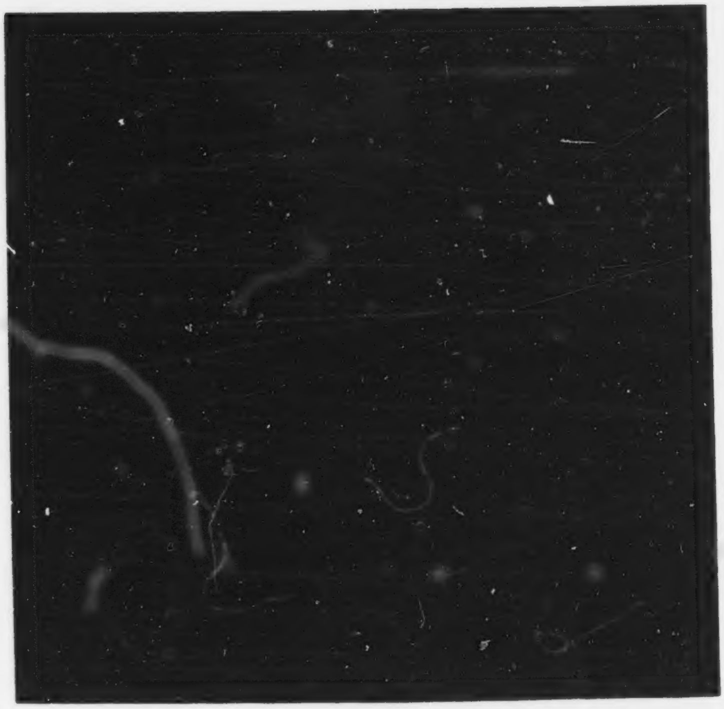

Pretest x-ray of test structure. The cavity outline and the nipple from the base plate can be faintly seen.

t = -1.0 s

Video image of test fixture. The cavity cannot be distinguished. The bright horizontal bar slightly above the middle of the figure is produced by the "beat" frequency between the x-ray pulsing and video scanning.

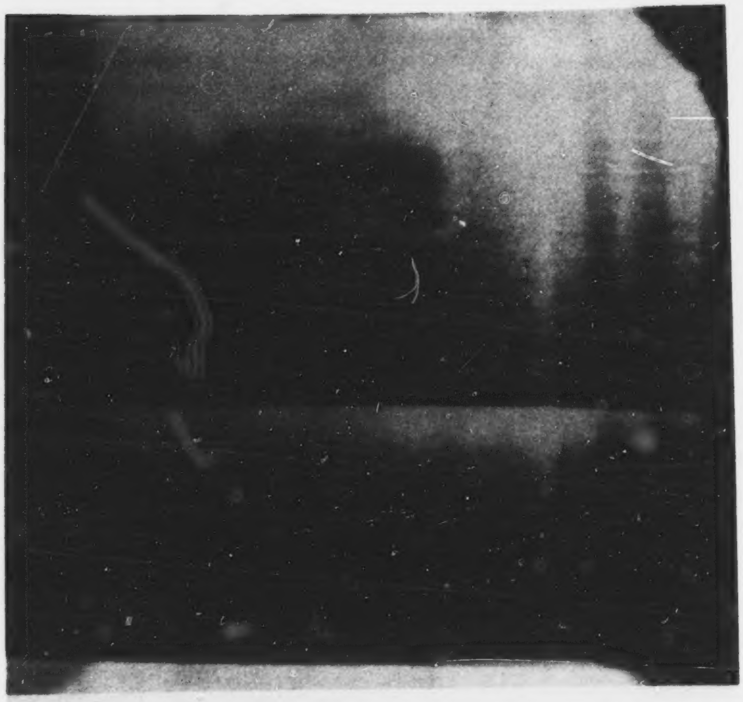

t = 3.08 s

Bubble diameters are about 1.9 and 2.2 cm.

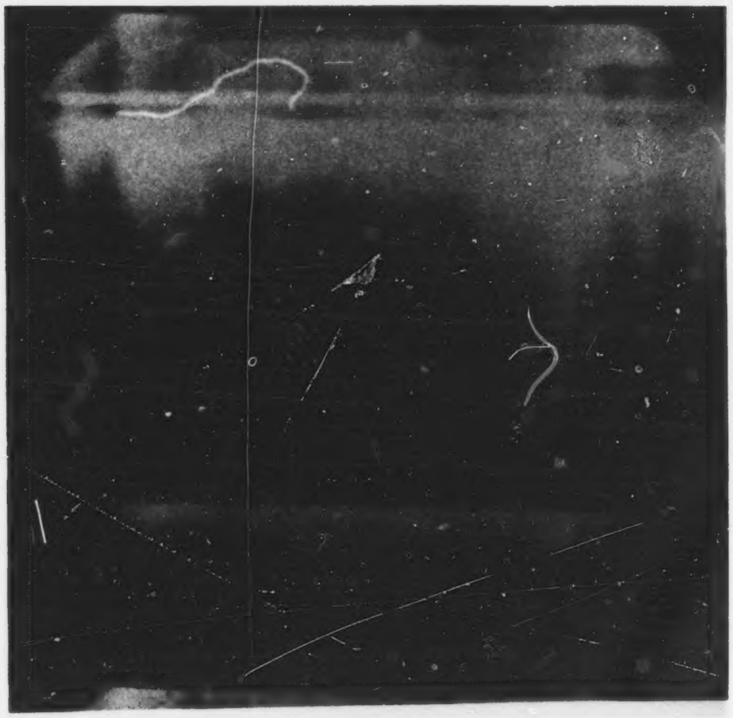

t = 4.04 s

t = 5.167 s

The beat frequency bar has obscured the image.

t = 6.04 s

Intense eruption of gas turns the molten pool into filaments.

BEST DOCUMENT AVAILABLE

t = 7.04 s

t = 7.96

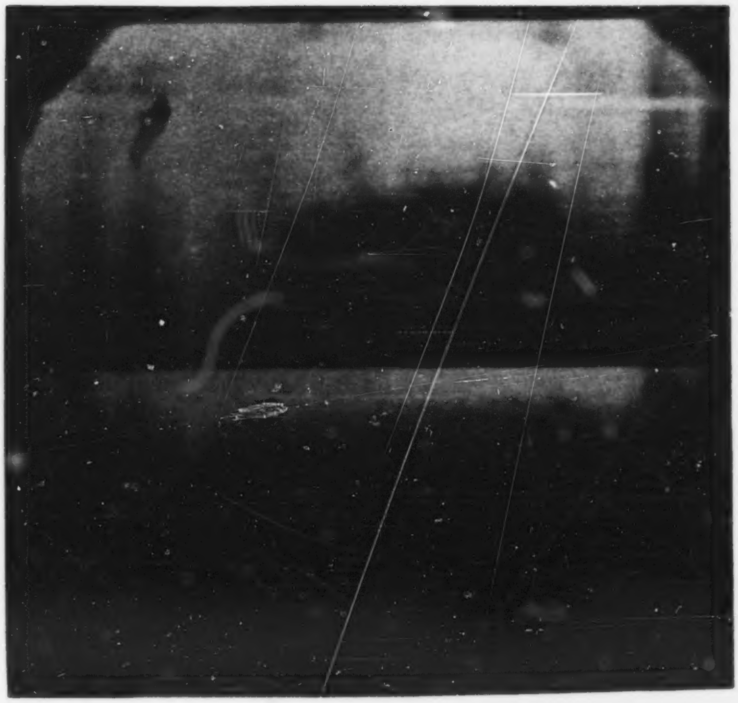

t = 11.12

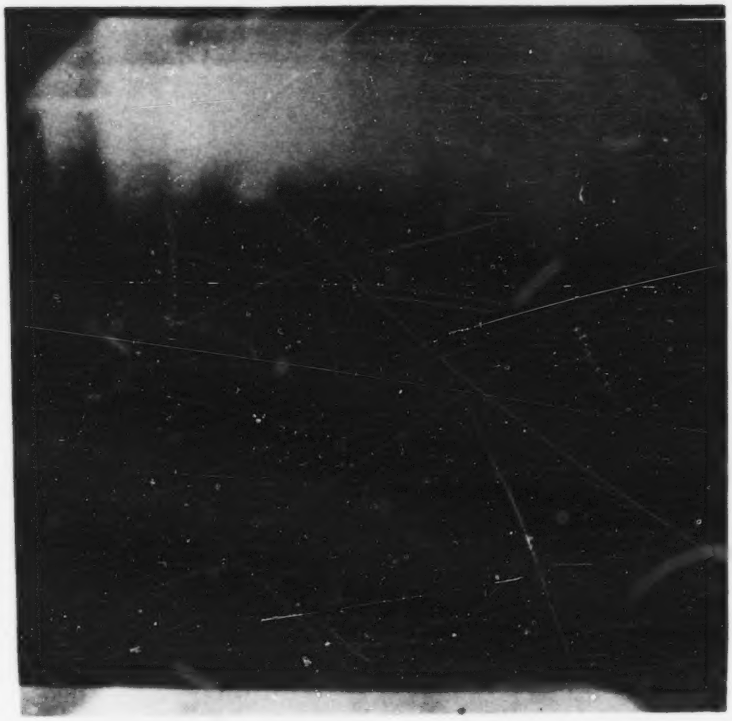

t = 12.12

t = 15.04 s

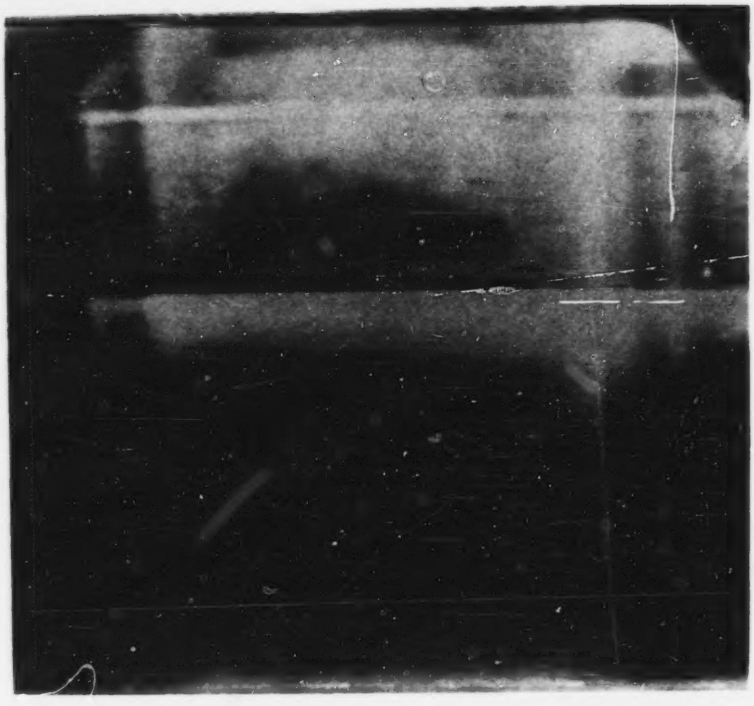

t = 16.12 s

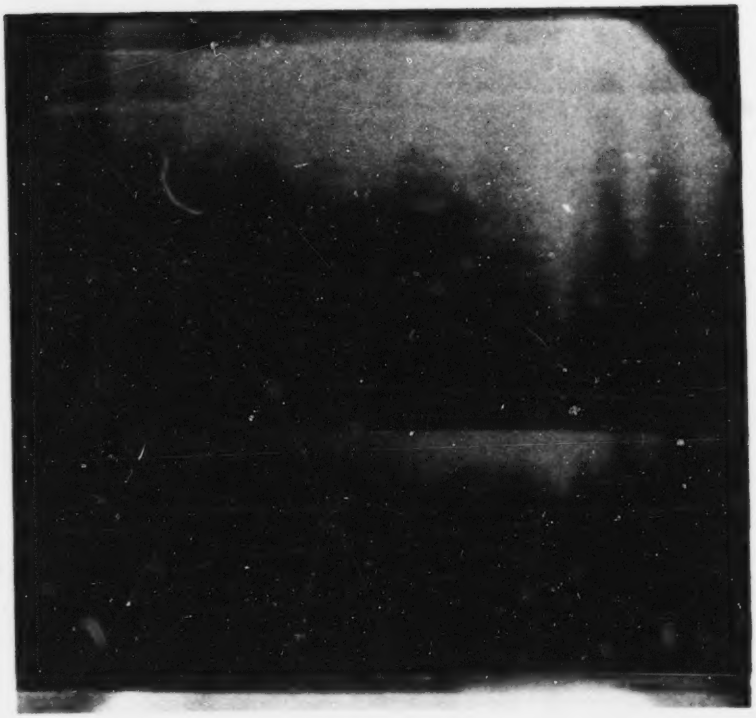

t = 17.17 s

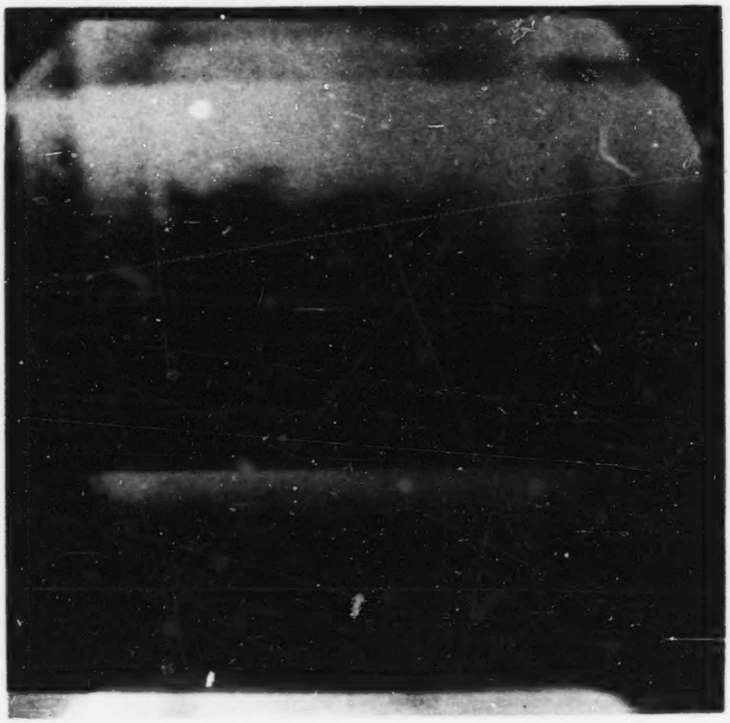

t = 18.12 s

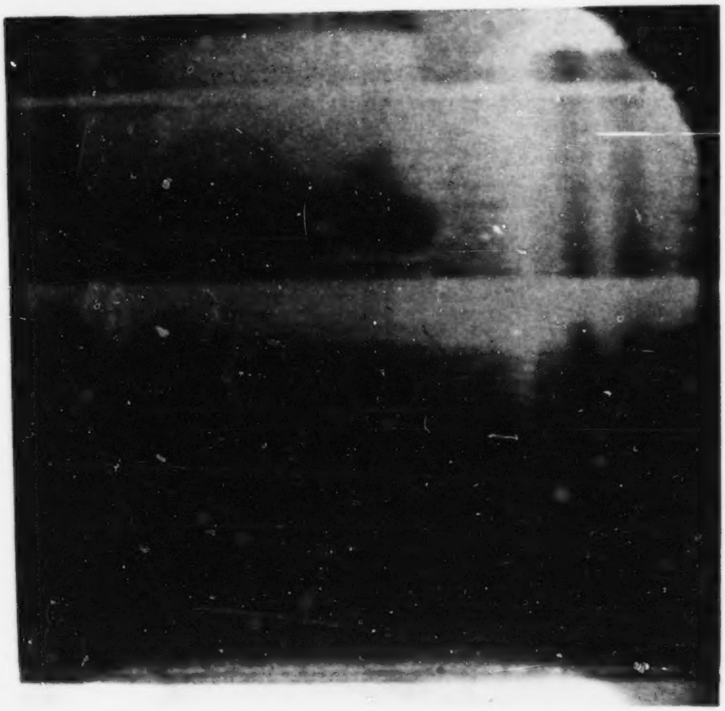

t = 19.12

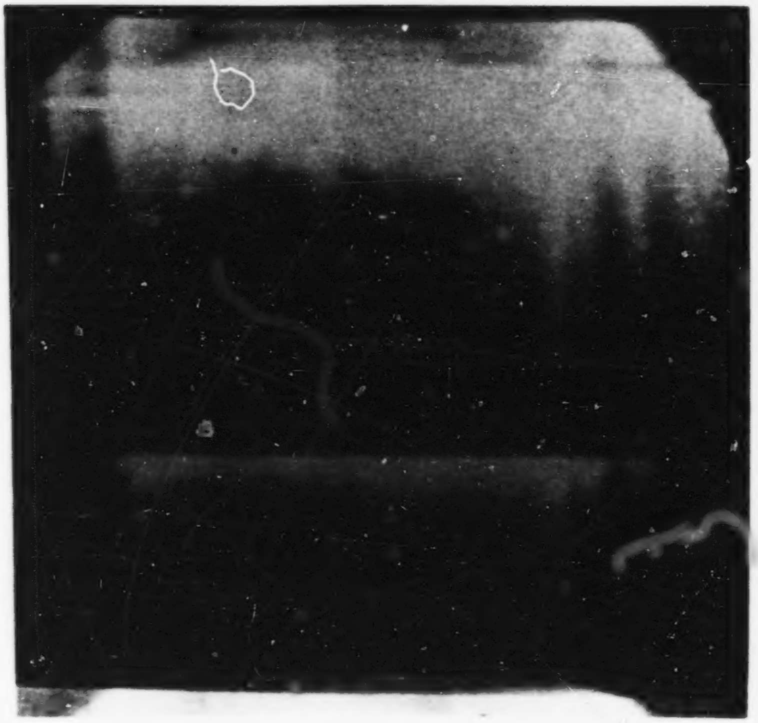

t = 21.17

Bubble diameters
are 1.9 and 1.3 cm.

BEST DOCUMENT AVAILABLE

t = 22.17 s

Quiescent period

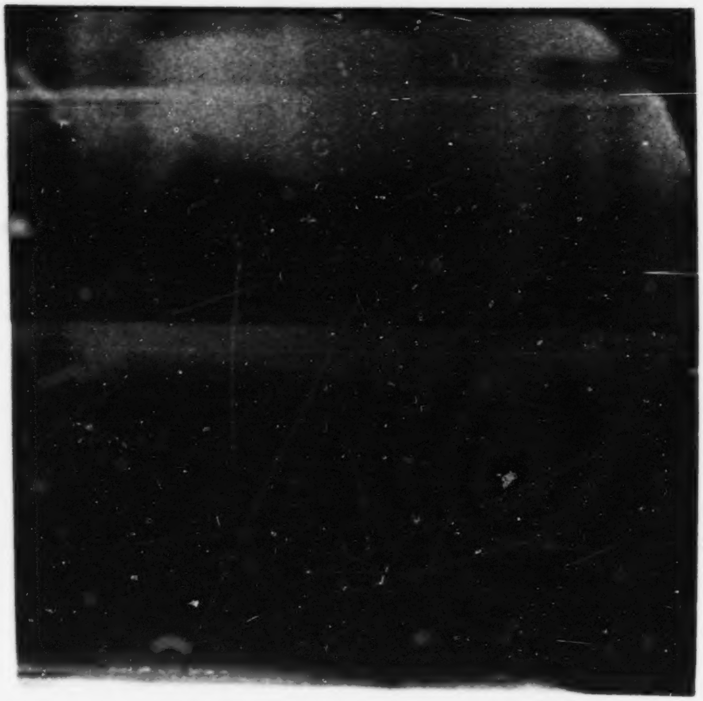

t = 23.12

Gas eruption from the wall

BEST DOCUMENT AVAILABLE

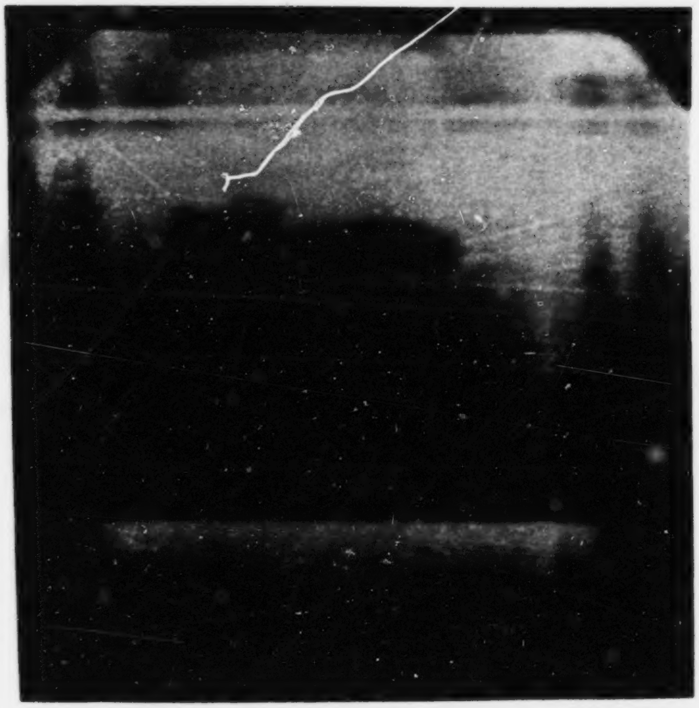

t = 24.17 s

t = 25.00 s

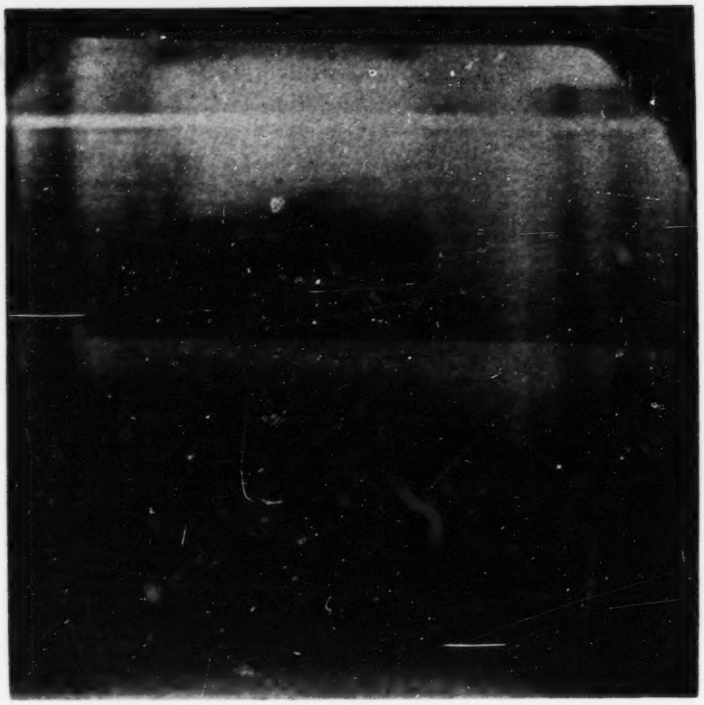

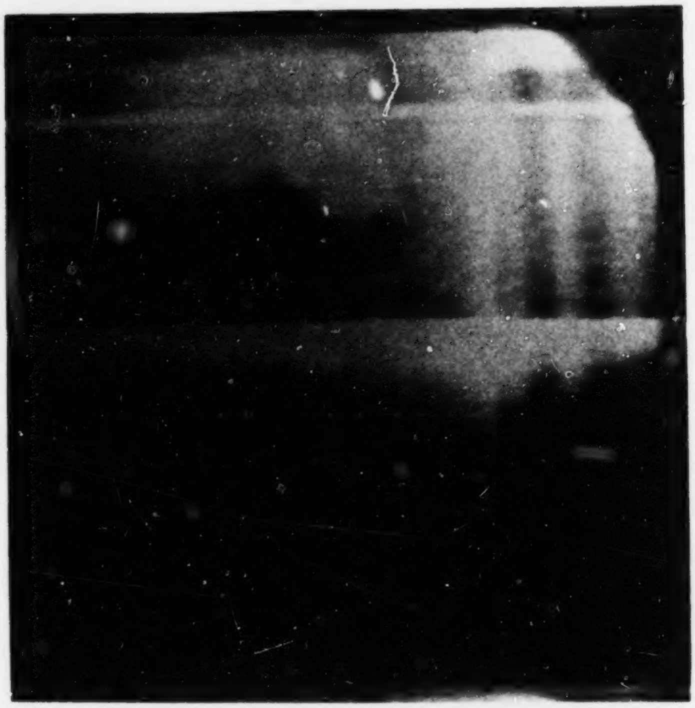

t = 26.0

Gas bubbles diameters are about 1.9, 0.9, and 1.1 cm.

t = 27.04 s

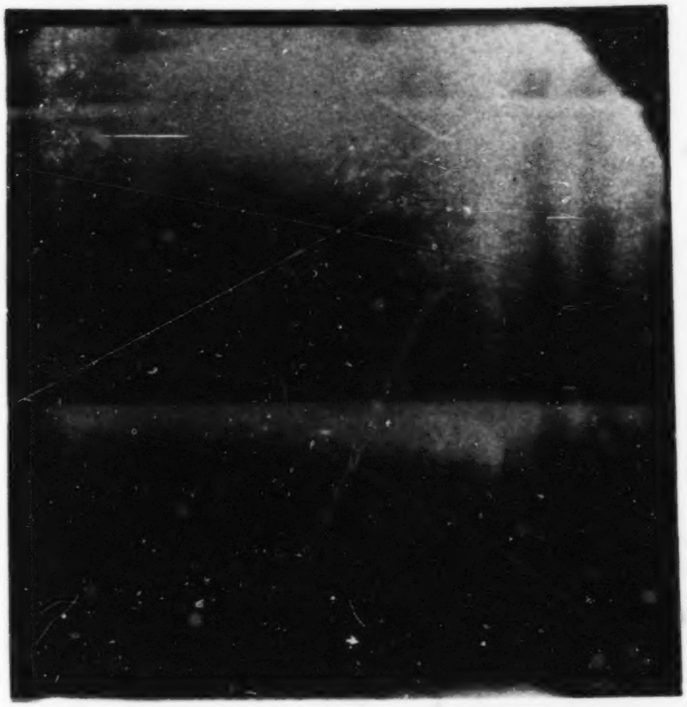

t = 28.08 s

Gas bubble has a diameter of about 1.7 cm.

t = 29.04

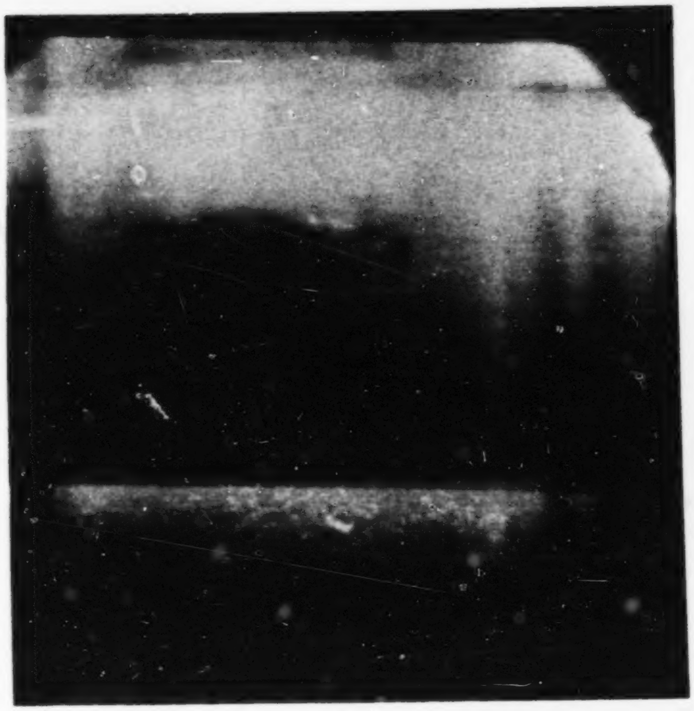

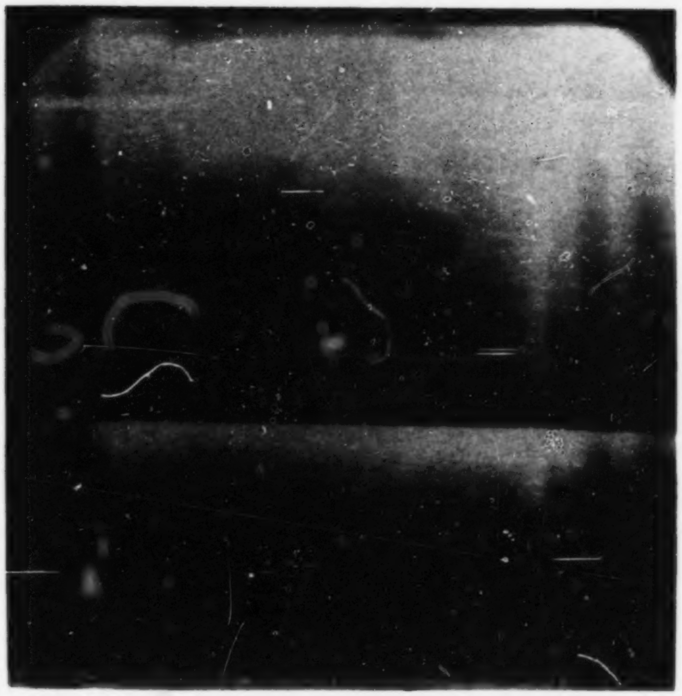

t = 31.12 s

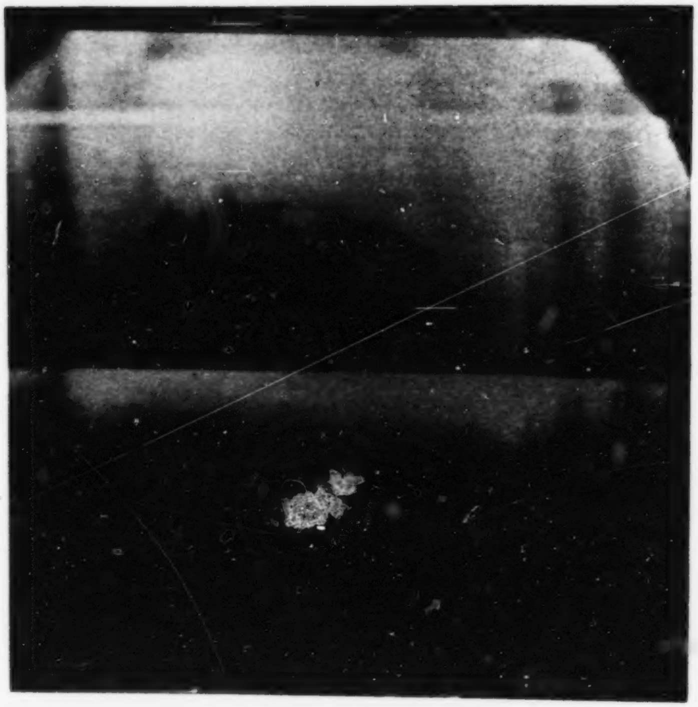

t = 32.04 s

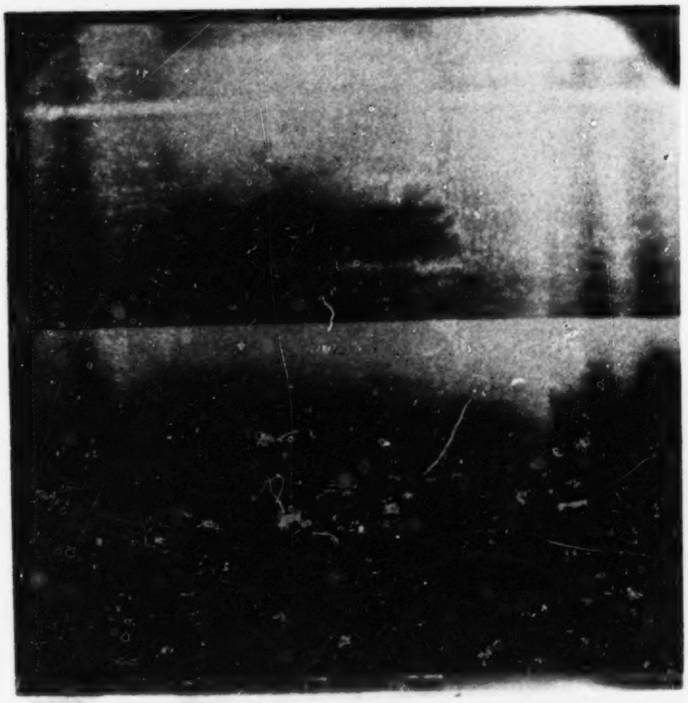

t = 33.08 s

Eruptions at locations about the centerline on the cavity bottom

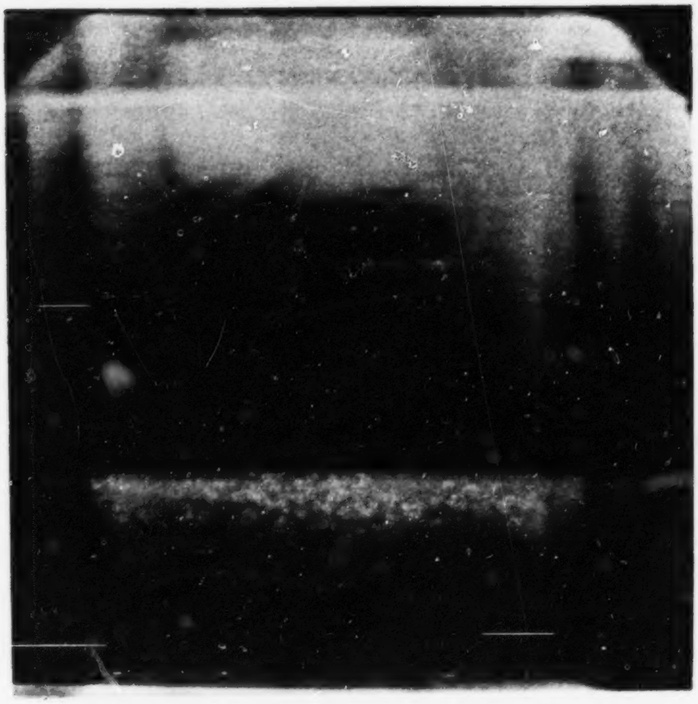

t = 36.04 s

Visible tendency for the oxide phase to solidify.

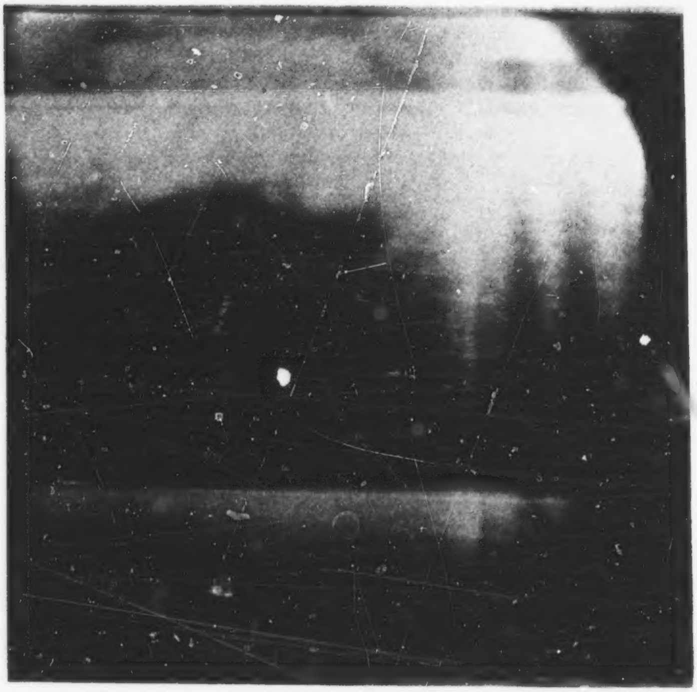

t = 37.04 s

Gas bubble is about 1.3 cm.

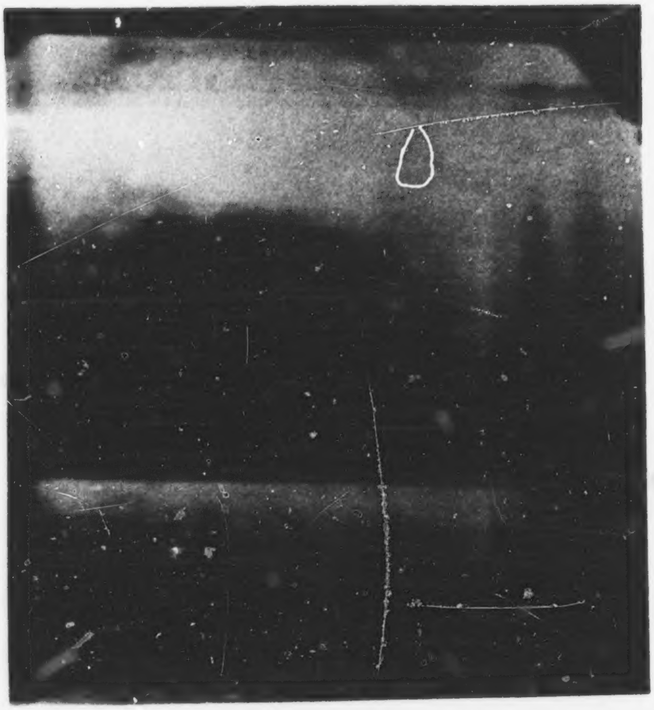

t = 39.00 s

Gas eruption from the cavity wall

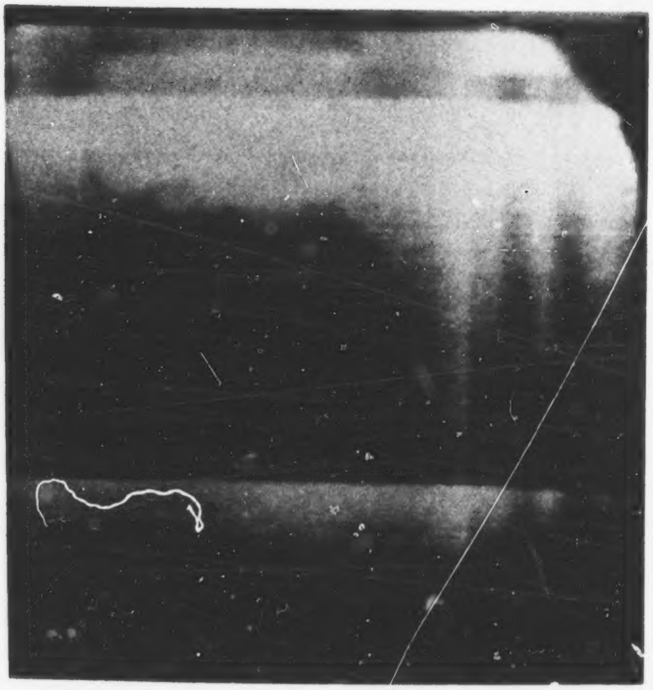

t = 41.04 s

Notice distinct crusts of oxidic material above the melt at the cavity walls.

t = 42.08 s

Eruption from wall and base. Gas bubble diameters are about 0.8 and 1.9 cm.

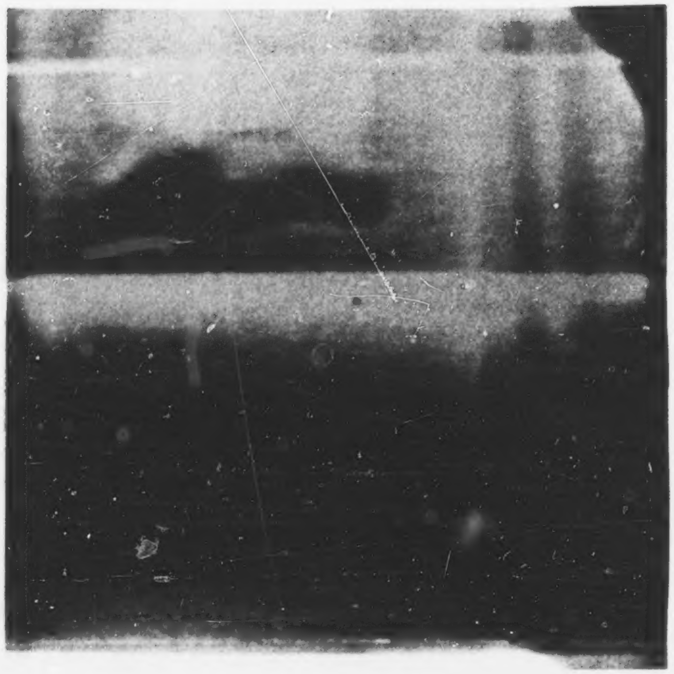

t = 44.08 s

t = 45.08 s

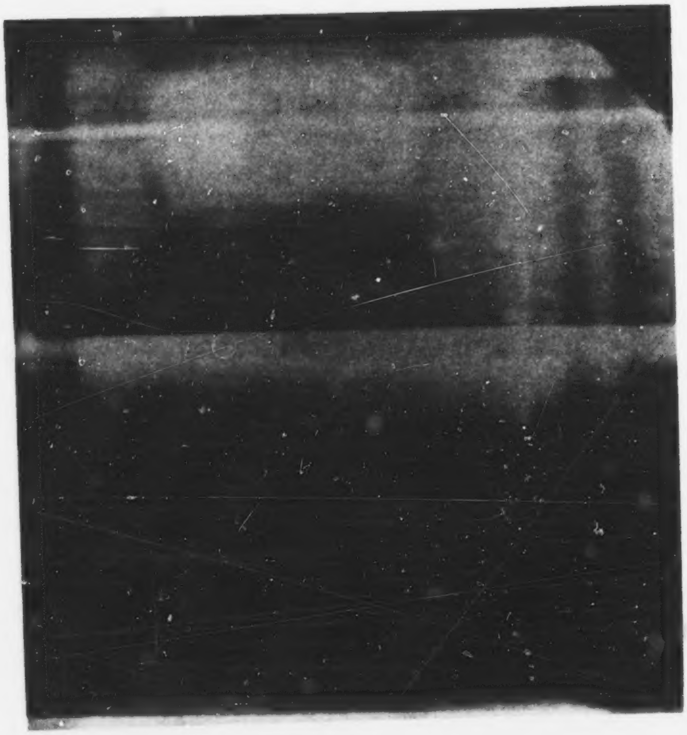

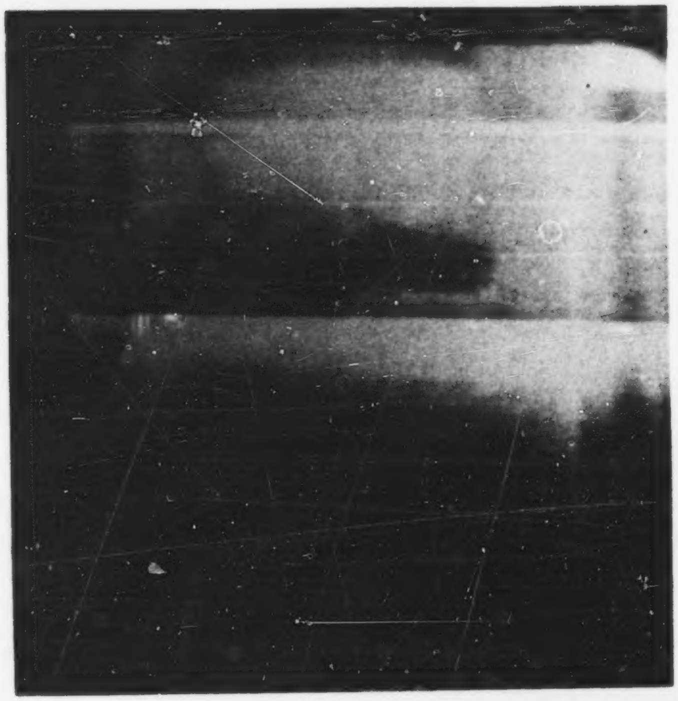

t = 45.96 s

Notice how "sticky" material at the top of the pool forms bubbles. Diameters are about 1.5 cm.

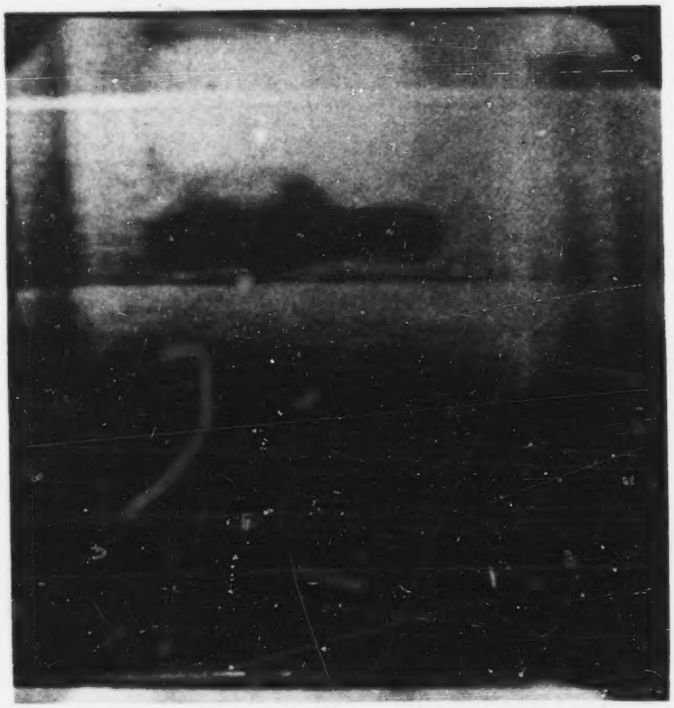

t = 46.96 s

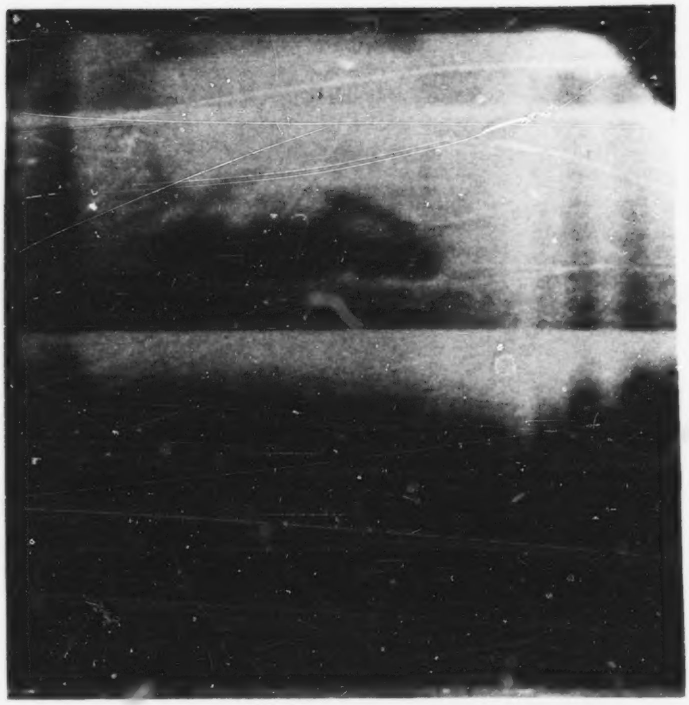

t = 47.96 s

Bubble diameter is about 2.1 cm.

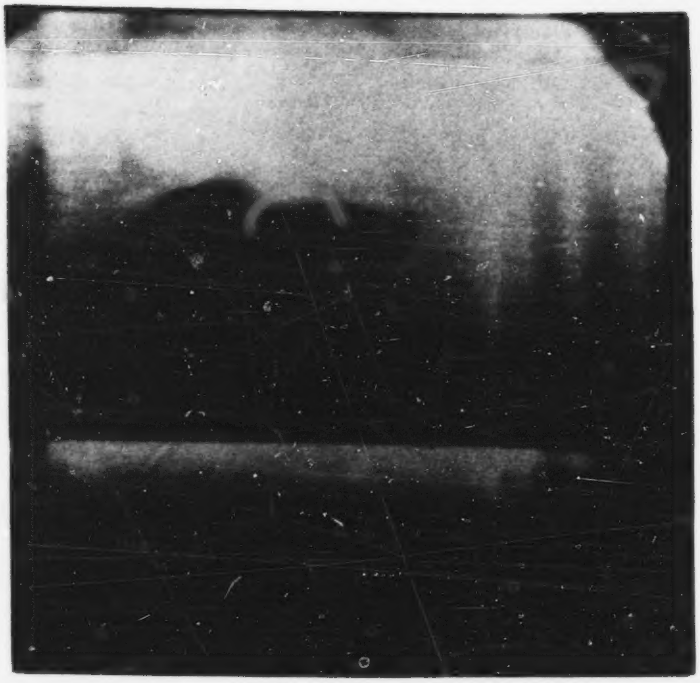

t = 48.96 s

t = 50.08 s

Thin slag crust beginning to form.

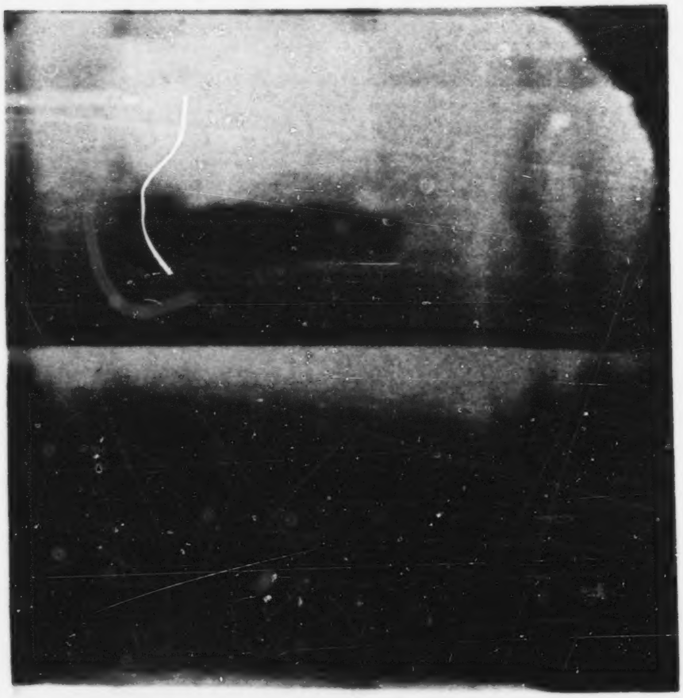

t = 51.08 s

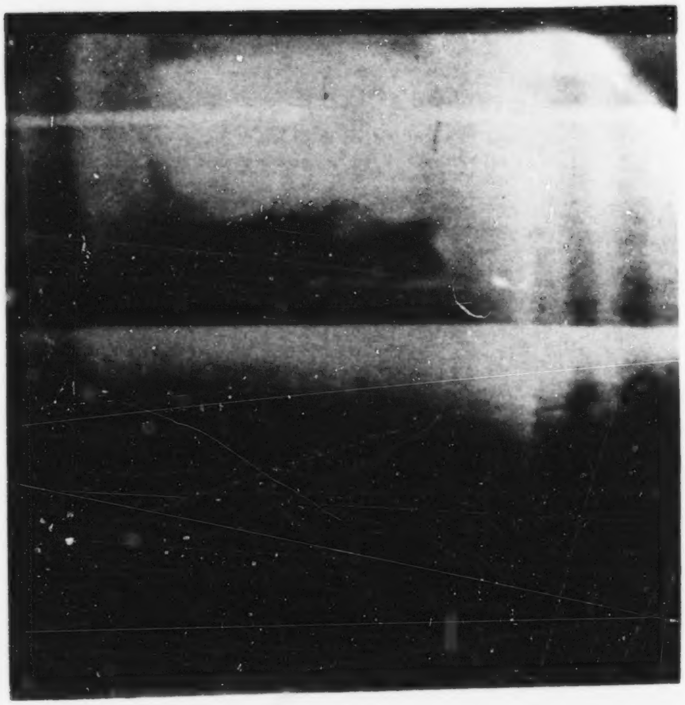

t = 52.42 s

Bubble diameter is about 1.9 cm.

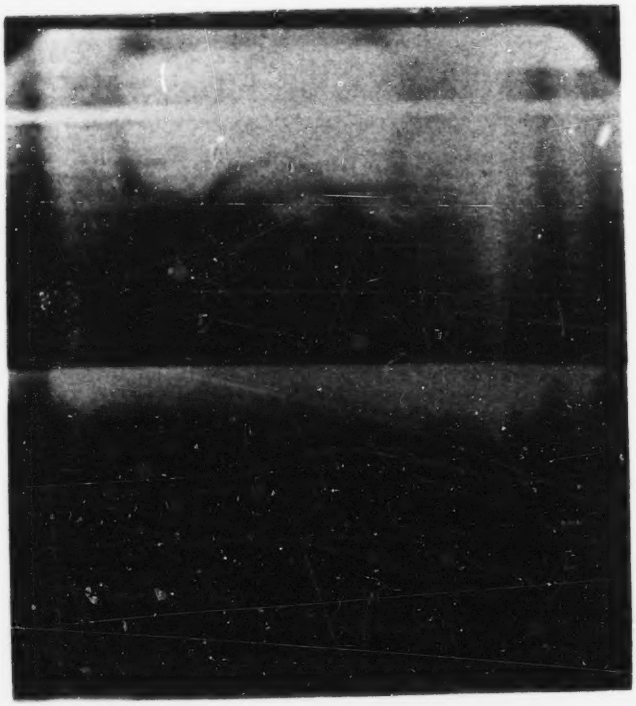

t = 53.08 s

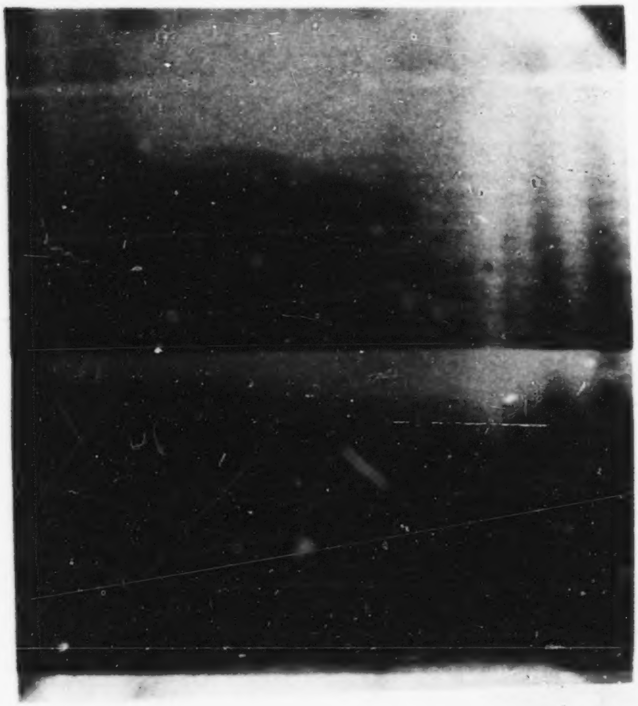

t = 54.04 s

Gas erupting into melt.

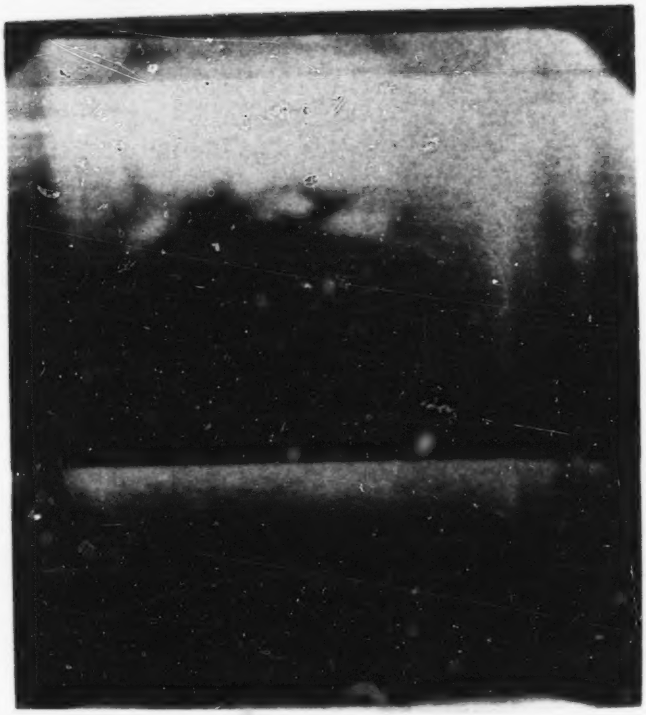

t = 56.12 s

Melt has gotten quite viscous

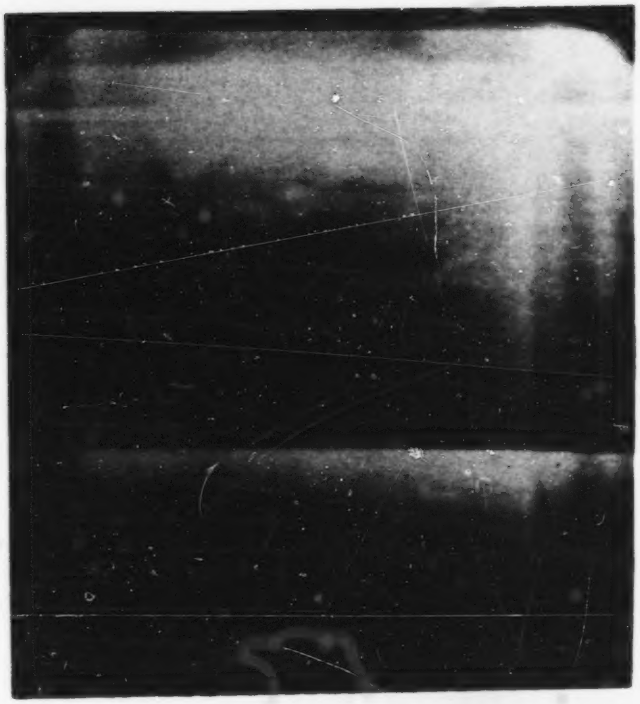

t = 57.08 s

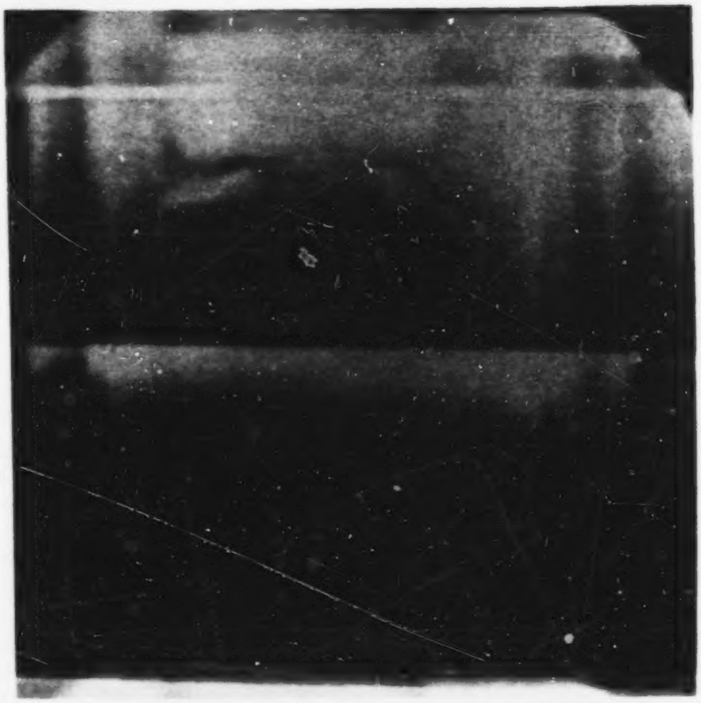

t = 59.00 s

Oxidic material is still fluid enough to be pushed aside by evolved gas. Notice how settled the metallic melt is when it is not disturbed by an evolved gas bubble.

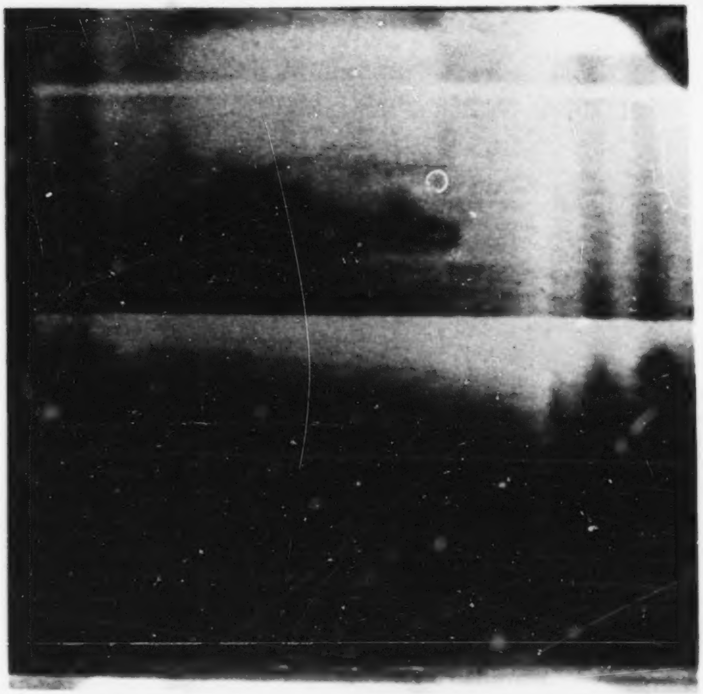

t = 60.00 s

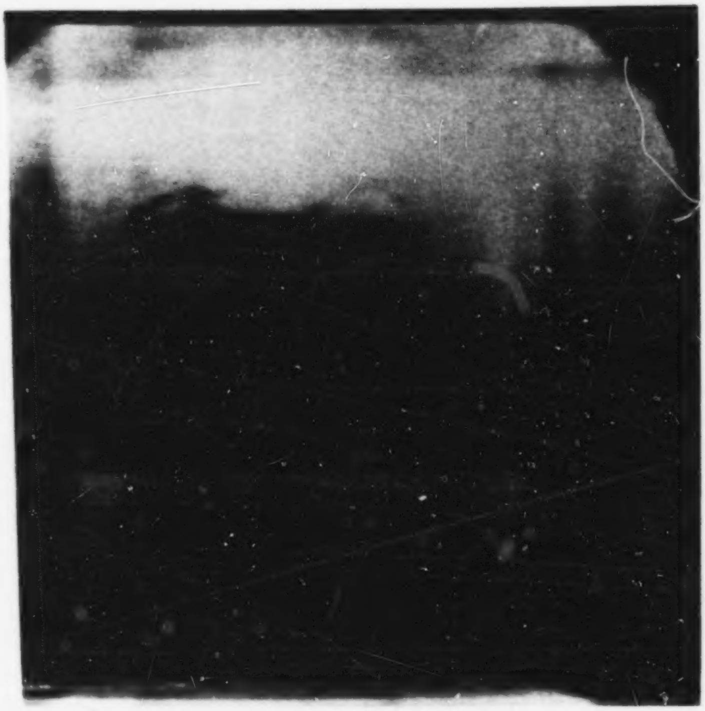

t = 61.04 s

BEST DOCUMENT AVAILABLE

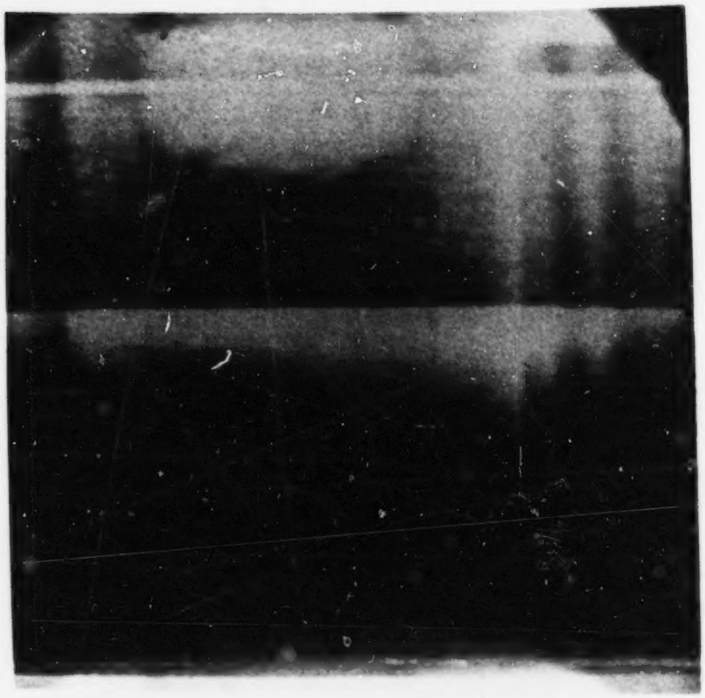

t = 62.00 s

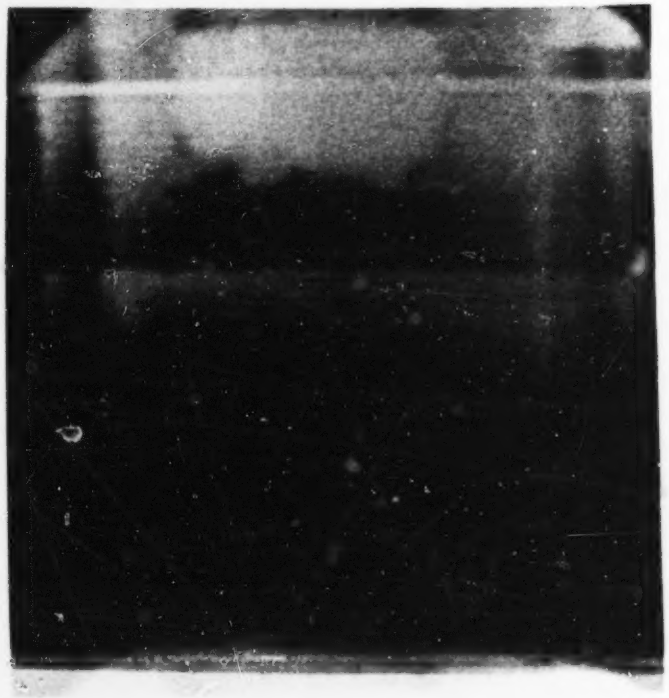

t = 63.04 s

Gas still evolves
from the special
locations on either
side of the
centerline

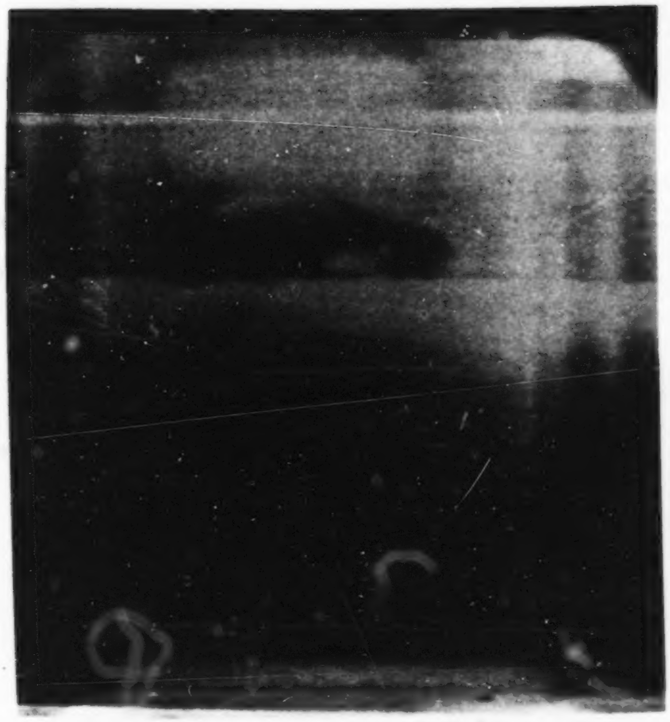

t = 65.00 s

Bubble diameter is 2.1 cm.

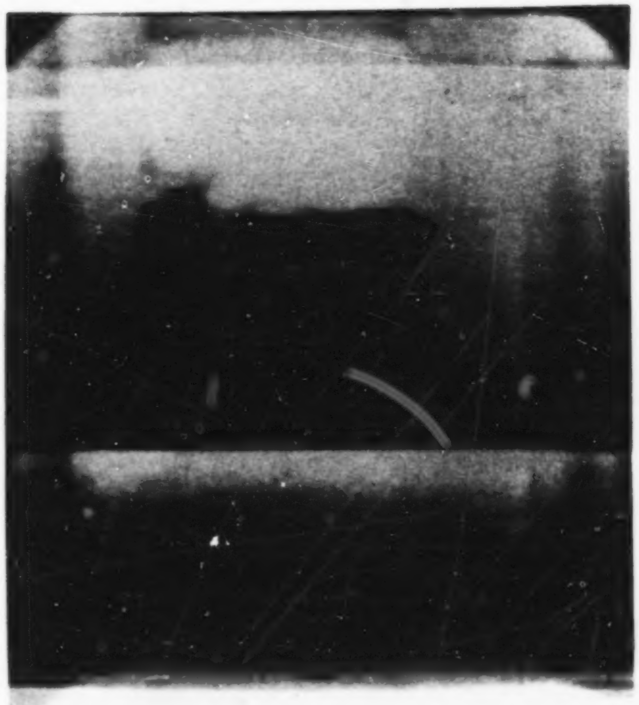

t = 67.29 s

Melt is frozen with gas bubbles entrained in the metal.

BEST DOCUMENT AVAILABLE

DISTRIBUTION:

US NRC Distribution Contractor (CDSI)
7300 Pearl Street
Bethesda, MD 20014
295 copies for R7
25 copies for NTIS

Author selected distribution - 108
(List available from author)

1530	W. E. Caldes
1537	N. R. Keltner
1537	R. U. Acton
1537	B. F. Blackwell
1537	T. Y. Chu
4400	A. W. Snyder
4410	D. J. McCloskey
4412	J. W. Hickman
4413	N. R. Ortiz
4414	G. B. Vernado
4414	J. Darby
4414	A. S. Benjamin
4420	J. V. Walker
4421	R. L. Coats
4421	J. B. Rivard
4421	G. Fieg
4421	K. Takahashi
4422	D. A. Powers
4422	J. Brockmann
4422	R. M. Elrick
4422	J. D. Fish
4422	J. Smaardyk
4423	P. S. Pickard
4424	M. J. Clauser
4424	F. W. Sciacca
4424	M. E. Senglaub
4424	D. C. Williams
4424	F. E. Haskin
4425	W. J. Camp
4425	W. M. Breitung
4425	F. Briscoe
4425	M. Pilch
4426	G. L. Cano
4440	G. R. Otey
4441	M. Berman
4441	R. K. Cole, Jr.
4441	J. C. Cummings
4441	D. Kelley
4442	W. A. Von Riesemann
4443	D. A. Dahlgren
4443	P. Yarrington
4445	L. O. Cropp
4450	J. A. Reuscher
4452	M. Aker
5800	R. S. Claassen
5820	R. E. Whan
5822	K. H. Eckelmeyer
5830	M. J. Davis
5836	F. J. Zanner
5840	N. Magnani
5846	E. Beuchamp
5846	W. Averill
8214	M. A. Pound
3141	L. J. Erickson (5)
3151	W. L. Garner (3)